MELT ON ANTARCTIC ICE SHELVES: OBSERVING SURFACE MELT DURATION

FROM MICROWAVE REMOTE SENSING AND MODELING THE DYNAMICAL

IMPACTS OF SUBSHELF MELTING

By

Andrew Johnson, B.S.

A Dissertation Submitted in Partial Fulfillment of the Requirements

for the Degree of

Doctor of Philosophy

in

Geophysics

University of Alaska Fairbanks

December 2021

APPROVED:

Dr. Regine Hock, Committee Chair
Dr. Mark Fahnestock, Committee Member
Dr. Andy Aschwanden, Committee Member
Dr. Ed Bueler, Committee Member
Dr. Paul McCarthy, Chair
    Department of Geosciences
Dr. Kinchel Doerner, Dean
    College of Natural Sciences and Mathematics
Dr. Richard Collins
    Director of the Graduate School

Abstract

Melt on the surface and underside of Antarctic ice shelves are important to the mass balance and stability of the ice sheet, and therefore pose significance to global sea levels. Satellite-based passive microwave observations provide daily or near-daily coarse resolution surface observations from 1978 on, and we use this record to identify days in which melt water is present on the ice sheet and ice shelf surfaces, called melt days. There are significant differences in the results of melt detection methods however, and we evaluate four different passive microwave melt detection algorithms. There is a lack of sufficient ground truth observations, so we use Google Earth Engine to build time series of Sentinel-1 Synthetic Aperture Radar images from which we can also detect melt to serve as a comparison dataset. A melt detection method using a Kmeans clustering algorithm developed here is shown to be the most effective on ice shelves, so we further apply this method to quantify melt days across all Antarctica ice shelves for every year from 1979/80 to 2019/20. The highest sums of melt days occur on the Antarctic Peninsula at 89 melt days per year, and we find few linear trends in the annual melt days on ice shelves around the continent. The primary mode of spatial variability in the melt day dataset is closely related to the Southern Annular Mode, a climate index for the southward migration of Southern Westerly Winds, which has been increasing in recent decades. Positive Southern Annular Mode index values are associated with decreased melt days in some regions of Antarctica. We also present a novel application of passive microwave analysis to detect changes in firn structure due to unusually large melt events in some regions and we show how this method detects ice lens formation and grain growth on specific ice shelves.

To study the impacts of subshelf melt we focus on the Filchner-Ronne region of Antarctica, which contains the second largest ice shelf on the continent. We performed an ensemble of ice sheet model runs for a set of ocean warming scenarios. Each ensemble used a realistic range of physical parameters to control ice dynamics and sliding, generated by a Bayesian

analysis of a surrogate model and observed velocities. Increased ocean temperatures were associated with increased mass loss, and by the year 2100 this region contributed 14 mm to sea level per degree of ocean warming at depth between $+0°C$ and $+4°C$ of ocean potential temperature. Beyond $+4°C$, the rate mass loss increased substantially. This mass loss corresponded to grounding line retreat across the region.

Table of Contents

List of Figures

List of Tables

x

Acknowledgments

1 Introduction

Antarctica, the vast southern polar continent, provides a ballast for global climate. The ice sheet has a perennially snow-covered area of 14 million km^2, lowering planetary albedo, and contains 26.5 million gigatons of ice, representing 70% of all freshwater on earth and carrying the potential for 60 m of sea level rise. The majority of Antarctica remains stable unless surface temperatures rise by 6 to 9°C above pre-industrial levels (Garbe et al., 2020). While this continent represents the coldest and driest surfaces on the globe, it also carries great importance to global climate and sea levels this century. By the year 2100, an inter-comparison of ice sheet models demonstrate that Antarctica could contribute between -7.8 and +30 cm to global sea levels (Seroussi et al., 2020).

Much of Antarctica is surrounded by floating outflows of glacier ice, called ice shelves. These ice shelves cover 75% of the coastline of the continent (Rignot et al., 2013) and are an important part of the ice sheet system. Ice shelves are vulnerable to very rapid changes due climate forcing from the ocean or atmosphere, for example ice shelves on the Antarctic Peninsula have lost 18% of their surface area over 1960-2010 (Cook and Vaughan, 2010). Because their basal surfaces are exposed to ocean waters, ice shelves can thin rapidly with increasing ocean temperatures. Intrusions of warm Circumpolar Deep Water today are driving rapid thinning along the western Antarctic Peninsula (Cook et al., 2016) and warm deep waters are beginning to reach the grounding lines of critical ice shelves along the Amundsen Sea in West Antarctica (Wåhlin et al., 2021).

Melt at the surface of ice shelves has implications on ice shelf stability. Ice shelves sit at low elevations and in close proximity to the ocean, and they have some of the highest melt rates across the continent (Jakobs et al., 2020). Surface melt can pool into ponds, and these ponds can fill in existing crevasses in the ice. This water can widen the crevasses, structurally weakening the ice shelf and leading to increased calving and potentially to rapid disintegration of the ice shelf (MacAyeal et al., 2003, Scambos et al., 2009). The Larsen B

Ice Shelf in the Antarctic Peninsula collapsed in 2002, where an ice shelf area of 3250 km^2 was lost over the span of just five weeks. This event has been suggested to be the product of this hydrofracture (Banwell et al., 2014). Melt pond-driven hydrofracture on ice shelves is thought to occur if the annual temperature is above a threshold (–9°C, from Morris and Vaughan, 2003), or if surface melt is above a threshold rate for a decade (725 mm a^{-1}, from Trusel et al., 2015).

While surface melt is observed at individual sites across Antarctica, there are no direct measurements of melt spanning the entire ice sheet. However, satellite-based Ku and K band passive microwave sensors, also called radiometers, have been taking daily or nearly-daily observations of Antarctica from 1978 on and these observations can be used to identify if melt water is present in a surface. Days with melt, from here on called melt days, can quantified for each 25 km pixel in the passive microwave record. The total melt days each year, called annual melt days, provide a readily available Antarctic climate dataset.

Chapter 2[1] evaluates the performance of different algorithms which quantify melt days from the passive microwave observations. This chapter demonstrates that different accepted melt detection algorithms show significant variability between each other, and there is little ground truth data available to rectify the issue. In this chapter we create a comparison dataset by leveraging Google Earth Engine to produce time series of high resolution Sentinel-1 SAR measurements. We are able to detect melt in the time series of SAR images. Using this comparison dataset we are able to evaluate the performance of several different passive microwave melt detection algorithms, and study the issues caused by their coarse spatial resolution. Melt detection is evaluated both on Antarctic Peninsula ice shelves, as well as on the pixels surrounding ice shelves which have significantly more topographic variation.

Chapter 3[2] applies the melt detection methodology recommended in Chapter 2 to study

---

[1]Published as: Johnson, A., Fahnestock, M., & Hock, R. (2020). Evaluation of passive microwave melt detection methods on Antarctic Peninsula ice shelves using time series of Sentinel-1 SAR. *Remote Sensing of Environment*, 250, 112044.

[2]Published as: Johnson, A., Hock, R., Fahnestock, M. (2021). Spatial variability and regional trends of Antarctic ice shelf surface melt duration over 1979 - 2020 derived from passive microwave data. *Journal of Glaciology*, 1-14.

melt across all Antarctic ice shelves from 1979 through 2020. This study is able to produce an annual melt day history for each ice shelf measurable at 25 km resolution. From the annual melt day dataset, this chapter shows the trends and the spatial patterns in the annual melt day record over this time period. The modes of spatial variability are shown to be closely related to the years with abnormally high melt. A novel observation in the passive microwave record is also presented in Chapter 3. Large melt events cause grain growth and produce ice lenses, which impact the microwave-band scattering properties of the surface. Chapter 3 argues that these melt-induced changes on surfaces which do not usually melt are observable in the passive microwave record.

One of the reasons why the stability of ice shelves around Antarctica is important is because of the connection between ice shelves and the ice sheet dynamics on the continent. Based on their geometry, ice shelves can provide backstress to reduce ice fluxes at the grounding line (Dupont and Alley, 2005). After the collapse of the Larsen B Ice Shelf in 2002, significant acceleration of grounded ice was observed in the region, leading to sustained increased ice discharge and surface lowering (De Angelis and Skvarca, 2003, Rignot et al., 2004, and Scambos et al., 2004). In West Antarctica, the Thwaites and Pine Island ice shelves help to buttress a marine ice sheet (Fürst et al., 2016), which contains the potential for Marine Ice Sheet Instability (Weertman, 1974). Retreat onto a retrograde slope, the critical condition for Marine Ice Sheet Instability, could already be occurring in this region (Joughin et al., 2014 and Rignot et al., 2014).

For Chapter 4, we study the importance of ice shelves in one particular region of Antarctica, the Filchner-Ronne region, by using ice sheet modeling driven by different climate scenarios. This region experiences low surface melt rates (Jakobs et al., 2020) and, as Chapter 3 notes, there are few melt days, but changes in ocean temperature or circulations can cause order of magnitude changes in ice shelf basal melt rates on the Filchner-Ronne ice shelf (Hazel and Stewart, 2020). Much of the Filchner-Ronne region contains ice which is grounded on a bed below sea level (Morlighem, 2020). In this chapter, we test the impact

of altering the ocean temperature by using the Parallel Ice Sheet Model (PISM) to model the response of ice in the region. We use neural networks to develop a surrogate model and we compare the surrogate model to observed ice velocities to help us determine a posterior distribution for some physical model parameters which control ice dynamics and sliding. We perform an ensemble of model runs for each scenario with parameters drawn from this posterior distribution. This work is able to determine the increase of velocity of ice streams and increased grounding line ice fluxes of each scenario, as well as quantifying the overall losses and sea level contribution.

1.1 References

Banwell, A. F., D. R. MacAyeal, and O. V. Sergienko (2013), Breakup of the larsen b ice shelf triggered by chain reaction drainage of supraglacial lakes, *Geophysical Research Letters*, *40*(22), 5872–5876.

Cook, A. J., P. Holland, M. Meredith, T. Murray, A. Luckman, and D. G. Vaughan (2016), Ocean forcing of glacier retreat in the western antarctic peninsula, *Science*, *353*(6296), 283–286.

De Angelis, H., and P. Skvarca (2003), Glacier surge after ice shelf collapse, *Science*, *299*(5612), 1560–1562.

Dupont, T., and R. Alley (2005), Assessment of the importance of ice-shelf buttressing to ice-sheet flow, *Geophysical Research Letters*, *32*(4).

Fürst, J. J., G. Durand, F. Gillet-Chaulet, L. Tavard, M. Rankl, M. Braun, and O. Gagliardini (2016), The safety band of antarctic ice shelves, *Nature Climate Change*, *6*(5), 479–482.

Garbe, J., T. Albrecht, A. Levermann, J. F. Donges, and R. Winkelmann (2020), The hysteresis of the antarctic ice sheet, *Nature*, *585*(7826), 538–544.

Jakobs, C. L., C. H. Reijmer, C. P. Smeets, L. D. Trusel, W. J. Van De Berg, M. R. Van Den Broeke, and J. M. Van Wessem (2020), A benchmark dataset of in situ antarctic surface melt rates and energy balance, *Journal of Glaciology, 66*(256), 291–302.

Joughin, I., B. E. Smith, and B. Medley (2014), Marine ice sheet collapse potentially under way for the thwaites glacier basin, west antarctica, *Science, 344*(6185), 735–738.

MacAyeal, D. R., T. A. Scambos, C. L. Hulbe, and M. A. Fahnestock (2003), Catastrophic ice-shelf break-up by an ice-shelf-fragment-capsize mechanism, *Journal of Glaciology, 49*(164), 22–36.

Morlighem, M., E. Rignot, T. Binder, D. Blankenship, R. Drews, G. Eagles, O. Eisen, F. Ferraccioli, R. Forsberg, P. Fretwell, et al. (2020), Deep glacial troughs and stabilizing ridges unveiled beneath the margins of the antarctic ice sheet, *Nature Geoscience, 13*(2), 132–137.

Morris, E. M., and D. G. Vaughan (2003), Spatial and temporal variation of surface temperature on the antarctic peninsula and the limit of viability of ice shelves, *Antarctic Peninsula Climate Variability: Historical and Paleoenvironmental Perspectives, 79*, 61–68.

Rignot, E., G. Casassa, P. Gogineni, W. Krabill, A. Rivera, and R. Thomas (2004), Accelerated ice discharge from the antarctic peninsula following the collapse of larsen b ice shelf, *Geophysical Research Letters, 31*(18).

Rignot, E., S. Jacobs, J. Mouginot, and B. Scheuchl (2013), Ice-shelf melting around antarctica, *Science, 341*(6143), 266–270.

Rignot, E., J. Mouginot, M. Morlighem, H. Seroussi, and B. Scheuchl (2014), Widespread, rapid grounding line retreat of pine island, thwaites, smith, and kohler glaciers, west antarctica, from 1992 to 2011, *Geophysical Research Letters, 41*(10), 3502–3509.

Scambos, T., H. A. Fricker, C.-C. Liu, J. Bohlander, J. Fastook, A. Sargent, R. Massom, and A.-M. Wu (2009), Ice shelf disintegration by plate bending and hydro-fracture: Satellite observations and model results of the 2008 wilkins ice shelf break-ups, *Earth and Planetary Science Letters*, *280*(1-4), 51–60.

Scambos, T. A., J. Bohlander, C. u. Shuman, and P. Skvarca (2004), Glacier acceleration and thinning after ice shelf collapse in the larsen b embayment, antarctica, *Geophysical Research Letters*, *31*(18).

Seroussi, H., S. Nowicki, A. J. Payne, H. Goelzer, W. H. Lipscomb, A. Abe-Ouchi, C. Agosta, T. Albrecht, X. Asay-Davis, A. Barthel, et al. (2020), Ismip6 antarctica: a multi-model ensemble of the antarctic ice sheet evolution over the 21st century, *The Cryosphere*, *14*(9), 3033–3070.

Trusel, L. D., K. E. Frey, S. B. Das, K. B. Karnauskas, P. K. Munneke, E. Van Meijgaard, and M. R. Van Den Broeke (2015), Divergent trajectories of antarctic surface melt under two twenty-first-century climate scenarios, *Nat. Geosci.*, *8*(12), 927–932.

Wåhlin, A., A. Graham, K. Hogan, B. Queste, L. Boehme, R. Larter, E. Pettit, J. Wellner, and K. Heywood (2021), Pathways and modification of warm water flowing beneath thwaites ice shelf, west antarctica, *Science Advances*, *7*(15), eabd7254.

Weertman, J. (1974), Stability of the junction of an ice sheet and an ice shelf, *Journal of Glaciology*, *13*(67), 3–11.

2   Evaluation of passive microwave melt detection methods on Antarctic Peninsula ice shelves using time series of Sentinel-1 SAR[3]

Abstract

Passive microwave datasets have been used to quantify the extent and duration of surface melt in Greenland and Antarctica from 1978 on with daily and near-daily intervals. These results have important implications for climate analysis and may help evaluate ice shelf stability. However, the accuracy of passive microwave methods used to detect melt is difficult to quantify, especially on the Antarctic Peninsula. Here four different melt detection methods are employed, including a new formulation of a statistical analysis of brightness temperature time series using a K-means clustering algorithm. Strikingly, two of the most widely used passive microwave melt detection methods are found to vary by 48% mean days of melt per year across six different locations on the Larsen C, Wilkins, and George VI Ice Shelves. In the absence of ground truth observations, time series of Sentinel-1 SAR observations from 2016 on provide a comparison dataset. In topographically flat regions where surface melt is spatially uniform, the passive microwave melt detection method based on a K-means analysis and the cross-polarization gradient ratio method demonstrate the highest agreement and correlation with active radar melt detection methods. One issue which has plagued passive microwave analysis is its coarse spatial resolution. High resolution SAR images are able to demonstrate and quantify the spatial variability of melt within individual passive microwave pixels. Melt is shown to be suitably uniform in space for passive microwave applications at the study sites on Antarctic Peninsula ice shelves, but not so in other regions of the Antarctic Peninsula. Spatial heterogeneity of surface melt on the sub-pixel scale is often related to varying surface topography.

2.1 Introduction

Air temperatures on the Antarctic Peninsula have been changing faster than almost anywhere else on Earth over the past century. From 1900 to 2000, annual average air temperatures on the Peninsula rose by 4°C compared to the global of average 1°C over that time period (Morris and Vaughan, 2003). Antarctic Peninsula temperature increases have subsided since 2000 however (Turner et al., 2016). This climatic shift has been accompanied by large scale changes to the surface in the form of dramatic shrinking and thinning of ice shelves. Cook and Vaughan (2010) estimated that Antarctic Peninsula ice shelves have lost 18% of their area over the past fifty years. Shrinking and collapsing ice shelves have caused the acceleration and thinning of grounded tributary glaciers, leading to increased ice mass loss and sea level rise. This has been observed across the entire continent (Pritchard et al., 2012), and also in specific regions after total ice shelf collapse (De Angelis and Skvarca, 2003; Rignot et al., 2004, and Scambos et al., 2004).

These large-scale changes to ice shelves and glaciers are driven directly and indirectly by climate. Ice shelf viability has been suggested to be related to mean annual surface temperature (Morris and Vaughan, 2003) or to sustained levels of annual surface melt (Trusel et al., 2015). Melt pond driven hydrofracture is a key mechanism in the rapid collapse of ice shelves (MacAyeal et al., 2003; Scambos et al., 2000, and Scambos et al., 2009). This provides a means by which surface melt is directly related to ice shelf stability and implies a need for understanding the history of surface melt on ice shelves. Direct observations of surface melt are rare, but passive microwave satellite observations can be used to determine if melt water is present in the surface firn layer for a given day. High numbers of annual melt days, which are days where surface melt is present in the firn, have been noted in the years leading up to the collapse of the Larsen A and B ice shelves from passive microwave analysis (Fahnestock et al., 2002; Scambos et al., 2000).

Calibrating passive microwave melt detection methods for use on the Antarctica Peninsula is non-trivial, however. Different methods can provide vastly different results in this

region (Tedesco, 2009) and ground truth calibration measurements have historically been sparse. Automated weather stations are present, but few of these stations are located on surfaces that are uniform in topography across the entire coarse passive microwave pixel and also experience summer melt seasons longer than a month. In addition, these stations do not measure surface wetness or snow temperature, but rather 2 m air temperature, which is not a perfect analogue for the presence of surface melt, especially without calibration (Liang et al., 2013; Tedesco, 2009). Thus there is a pressing need for alternative methods.

Active radar has been shown to be able to detect melt on an ice sheet snow surface (Wismann, 2000) but previous studies comparing passive and active radar melt detection methods have been limited by radar systems with low revisit times or low resolution measurements. The relatively recent Copernicus Sentinel-1 constellation provides an unprecedented combination of high resolution SAR observations with rapid revisit-times. Open data policies and modern tools such as Google Earth Engine have made large sets of SAR data more accessible than ever before.

The purpose of this study is to evaluate the effectiveness of several passive microwave melt detection algorithms over selected study sites on the Antarctic peninsula and compare the results to SAR melt detection from Sentinel-1. The comparison is carried out on flat ice shelves with uniform melt patterns, and also on regions with more significant terrain features characterized by non-uniform melt within individual pixels.

2.2 Background

2.2.1 Passive microwave remote sensing of melt

Satellite-based microwave radiometers have measured upwelling radiation from 1978 on. The intensity of radiation at a given frequency interval is reported as the brightness temperature of a black body surface emitting the same amount of energy over that frequency interval. The frequencies observed by these sensors are on the order of 10s of GHz. The microwave-band emissivity of water is much higher than that of ice allowing increases in

9

brightness temperature to be used as an indicator for the presence of melt over snow and ice (Mote et al., 1993).

Most melt detection methods use 19 GHz in the horizontal polarization because it is the frequency and polarization that has the lowest brightness temperature over dry firn, thereby maximizing the change in brightness temperature caused by the emergence of liquid water (Liu et al., 2006). Nearly all upwelling radiation from a dry firn surface at 19 GHz originates in the top several meters of the firn column (Chang et al., 1976), or the top several centimeters for wet firn (Zwally and Fiegles, 1994). The magnitude of the signal is a function of the firn column temperature and water content, as well as impacts on scattering due to grain size and stratigraphy including ice lenses. Of these factors, the emergence or disappearance of water in the surface layer will generally have the largest impact on brightness temperature variation at daily timescales (Tedesco, 2007).

The effects of melt on microwave emissions are demonstrated in Fig. 2.1. The annual brightness temperature variability of dry (non-melting) firn in Fig. 2.1B is driven by seasonal thermal changes in the firn column. When there is summer melting however (Fig. 2.1A), there will be a much more significant brightness temperature increase. In some regions where significant summer melt occurs, such as on the Larsen C Ice Shelf, the winter brightness temperatures are much lower due to ice lenses in the firn scattering upwelling radiation.

Historically passive microwave melt detection studies have been used to detect snow melt on the Greenland Ice Sheet (e.g. Abdalati and Steffen, 1995; Joshi et al., 2001, and Mote et al., 1993) and on the Antarctic Peninsula (e.g. Tedesco, 2009, and Zwally and Fiegles, 1994), and to identify abnormal melt events (Nicolas et al., 2017; Tedesco et al., 2013, and Zwally et al., 2002). Comparisons of year-to-year results of passive microwave melt detection have been used to demonstrate an increase in the spatial extent of surface melt on the Greenland Ice Sheet over the past several decades (Fettweis et al., 2011) and an increase in annual melt days in the decade prior to the collapse of the Larsen A and B ice shelves (Fahnestock et al., 2002). Passive microwave melt detection results have been compared with and evaluated by
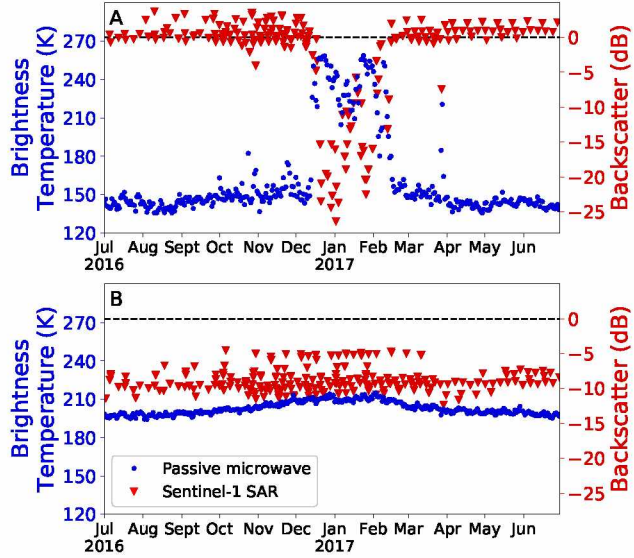
Figure 2.1: Raw passive and active microwave measurements of two locations for July 2016 through June 2017. Passive measurements are taken from SSMIS at 19 GHz in the horizontal polarization. Backscatter data is from Sentinel-1C-band SAR in the HH polarization. (A) Point on Larsen C Ice Shelf that experiences summer melt (53 m a.s.l.). (B) Point on Antarctic Peninsula ice sheet that does not melt (1107 m a.s.l.). Locations of A and B are shown in Fig. 2.2.

results from climate model simulations (Fettweis et al., 2006).

Traditionally satellite-based passive microwave sensors have had coarse spatial resolution, with composited daily data posted at single pixel sizes of 25×25 km^2 at the 19 GHz frequency. These satellite instruments measure upwelling radiation from an effective field of view with a footprint several times larger than the gridded 25 km pixel. As in previous studies, we will treat individual passive microwave pixels as representative of the conditions within that pixel on the surface. In many places surface melt is not uniform across the 25×25 km^2 area. Pixels with mixed regions of melting and no-melting are called "mixed pixels" and they have long been difficult for passive microwave melt detection studies to deal with.

2.2.2 Active microwave remote sensing of melt

A time series of backscatter observations from SAR or a scatterometer can be used to detect the presence of melt water. This has been demonstrated for firn on ice sheets and

ice shelves (Ashcraft and Long, 2006, and Trusel et al., 2012, and Wismann, 2000), as well as for firn and seasonal snow covers in mountainous areas (Nagler and Rott, 2000, Nagler et al., 2016, and Snapir et al., 2019). Liquid water in a snowpack increases the absorptivity and also increases the surface forward scattering of radar signals. These effects both reduce the backscatter with increasing moisture contents of the firn. Below snow moisture contents of 3%, absorption is expected to be the dominant contributor to backscatter reduction (Shi and Dozier, 1995).

Time series of SAR backscatter observations are shown in Fig. 2.1. When water appears due to surface melt during the summer, the backscatter decreases significantly (Fig. 2.1A). This decrease in the C-band single polarization horizontal SAR backscatter is consistent in location and timing with the increase in passive microwave brightness temperature. The time series of the dry firn surface (Fig. 2.1B) does not show this abrupt change in backscatter. The location with summer melt in Fig. 2.1A has higher winter backscatter values because summer melt refreezes into ice lenses which scatter significant radiation back to the satellite. In the SAR time series, differences in imaging geometry and look angle from different satellite passes account for most of the day-to-day variance in the observed winter backscatter signal. The observed backscatter of a single point does not vary much between repeated images with the same geometry, except when melt is present, but the backscatter varies by more than 5 dB between different imaging geometries in this example. Due to the variability of backscatter between viewing geometries, this study will only detect melt by comparing observations of the same geometry. Such an approach requires a large amount of SAR observations. This is made possible by the wealth of Sentinel-1 images presently available and their accessibility in Google Earth Engine. Satellite-based SAR and radar systems have traditionally been limited by long repeat times, low resolutions, or only covering certain years when a particular instrument has been active. These limitations have been greatly reduced by the launch of the Sentinel-1 satellite constellation. After the second satellite was added to the constellation in 2016, Sentinel-1 has provided C-Band imagery of the entire

Antarctic Peninsula with a revisit time of 1–3 days. Individual scenes are repeated every 6 or 12 days.

Detection of water in firn from SAR can have considerable advantages over passive microwave methods. Modern SAR systems have a resolution on the order of meters to tens of meters and thus much higher than passive microwave observations. The radar backscatter is also a product of fewer physical properties of the surface than passive emissions because it is unaffected by temperature in dry snow.

2.3 Site description

Passive and active radar observations were compared at study sites chosen across the major ice shelves of the Antarctic Peninsula. These sites were chosen to represent a geographically and climatically diverse set of ice shelf surface environments which experience summer melt and to include both uniform and mixed sites. The six uniform sites are expected to experience surface melt in spatially uniform patterns across passive microwave pixels, while the four mixed sites do not always melt uniformly.

The uniform sites were chosen on flat ice shelf surfaces. Almost all of these regions are 2 × 2 passive microwave pixel areas, resulting in a 2500 km² target area (Fig. 2.2). The sites L1, L2, L3, and L4 are on the Larsen C Ice Shelf. L2 and L3 are on the interior of the ice shelf, and melt there is expected to be impacted by foehn winds (Luckman et al., 2014). W1 covers 2500 km² of the southern Wilkins Ice Shelf. G1 spans 1 × 5 pixels (3125 km²) on the southern George VI Ice Shelf.

Mixed pixel sites were selected at the edge of ice shelves either near to the grounding line or intersecting it. All mixed sites cover single 25 × 25 km² passive microwave pixels. MP1 and MP2 are on the interior of the Larsen C, MP3 is along the northeastern interior of the Wilkins Ice Shelf, and MP4 is along the northwestern edge of the southern George VI Ice Shelf. MP1, MP2, and MP3 have elevation ranges greater than 1000 m in each of their respective 25 km surface regions, while MP4 has an elevation range of 360 m. Elevations
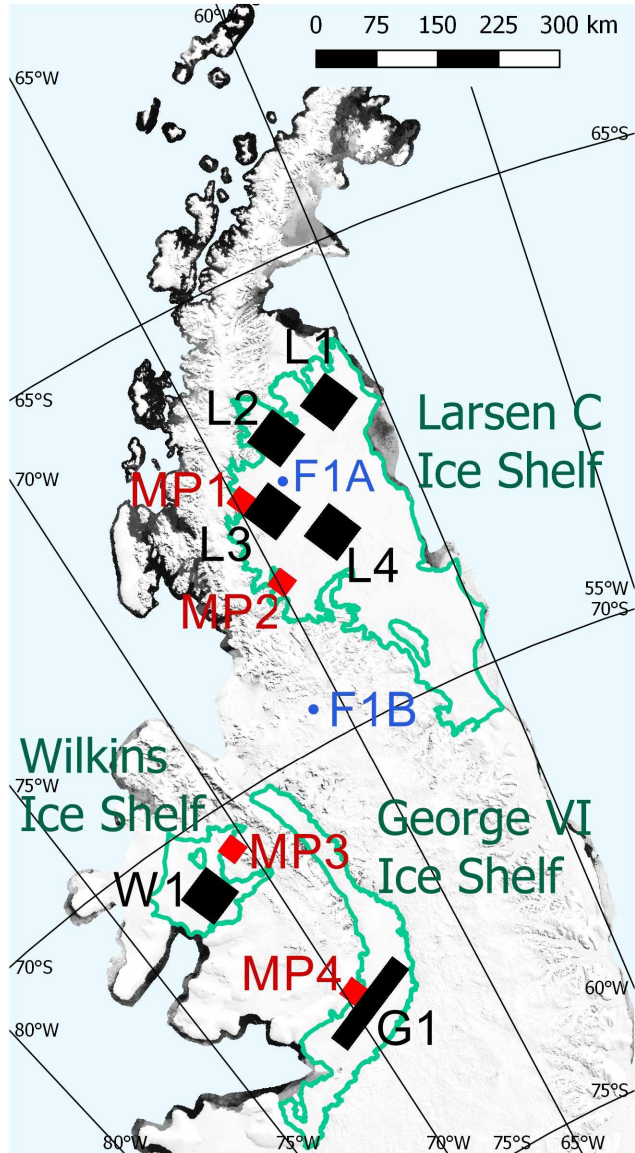
Figure 2.2: Location of the study sites. Uniform sites are marked in black while the mixed sites are shown in red. The blue dots labeled F1A and F1B note the locations of the two points used in Fig. 2.1. Approximate ice shelf outlines are shown in green. Background map is the 2009 MODIS mosaic (Haran et al., 2014).

come from the RAMP2 DEM (Liu et al., 2006). The mean standard deviation of elevation in each of the four 25×25 km^2 mixed pixels used in this study was 275 m, while the mean deviation of the uniform sites was only 5.7 m.

2.4 Methods

2.4.1 Passive microwave melt detection methods

Four different passive microwave melt detection algorithms were used to produce binary determination of the presence of surface melt water for each day at each pixel from 1979 to 2019. While we use the entire record to compare these methods to each other, we focus on the years 2016 to 2019 in detail because there is overlap with Sentinel-1 SAR. Each melt year covers the austral summer and is taken to be July 1 through June 30 of the following calendar year.

Observations from the scanning Multichannel Microwave Radiometer (SMMR) were used for 1979–1987 (Gloersen and Francis, 2003). The Special Sensor Microwave Imager (SSM/I) instrument provided daily data for 1987 to 2007 and the Special Sensor Microwave Imager/Sounder (SSMIS) provided daily data for 2006 on (Maslanik and Stroeve, 1999; Meier et al., 2019). SMMR observations were at a slightly different frequency and incidence angle, with SMMR observing 18.0 and 37.0 GHz at 50.2° incidence angle, and SMM/I and SMMIS observing 19.35 and 37.0 GHz at 53.1° incidence angle. Measurements from SMMR were only acquired approximately once every two days. A linear interpolation between days was applied to fill in missing days. Four different methods were employed to detect melt, detailed below. All passive microwave observations in this study are at 19 GHz in the horizontal polarization unless otherwise stated.

2.4.2 Delta above winter mean (W30K)

Mote et al. (1993) and Zwally and Fiegles (1994) demonstrated a method which detects melt when brightness temperatures are above a set threshold over the winter average. The

proposed rationale was that increases in brightness temperatures well above the typical seasonal variations are likely the result of the presence of liquid water. Mote et al. (1993) used a 31 K increase to indicate melt in Greenland, and Zwally and Fiegles (1994) used 30 K in the Antarctic Peninsula, which is the value used in this study. For the Antarctic Peninsula the winter mean brightness temperature refers to the mean brightness temperature in the austral winter months of June, July, and August. This melt threshold brightness temperature is recalculated for every year and each passive microwave pixel.

2.4.3   Sigma above winter mean (W3S)

Similar to the W3S method, Torinesi et al. (2003), proposed using statistically significant brightness temperature increases compared to times of dry snow to detect melt. In this method melt is assumed if the brightness temperature is three standard deviations above the mean brightness temperature of dry snow. The method was initially calibrated using measurements of Antarctica.

The melt threshold value is set through a three step process. To produce a dry snow time series, the brightness temperature time series for April 1 to March 31 of the following year was used. All values 30 K above the mean brightness temperature of the entire time series were removed, and then a new mean brightness temperature was found. That process was repeated two more times so as to produce a time series that likely only contains measurements of dry snow. The melt threshold was set at three standard deviations above the mean of that new time series. The melt threshold value was then applied to the original, unaltered brightness temperature time series.

2.4.4   KMean method

The emergence of liquid water in a previously dry snowpack has a strong non-linear response on measured brightness temperature. Fahnestock et al. (2002) demonstrated that a statistical approach to analyzing an annual brightness temperature time series can yield a

determination of melt independent of changing conditions in winter temperatures, ice lens formation, or grain size. In that method melting is assumed to occur when the annual brightness temperature time series has a bimodal distribution, with the higher mode being melt. The transition between modes is detected from the slope of the sorted annual brightness temperature time series.

Here we modified this approach to use a well known clustering algorithm to find the transition between modes and detect melt. A K-means clustering algorithm was used in one dimension to determine how well annual brightness temperature time series would fit into two clusters compared to one cluster. In this study the KMean package from the Python Scikit-Learn Clustering toolbox was used. The KMean algorithm requires the user to specify the number of clusters, and then it adjusts the location of the cluster centers by running iterations which minimize the root-mean-square distance of each data point to the nearest cluster center.

Several rules were used to detect melt. The sum of squared distances of each data point to the nearest cluster center is called the inertia. If the inertia in the two cluster case is less than 42% of the inertia of the one cluster case and the cluster centers are more than 20 K apart, then the algorithm is assumed to have succeeded and the upper cluster is considered to be melt. Additionally, if the centers of the clusters are more than 40 K apart in the two cluster case, then the upper cluster is considered melt. If neither of the above criteria are met then the clusters are not assumed to resemble melt. In that case a simple melt threshold of 40 K above the lower cluster center is set.

The difference between actual mean summer and winter snow temperatures is unlikely to exceed 40 K in Antarctica, so if the cluster centers themselves are greater than 40 K apart then that difference is unlikely to be solely due to thermal changes in the ice, implying it must be melt. If the cluster centers are less than 20 K apart then the clusters are likely too close for emergence of liquid water into a snowpack to be driving that variation. The application of a 40 K threshold to detect melt was rare on ice shelves. For 1979–2019 at

the six uniform ice shelf sites in this study, the threshold only needed to be applied 0.7% of the time. The 42% inertia reduction threshold was set by visual inspection of algorithm behavior given a number of brightness temperature time series on Antarctic Peninsula ice shelves. No inertia reduction threshold was able to solely identify when the upper cluster should be melt. All values between 40% to 45% showed no instances of false positives of melt, while they did show some occurrences of false negatives of melt. Whenever the KMean method positively identified the upper cluster to be melt, the cluster centers also met the 40 K difference threshold criteria.

2.4.5   Cross polarization gradient ratio (XPGR)

The XPGR method (Abdalati and Steffen, 1995) exploits the differences in microwave emissions at different frequencies and polarizations. Meltwater produced at the snow surface of a dry snowpack has a greater impact on emissions at shorter wavelengths with shallower penetration depths than on longer wavelengths. Emissions from wet snow are also less polarized than those of dry snow. The Cross Polarization Gradient Ratio XPGR is given as:

$$XPGR = \frac{Tb_{19H} - Tb_{37V}}{Tb_{19H} + Tb_{37V}} \tag{2.1}$$

The Tb_f values refer to the daily brightness temperature measurement at frequency f (with the polarization specified as well). When this ratio is above a specific threshold then the surface is assumed to be melting. Previous literature values were used for these thresholds, which are -0.0265 for observations from SMMR and -0.0158 for SMM/I (Abdalati and Steffen, 1997). The threshold value used here for SSMIS was the same as for SSM/I because the sensors have the same frequency and incidence angle.

2.4.6   Active radar detection method

Sentinel-1 SAR images were gathered from Google Earth Engine (2019) and scaled to 1 km resolution. Single polarization Ground Range Detected (GRD) images in Extra Wide

and Interferometric Wide Swath mode were processed in Google Earth Engine (Gorelick et al., 2017). For this region, single polarization images are acquired in the "HH" polarization. Google Earth Engine ingests Level-1 GRD images and automatically uses the Sentinel-1 Toolbox (Veci et al., 2014) to apply a border noise removal, thermal noise removal, and radiometric calibration. Google Earth Engine orthorectifies the image using ASTER DEM (NASA/METI/AIST/Japan Spacesystems, Team, U.A.S, 2019) at latitudes greater than 60°. Then within Google Earth Engine we resampled the images to 125 m resolution using nearest-neighbor interpolation and then rescaled the images from there to 1 km resolution using mean-values. While 1 km is quite coarse for Sentinel-1 SAR data, it is much finer than the 25 km passive pixels it was compared with. Any issues of mixed melt in the 1 km SAR pixels will certainly mean mixed melt in the 25 km passive pixel as well.

Scene geometry had to be accounted for and any erroneous data were removed. Backscatter values below -28 dB were automatically removed. For each image an automatic correction was applied to remove unrealistic data in the form of nonphysical dark bands which sometimes appeared near the edge of a SAR swath. Any exact backscatter value which occurred in more than 5% of a single image was removed as erroneous data. The Extra Wide images were also found to require an additional antenna pattern correction because backscatter decreased with off-nadir angle α. A first order linear angular correction with correction factor c was applied to flatten the backscatter values out to their 32° value, which is approximately the middle of the swath. The factor c was found to be -0.17 dB degree^{-1} by following the slope of the maximum detected backscatter values with angle. Further explanation of this residual antenna pattern is given in the Supplementary Material. The following correction was applied to the backscatter σ of Extra-Wide swath images:

$$\sigma^* = \sigma - (\alpha - 32)c \tag{2.2}$$

Because the major seasonal variations in SAR backscatter are primarily the result of liquid water content, SAR melt detection methods typically use a simple threshold for backscatter

19

decrease compared to the average of dry snow (Nagler and Rott, 2000). These methods are based on theory and direct observations of the behavior of C-band and Ku-band active radar measurements over dry and wet snow.

Each 1 km SAR pixel was assumed to be melting if the backscatter in that pixel was below a threshold decrease from the winter mean backscatter. The winter mean backscatter was the mean backscatter of observations from July through October. For C-band radar a threshold change of -3 dB (Luckman et al., 2014, Nagler and Rott, 2000 and Wismann, 2000) or -2.8 dB (Ashcraft and Long, 2006) has been found to be effective for detecting melt water on firn on ice sheets and ice shelves. We used a 3 dB decrease threshold relative to the dry firn backscatter. This lines up closely with theoretical results and direct observations (Stiles and Ulaby, 1980). Additional analysis using a -2 dB threshold instead is provided in the Supplementary material.

Changes in scene geometry can account for more than 5 dB of variation (Fig. 2.1), and therefore viewing geometry must be taken into account. The ASTER DEM used by Google Earth Engine for SAR image orthorectification is known to have relatively limited accuracy on ice sheets (Tachikawa et al., 2011), and this increases the difficulty of comparing Sentinel-1 images from one scene geometry to another. Therefore instead of using the same backscatter value to detect melt for all geometries, the winter average backscatter values were only calculated for images with the same viewing geometry, and then a -3 dB melt threshold was found for each different image geometry. If a time series of images with a new scene geometry began during summer months rather than winter, then it was impossible to detect the backscatter change compared to the preceding winter. Here if a particular geometry did not have at least four observations during the previous winter, it was not used in melt quantification. Additionally, the maximum Noise Equivalent Sigma Zero (NESZ) for Sentinel-1 is -22 dB (Geudtner et al., 2014). If the backscatter melt threshold was -22 dB or below, then all data from that pixel in that orbit geometry were removed.

At the mixed pixel sites the elevation of each 1 km SAR pixel was also recorded. A bilinear

Table 2.1: Mean annual melt days from passive microwave melt detection methods, 1979/80–2018/19, excluding 1987/88.

Site	W30K	W3S	KMean	XPGR
L1	72	72	64	50
L2	71	71	63	47
L3	73	71	63	44
L4	57	54	49	34
W1	102	92	89	72
G1	72	68	66	59

interpolation of the RAMP2 DEM (Liu et al., 2015) was used to classify the elevation of each 1 km SAR pixel. The 1 km resolution may be too coarse to resolve some topographic features, but it was more than sufficient for demonstrating heterogeneity in both topography and the melt detected from SAR imagery when compared to passive microwave pixels.

2.5   Results

Passive microwave melt detection results for each of the uniform sites are given in Table 1. Melt results from 1987/88 were not used because there are 42 consecutive days of missing data during December and January. The W30K method consistently found the highest number of melt days, with W3S not far behind. The KMean method results were always in between the highest and lowest number of melt days, and the XPGR method found the fewest melt days per year. On average the W30K method detected 48% more melt days per year than the XPGR method. On the Wilkins Ice Shelf in particular this resulted in mean melt season lengths which were found to be approximately two and a half months in length from XPGR but approximately three and a half months with W30K.

2.5.1   Comparison results at uniform sites

SAR melt detection was compared to passive microwave melt detection methods in the absence of true ground truth data in order to assess the passive microwave methods. Coincident passive and active radar observations are shown in Fig 2.3 to highlight examples of

agreement and disagreement between passive methods. At the L1 point in 2016/17 there was a clear melt season that lasted a couple months in length and all the passive methods, except possibly XPGR, showed good agreement. However, at L4 in 2017/18 the passive melt detection methods were much more divergent. During the summer months at that site the passive microwave time series lacked a jump in brightness temperatures and there was little decrease in backscatter values, both indicating that there was likely very little melt. The passive microwave melt detection results ranged from 60 days of melt from W30K to zero days from XPGR.

The passive and active radar results were further compared quantitatively. The melt determination of the 1 km SAR pixels were compared to the result of the corresponding passive microwave pixel for that day. This produced four possible cases for each SAR observation, since melt or no melt can be found using SAR and a given passive microwave melt detection algorithm. Table 2 gives confusion matrices, also called 2 × 2 contingency tables, which show the occurrence of each of these four cases for each of the passive melt detection algorithms. This comparison used data over November through March for the austral summers for 2016/17, 2017/18, and 2018/19, and the total sample size was 3.0 million. 96.6% of the total year round melt detected by SAR for these years occurred during the November through March period.

Several useful binary comparison statistics are found from the confusion matrices. The specificity is the likelihood of the passive melt algorithm to detect no melt when the active method is not melting and the sensitivity is the likelihood of the passive melt algorithm to detect melt when the active radar analysis indicates melt. Informedness is the sum of specificity and sensitivity minus 1. It is a measure of whether the test is making accurate and informed decisions rather than taking random guesses. The agreement is the total likelihood of the passive and active melt determinations to agree with one another. Finally, the Matthews Correlation Coefficient (MCC) is a correlation coefficient appropriate for binary datasets.
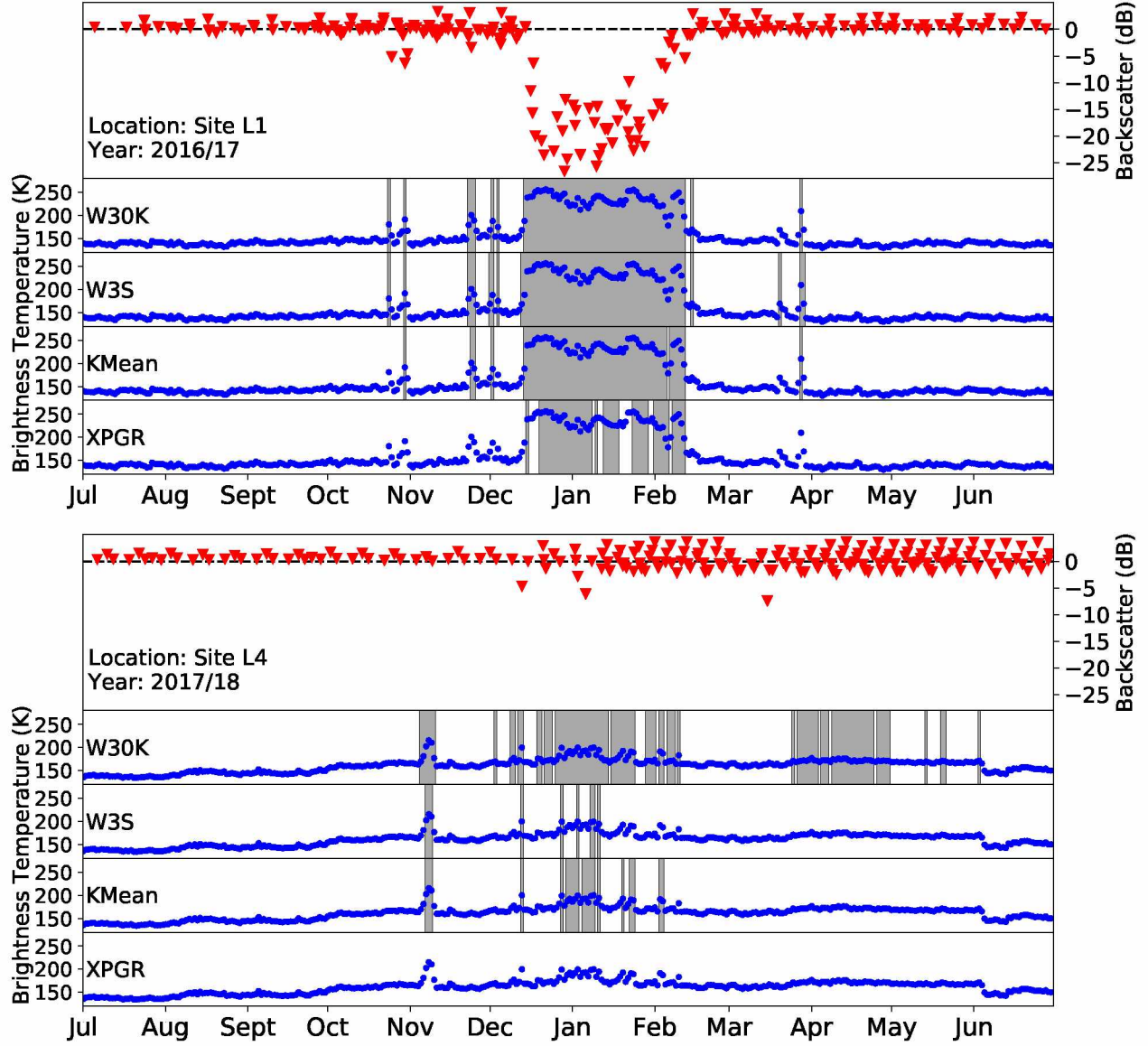
Figure 2.3: Comparison of passive microwave (19 GHz horizontal, 25×25 km^2 pixel) and observed SAR (1 km^2 pixel) measurements at single location. Melt determinations from each of the four passive methods given by gray shaded regions. Small blue dots indicate brightness temperature, red triangles indicate backscatter.

Table 2.2: Confusion matrices comparing passive (P) microwave melt detection and SAR melt detection (A). Data includes all November through March observations of the 2016/17–2018/19 melt seasons from all six uniform sites (Fig. 2). During this time period, 33.7% of all active measurements are melt. Each cell shows the percentage and total occurrences of these cases. Each table gives the sensitivity (Sens), specificity (Spec), informedness (Inf) agreement (Agr), and Matthews Correlation Coefficient of each melt detection method.

W30K	A melt	A no melt
P melt	28.9% 863464	10.6% 316796
P no melt	4.8% 143884	55.7% 1663076

Sens=0.857, Spec=0.840, Inf=0.697,
Agr=0.846, MCC=0.674

W3S	A melt	A no melt
P melt	28.4% 847571	8.9% 265077
P no melt	5.3% 159777	57.4% 1714795

Sens=0.841, Spec=0.866, Inf=0.708,
Agr=0.858, MCC=0.692

KMean	A melt	A no melt
P melt	27.8% 829808	6.4% 190757
P no melt	5.9% 177540	59.9% 1789115

Sens=0.824, Spec=0.904, Inf=0.727,
Agr=0.877, MCC=0.725

XPGR	A melt	A no melt
P melt	23.8% 711780	0.9% 26184
P no melt	9.9% 295568	65.4% 1953688

Sens=0.707, Spec=0.987, Inf=0.693,
Agr=0.892, MCC=0.760

Both informedness and MCC were used here because they have an unbiased treatment of datasets with a highly disproportionate frequency of positive or negative binary results. The informedness and MCC give equal weight to the positive result identification "success" rate and negative identification "success" rate, as well as to the false positive and false negative "failure" rates. In this dataset, the negative result was somewhat more common as the active radar melt detection found no melt in 66.3% of the samples. The MCC is an indicator of which method is better at both detecting melt and detecting no melt, and it is not simply a measure of method agreement.

The comparison statistics in Table 2 illuminates a number of characteristics of the results. The W30K method was most likely to overcount melt compared to active radar analysis, and was the only method with a sensitivity higher than its specificity, meaning it has the least accuracy when detecting no melt. In addition, W30K had the lowest overall agreement with active radar. This was partly due to the higher prevalence of no melt in the dataset, but the MCC was also the lowest. XPGR was most likely to undercount melt compared to SAR, and also had the highest agreement and highest MCC. The KMean method had the second highest agreement and MCC, and was less likely than XPGR to undercount melt days. Overall the instances where the KMean method found no melt but the SAR method did find melt occurred approximately as frequently as instances where the KMean method found melt but SAR did not (5.9% vs 6.4%, respectively). Therefore the KMean method was most accurate to quantifying the total area×day melt index of the SAR results. The KMean method also had the highest informedness, and both of these imply that the KMean method was the most accurate at determining total annual melt days.

This analysis was also performed for SAR melt detection with a a -2 dB threshold to detect melt instead of the -3 dB threshold. Confusion matrix results are given in Supplementary Materials. Results of that analysis are similar, with W30K method having the lowest agreement and MCC, and the KMean method demonstrating the highest agreement.

2.5.2 Mixed pixel results

Satellite passive microwave sensors observe each 25×25 km^2 pixel as a single data point, yet higher resolution imagery often shows a much more detailed tapestry. Melt can vary on small scales geographically, especially over more complex topography. Fig 2.4 shows how non-uniform melt in a single passive microwave pixel on the edge of an Antarctic Peninsula ice shelf can be over a melt season. While the exact transition between not-melting and melting is difficult to visualize in the SAR images in Fig 2.4, the white colors represent surfaces with backscatter values near zero which are unlikely to be melting, and the much darker shades represent surfaces with much more negative backscatter values indicating melt.

Distinct regions of melting and non-melting over the melt season are clear in the SAR images in Fig 2.4, yet passive microwave methods can only indicate melt or no melt for the entire 625 km^2 pixel. The passive brightness temperatures did jump during summer, indicating melt in this pixel, however this brightness temperature increase was much smaller than some sites with clearer melt signals, such as Fig 2.1A. The KMean melt algorithm found that this pixel had 87 days of melt over the 2016/17 melt year, with the main melt season being 73 days from early December through mid-February. The SAR imagery and SAR time series showed that the ice shelf had melt during the entire melt season, whereas higher elevations saw far fewer days of melt.

Passive and active melt detection results were compared for the four mixed pixel sites, whose locations are given in Fig. 2. As expected, the passive and active melt detection methods had lower correlation and agreement over 2016–2019 than the uniform sites. The total agreement between passive and active methods was between 0.78 and 0.79 for each method, with KMean having the slightly highest agreement. The Matthews Correlation Coefficients between passive and active methods were 0.55 for W30K, 0.54 for W3S, 0.55 for KMean, and 0.48 for XPGR. The XPGR method correctly identified a positive melt result with respect to active radar (sensitivity) only 57% of the time, while W30K performed best in this metric at 81% of the time. The full comparison and confusion matrices for passive radar

26
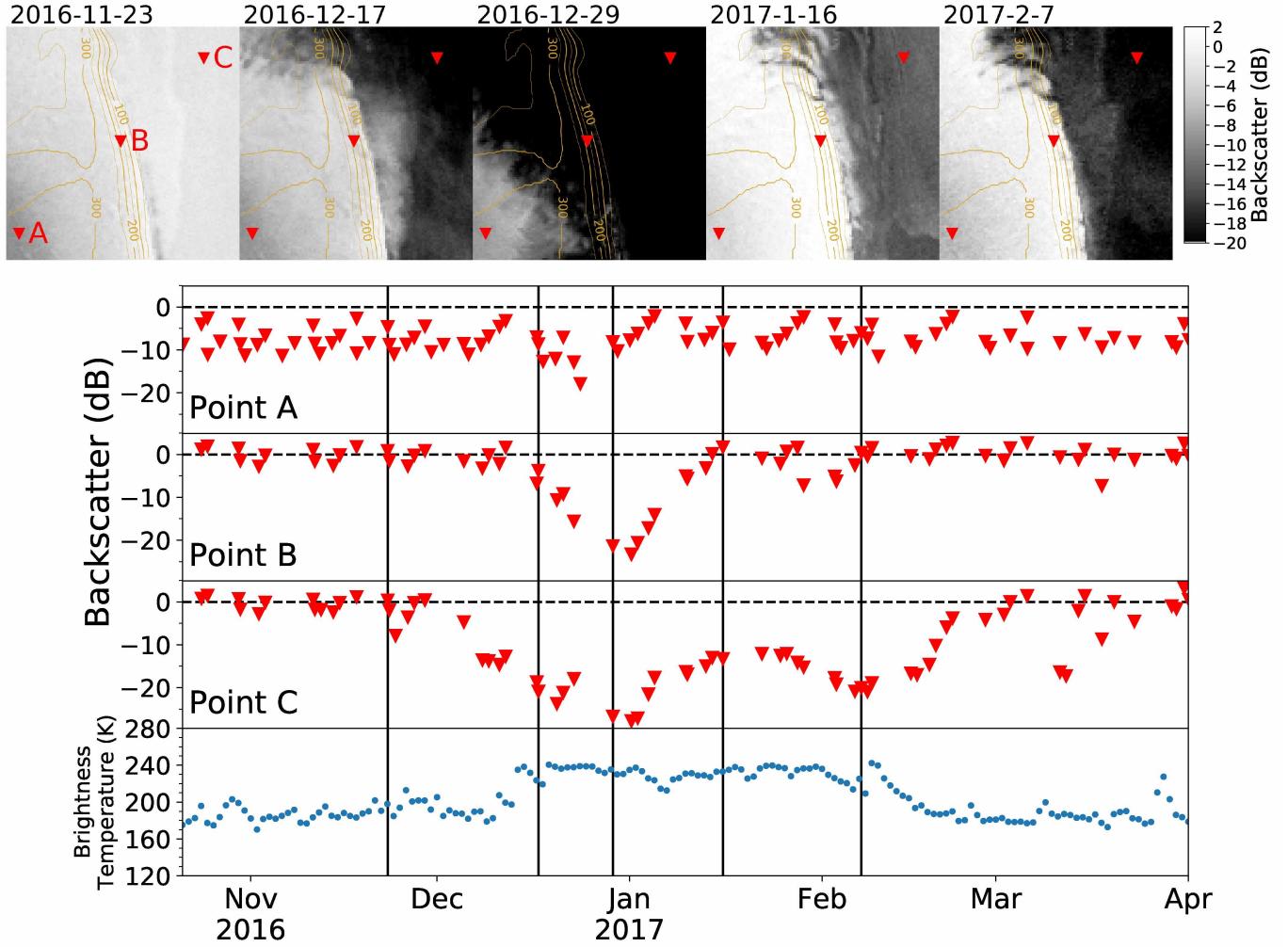
Figure 2.4: Time series of SAR backscatter for a single passive microwave mixed pixel located at site MP4 on the western edge of George VI Ice Shelf (Fig. 2) over the 2016/17 melt season. Bottom plot shows the passive microwave time series. Top panels show Sentinel-1 images of site over the melt season. The spatial resolution is 250 m. The three markers, A, B, and C, correspond to sites of the SAR time series shown below. Black vertical lines indicate where each image lies in the time series. Elevation contours are given in yellow at a spacing of 50 m. Elevations of points are A: 313 m a.s.l., B: 212 m a.s.l, C: 28 m a.s.l.

and SAR melt detection at mixed pixel sites are provided in the Supplemental Materials.

2.6 Discussion

2.6.1 Uniform pixels

The four passive microwave melt detection methods provide such a spread of results that it is difficult to quantify melt days or long-term trends without further considerations to the accuracy of each method. The XPGR method had the highest agreement with the active radar melt detection, but that was partly because it had the highest sensitivity, meaning that it nearly always agreed with active "no melt" identifications and there were significantly less "melt" than "no melt" cases in the active dataset. The XPGR method also had the highest correlation to the active radar, but because it detected much less melt than other methods it is worth further exploring those results.

The XPGR method was routinely late to detect the onset of melt on Antarctic Peninsula ice shelves compared to the other methods, as demonstrated in Fig 2.5. The vertical 37 GHz signal originates from a shallower layer than the 19 GHz horizontal signal. Buried ice lenses block more upwelling radiation at 19 GHz horizontal than 37 GHz vertical (Montpetit et al., 2013 and Rutter et al., 2014), and the firn on these ice shelves has many ice lenses in it. Therefore it is likely that at the beginning of the melt season when there are low moisture contents at the surface the 37 GHz brightness temperature will increase much more substantially than the 19 GHz measurement. This would cause the XPGR value (Eq. 1) to decrease and the method would be less likely to surpass the threshold required to detect melt. Such an effect would be strongly dependent on the firn stratigraphy and ice lens profile, which can change over decades.

In these comparisons the SAR melt determination was treated as close to ground truth measurements as can be available. C-Band radar operates at a different wavelength than the passive microwave sensors employed here and therefore it does have a different penetration depth and surface interaction properties. The methods for melt determination attempt to
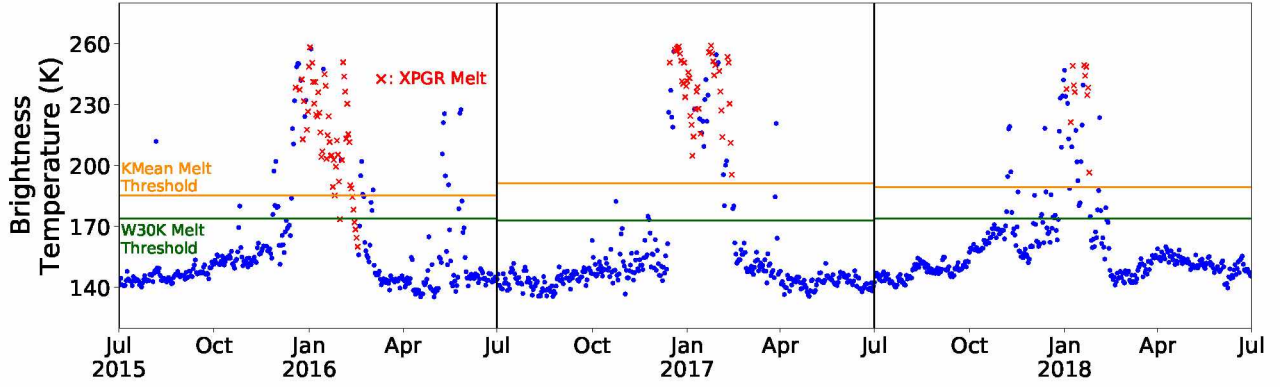
Figure 2.5: Passive microwave method melt determinations for single pixel. Pixel location is the same as Fig 2.1A on Larsen C Ice Shelf. Horizontal lines indicate the melt temperature threshold for one melt detection method, and the red 'x' marks indicate where the XPGR method detects melt. (For interpretation of the references to color in this figure legend, the reader is referred to the web version of this article.)

address the unique properties of their respective data sources and datasets. Additionally, the agreement of passive melt detection methods to SAR melt detection were significantly higher than similar comparisons of passive microwave melt detection with 2 m air temperature melt determinations from Automated Weather Stations found by Liang et al. (2013).

Several differences remain however. The overpass time of day can vary between passive and active observations, which was not accounted for here. Additionally, the vastly different resolutions of passive and active observations present new challenges and insights. Across every passive microwave pixel at the six uniform sites used in this comparison, an average of 98.9% of the 1 km SAR pixels shared the same melt or no melt determination within their respective 25 × 25 km² passive pixel. Therefore that is the maximum agreement possible between the passive and active methods due to their difference in resolution. When more than 50% of the SAR pixels detected melt within a passive microwave pixel, then that internal agreement dropped and to an average of 96.5% of the SAR pixels indicating melt. This internal agreement is high enough to suggest that melt is sufficiently uniform in space on Antarctic Peninsula ice shelves for the application of passive microwave melt detection methods.

29

2.6.2 Mixed pixels

For mixed pixels, the internal melt or no melt agreement of all 1 km SAR pixels within a single 25 km passive microwave pixel was 93.0% on average, which is somewhat lower than the internal agreement at the uniformly melting sites. The difference was far greater however when more than half of the passive pixel was melting, in which case the average internal agreement was only 73.5%. These numbers illustrate the limitations with using 25 km passive microwave measurements to detect melt in mixed pixels, and imply a necessity for using a higher resolution measurements in such regions. If only part of the pixel is physically melting then it also raises an important question of what a positive or negative passive microwave melt result physically means.

Mixed melt pixels are common on the Antarctic Peninsula and they present a clear problem for passive microwave melt detection. The abundance of mixed passive microwave pixels on the Antarctic Peninsula is further illustrated in Fig 2.6. The low (dark) SAR backscatter values at low elevations are indicative of melt, the very high backscatter surfaces at mid elevations show percolation zone surfaces which are not presently melting, and the low backscatter values at high elevations are typical of dry firn that rarely or never melts.

In the scene in Fig. 2.6 the 25×25 km^2 passive pixels on flat ice shelves are nearly entirely melting, but nearly every other pixel is mixed. On either side of the George VI Ice Shelf melt is absent at elevations only a few hundred meters higher. Spatially, the melt disappears within a distance of a few kilometers. In the interior of the Wilkins Ice Shelf region, melt is initially still found with increasing elevation, but then abruptly gives way to dry firn.

As expected, there is a spatial trend of less melt and fewer melt days with increasing elevation. The melt likelihood of individual 1 km SAR pixels showed a negative correlation with respect to elevation (Fig. 2.7). That statement is an obvious observation because temperature generally decreases with elevation, but the sharp relief of the Antarctic Peninsula, especially when compared to the gradual slopes of the percolation zones in Greenland, rein-
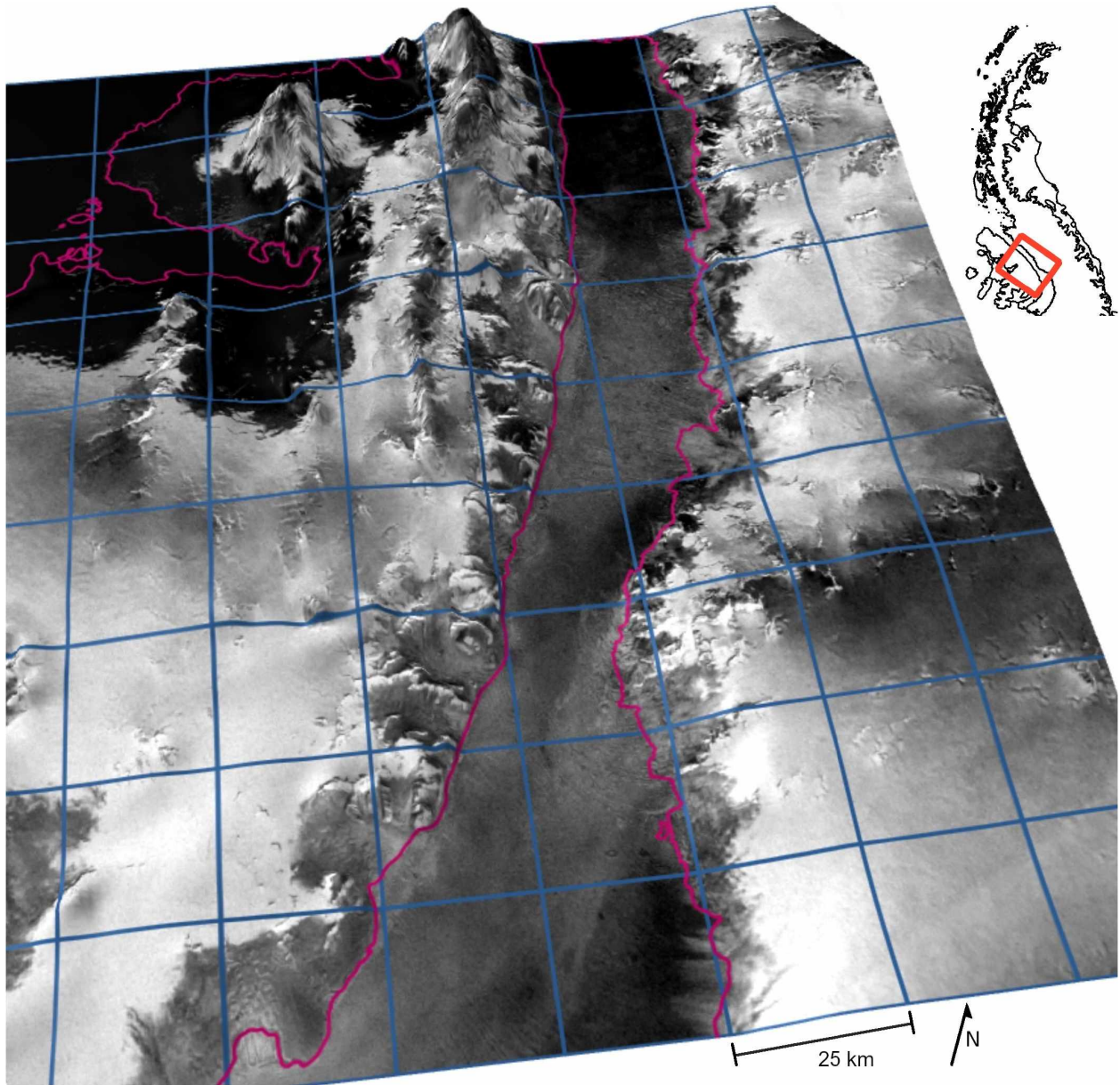
Figure 2.6: Oblique view of a summer Sentinel-1 image of the southwest Antarctic Peninsula with DEM. 25 km resolution passive microwave pixel outlines are shown in blue. RAMP2 DEM was used with a vertical exaggeration factor of 10. SAR image was from 2018-02-04, at 250 m resolution. The colorscale ranges from -20 dB (black) to 2 dB (white), with the same colorscale as Fig. 2.4. The George VI Ice Shelf runs through the middle of the scene while the Wilkins Ice Shelf is in the top left corner. Elevations range from 6 m to 2430 m a.s.l. Coastlines are given in pink (SCAR, 2017).
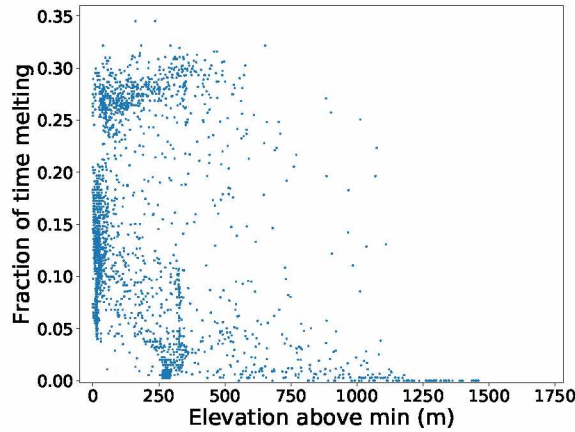
Figure 2.7: Melt likelihood of all SAR pixels at the four mixed pixel sites (MP in Fig. 2.2) as a function of elevation, from 2016 to 2019. Each point represents the ratio of instances of melt to total observations of each 1 km SAR pixel. Elevations are measured relative to lowest elevation in the respective 25 km passive pixel.

forces the necessity of remaining conscious of this trend when designing passive microwave surveys for the Antarctic Peninsula. Large topographic variation can be present in individual passive pixels and serves as a clear indication that the pixel might not be expected to melt uniformly. A DEM can be a reasonable tool when choosing which 25 km passive microwave pixels to study.

2.7 Conclusion

The four different passive microwave algorithms employed here detect numbers of annual melt days which vary by up to 30 days at our study sites on Antarctic Peninsula ice shelves. The large difference between methods makes it difficult to have confidence in the melt results and it emphasizes the need for independent ground truth measurements. In the comparison to SAR melt results, the XPGR and the KMean method were superior to the W30K and W3S methods. XPGR performed best at identifying melt at any given time and had the highest agreement and correlation with SAR results. However, it was strongly biased to undercount total melt days and often missed the timing of the onset of melt on Antarctic Peninsula ice shelves. In contrast the KMean method proposed here had the second highest

agreement and correlation, but it showed the best accuracy at determining the total melt days. For that reason the KMean method is recommended for quantifying total melt days.

SAR melt detection results showed that passive microwave melt detection is suitable for melt detection on Antarctic Peninsula ice shelves. On the flat ice shelf sites used in this study, results illustrated that melt patterns are spatially very uniform, and the 25 km passive pixels were nearly always either all melting or all not melting. The highest agreement between passive and active methods at the uniformly melting ice shelf sites was 95%. Additionally, these methods for evaluating passive microwave melt detection methods using SAR observations can easily be replicated for application to other regions, such as Greenland.

SAR results identified which regions melt heterogeneously at the sub passive microwave pixel scale. High spatial variability of melt is often related to topographic variability. The edges of Antarctic Peninsula ice shelves often have high elevation gradients, causing many mixed pixels at the edges of ice shelves. Using a DEM to identify elevation variation is a viable strategy to determine if a surface is likely to uniformly melt on the Antarctic Peninsula. More modern passive microwave measurements with higher resolution may alleviate some of these issues, and high repeat time series from Sentinel-1 SAR imagery for 2016 onwards provides significantly higher resolution for robust melt determinations.

2.8 Acknowledgements

2.9 References

Abdalati, W., Steffen, K., 1995. Passive microwave-derived snow melt regions on the greenland ice sheet. Geophysical Research Letters 22, 787–790.

Abdalati, W., Steffen, K., 1997. Snowmelt on the greenland ice sheet as derived from passive microwave satellite data. Journal of Climate 10, 165–175.

Ashcraft, I.S., Long, D.G., 2006. Comparison of methods for melt detection over greenland using active and passive microwave measurements. International Journal of Remote Sensing 27, 2469–2488.

Chang, T., Gloersen, P., Schmugge, T., Wilheit, T., Zwally, H., 1976. Microwave emission from snow and glacier ice. Journal of Glaciology 16, 23–39.

Cook, A.J., Vaughan, D.G., 2010. Overview of areal changes of the ice shelves on the antarctic peninsula over the past 50 years. The Cryosphere 4, 77–98.

De Angelis, H., Skvarca, P., 2003. Glacier surge after ice shelf collapse. Science 299, 1560–1562.

Engine, G.E., 2019. Contains modified Copernicus Sentinel data 2016-2019. Processed by ESA.

Fahnestock, M.A., Abdalati, W., Shuman, C.A., 2002. Long melt seasons on ice shelves of the antarctic peninsula: an analysis using satellite-based microwave emission measurements. Annals of Glaciology 34, 127–133.

Fettweis, X., Gallée, H., Lefebre, F., Van Ypersele, J.P., 2006. The 1988–2003 greenland ice sheet melt extent using passive microwave satellite data and a regional climate model. Climate dynamics 27, 531–541.

Fettweis, X., Tedesco, M., van den Broeke, M., Ettema, J., 2011. Melting trends over the greenland ice sheet (1958–2009) from spaceborne microwave data and regional climate models. The Cryosphere 5, 359–375.

Geudtner, D., Torres, R., Snoeij, P., Davidson, M., Rommen, B., 2014. Sentinel-1 system capabilities and applications, in: 2014 IEEE Geoscience and Remote Sensing Symposium, IEEE. pp. 1457–1460.

Gloersen, P., Francis, E.A., 2003. Nimbus-7 smmr antenna temperatures. NASA National Snow and Ice Data Center Distributed Active Archive Center, Version 1, South 18H and 37V. Doi: https://doi.org/10.5067/C8ZJDDHZAS59.

Gorelick, N., Hancher, M., Dixon, M., Ilyushchenko, S., Thau, D., Moore, R., 2017. Google earth engine: Planetary-scale geospatial analysis for everyone. Remote Sensing of Environment 202, 18–27.

Haran, T., Bohlander, J., Scambos, T., Painter, T., Fahnestock, M., 2014, updated 2019. Modis mosaic of antarctica 2008-2009 (moa2009) image map, version 1. NSIDC: National Snow and Ice Data Center Distributed Active Archive Center, Version 1 South 19H and 37V. Doi: https://doi.org/10.7265/N5KP8037.

Joshi, M., Merry, C.J., Jezek, K.C., Bolzan, J.F., 2001. An edge detection technique to estimate melt duration, season and melt extent on the greenland ice sheet using passive microwave data. Geophysical Research Letters 28, 3497–3500.

Liang, L., Guo, H., Li, X., Cheng, X., 2013. Automated ice-sheet snowmelt detection using microwave radiometer measurements. Polar Research 32, 19746.

Liu, H., Jezek, K.C., Li, B., Zhao, Z., 2015. Radarsat antarctic mapping project digital elevation model. NASA National Snow and Ice Data Center Distributed Active Archive Center, Version 2, 200m. Doi: http://dx.doi.org/10.5067/8JKNEW6BFRVD.

Liu, H., Wang, L., Jezek, K.C., 2006. Spatiotemporal variations of snowmelt in antarctica derived from satellite scanning multichannel microwave radiometer and special sensor microwave imager data (1978–2004). Journal of Geophysical Research: Earth Surface 111.

Luckman, A., Elvidge, A., Jansen, D., Kulessa, B., Munneke, P.K., King, J., Barrand, N.E., 2014. Surface melt and ponding on larsen c ice shelf and the impact of föhn winds. Antarctic Science 26, 625–635.

MacAyeal, D.R., Scambos, T.A., Hulbe, C.L., Fahnestock, M.A., 2003. Catastrophic ice-shelf break-up by an ice-shelf-fragment-capsize mechanism. Journal of Glaciology 49, 22–36.

Maslanik, J., Stroeve, J., 1999. Near-real-time dmsp ssm/i-ssmis daily polar gridded brightness temperatures. NASA National Snow and Ice Data Center Distributed Active Archive Center, Version 1 South 19H and 37V. Doi: https://doi.org/10.5067/AKQDND71ZDLF.

Meier, W.N., Wilcox, H., Hardman, M.A., Stewart, J.S., 2019. Dmsp ssm/i-ssmis daily polar gridded brightness temperatures. ASA National Snow and Ice Data Center Distributed Active Archive Center, Version 5, South 19H and 37V. Doi: https://doi.org/10.5067/QU2UYQ6T0B3P.

Montpetit, B., Royer, A., Roy, A., Langlois, A., Derksen, C., 2013. Snow microwave emission modeling of ice lenses within a snowpack using the microwave emission model for layered snowpacks. IEEE Transactions on Geoscience and Remote Sensing 51, 4705–4717.

Morris, E.M., Vaughan, D.G., 2003. Spatial and temporal variation of surface temperature on the antarctic peninsula and the limit of viability of ice shelves. Antarctic Peninsula Climate Variability: Historical and Paleoenvironmental Perspectives 79, 61–68.

Mote, T.L., Anderson, M.R., Kuivinen, K.C., Rowe, C.M., 1993. Passive microwave-derived spatial and temporal variations of summer melt on the greenland ice sheet. Annals of Glaciology 17, 233–238.

Nagler, T., Rott, H., 2000. Retrieval of wet snow by means of multitemporal sar data. IEEE Transactions on Geoscience and Remote Sensing 38, 754–765.

Nagler, T., Rott, H., Ripper, E., Bippus, G., Hetzenecker, M., 2016. Advancements for snowmelt monitoring by means of sentinel-1 sar. Remote Sensing 8, 348.

Nicolas, J.P., Vogelmann, A.M., Scott, R.C., Wilson, A.B., Cadeddu, M.P., Bromwich, D.H., Verlinde, J., Lubin, D., Russell, L.M., Jenkinson, C., et al., 2017. January 2016 extensive summer melt in west antarctica favoured by strong el niño. Nature communications 8, 15799.

Pritchard, H., Ligtenberg, S., Fricker, H., Vaughan, D., Van den Broeke, M., Padman, L., 2012. Antarctic ice-sheet loss driven by basal melting of ice shelves. Nature 484, 502.

Rignot, E., Casassa, G., Gogineni, P., Krabill, W., Rivera, A., Thomas, R., 2004. Accelerated ice discharge from the antarctic peninsula following the collapse of larsen b ice shelf. Geophysical Research Letters 31.

Rutter, N., Sandells, M., Derksen, C., Toose, P., Royer, A., Montpetit, B., Langlois, A., Lemmetyinen, J., Pulliainen, J., 2014. Snow stratigraphic heterogeneity within ground-based passive microwave radiometer footprints: Implications for emission modeling. Journal of Geophysical Research: Earth Surface 119, 550–565.

Scambos, T., Fricker, H.A., Liu, C.C., Bohlander, J., Fastook, J., Sargent, A., Massom, R., Wu, A.M., 2009. Ice shelf disintegration by plate bending and hydro-fracture: Satellite observations and model results of the 2008 wilkins ice shelf break-ups. Earth and Planetary Science Letters 280, 51–60.

Scambos, T.A., Bohlander, J., Shuman, C.u., Skvarca, P., 2004. Glacier acceleration and thinning after ice shelf collapse in the larsen b embayment, antarctica. Geophysical Research Letters 31.

Scambos, T.A., Hulbe, C., Fahnestock, M., Bohlander, J., 2000. The link between climate warming and break-up of ice shelves in the antarctic peninsula. Journal of Glaciology 46, 516–530.

SCAR, 2017. Antarctic digital database coastlines. British Antarctic Survey, Cambridge.

Shi, J., Dozier, J., 1995. Inferring snow wetness using c-band data from sir-c's polarimetric synthetic aperture radar. IEEE transactions on geoscience and remote sensing 33, 905–914.

Snapir, B., Momblanch, A., Jain, S., Waine, T.W., Holman, I.P., 2019. A method for monthly mapping of wet and dry snow using sentinel-1 and modis: Application to a himalayan river basin. International Journal of Applied Earth Observation and Geoinformation 74, 222–230.

Spacesystems, N., Team, U.A.S., 2019. Aster global digital elevation model. NASA EOSDIS Land Processes DAAC, V003. Doi: https://doi.org/10.5067/ASTER/ASTGTM.003.

Stiles, W.H., Ulaby, F.T., 1980. The active and passive microwave response to snow parameters: 1. wetness. Journal of Geophysical Research: Oceans 85, 1037–1044.

Tachikawa, T., Kaku, M., Iwasaki, A., Gesch, D.B., Oimoen, M.J., Zhang, Z., Danielson, J.J., Krieger, T., Curtis, B., Haase, J., et al., 2011. ASTER global digital elevation model version 2-summary of validation results. Technical Report. NASA.

Tedesco, M., 2007. Snowmelt detection over the greenland ice sheet from ssm/i brightness temperature daily variations. Geophysical Research Letters 34.

Tedesco, M., 2009. Assessment and development of snowmelt retrieval algorithms over antarctica from k-band spaceborne brightness temperature (1979–2008). Remote Sensing of Environment 113, 979–997.

Tedesco, M., Fettweis, X., Mote, T., Wahr, J., Alexander, P., Box, J., Wouters, B., 2013. Evidence and analysis of 2012 greenland records from spaceborne observations, a regional climate model and reanalysis data .

Torinesi, O., Fily, M., Genthon, C., 2003. Variability and trends of the summer melt period of antarctic ice margins since 1980 from microwave sensors. Journal of Climate 16, 1047–1060.

Trusel, L.D., Frey, K.E., Das, S.B., 2012. Antarctic surface melting dynamics: Enhanced perspectives from radar scatterometer data. Journal of Geophysical Research: Earth Surface 117.

Trusel, L.D., Frey, K.E., Das, S.B., Karnauskas, K.B., Munneke, P.K., Van Meijgaard, E., Van Den Broeke, M.R., 2015. Divergent trajectories of antarctic surface melt under two twenty-first-century climate scenarios. Nature Geoscience 8, 927.

Turner, J., Lu, H., White, I., King, J.C., Phillips, T., Hosking, J.S., Bracegirdle, T.J., Marshall, G.J., Mulvaney, R., Deb, P., 2016. Absence of 21st century warming on antarctic peninsula consistent with natural variability. Nature 535, 411.

Veci, L., Lu, J., Prats-Iraola, P., Scheiber, R., Collard, F., Fomferra, N., Engdahl, M., 2014. The sentinel-1 toolbox, in: Proceedings of the IEEE International Geoscience and Remote Sensing Symposium (IGARSS), pp. 1–3.

Wismann, V., 2000. Monitoring of seasonal snowmelt on greenland with ers scatterometer data. IEEE Transactions on Geoscience and Remote Sensing 38, 1821–1826.

Zhou, C., Zheng, L., 2017. Mapping radar glacier zones and dry snow line in the antarctic peninsula using sentinel-1 images. Remote Sensing 9, 1171.

Zwally, H.J., Abdalati, W., Herring, T., Larson, K., Saba, J., Steffen, K., 2002. Surface melt-induced acceleration of greenland ice-sheet flow. Science 297, 218–222.

Zwally, H.J., Fiegles, S., 1994. Extent and duration of antarctic surface melting. Journal of Glaciology 40, 463–475.

Table 2.3: Confusion matrices comparing passive (P) microwave melt detection and SAR melt detection (A) at mixed pixel sites. Data refer to November through March of the austral summers of 2016/17–2018/19 and include all four mixed sites (Figure 2). Each cell shows the percentage and total occurrences of these cases. Each table gives the sensitivity (Sens), specificity (Spec), informedness (Inf), agreement (Agr), and Matthews Correlation Coefficient of each melt detection method.

W30K	A melt	A no melt
P melt	25.5% 112085	15.8% 69366
P no melt	5.9% 25776	52.8% 231667

Sens=0.813, Spec=0.770, Inf=0.583,
Agr=0.783, MCC=0.549

W3S	A melt	A no melt
P melt	24.8% 108683	15.0% 65700
P no melt	6.6% 29178	53.6% 235335

Sens=0.788, Spec=0.782, Inf=0.570,
Agr=0.784, MCC=0.541

KMean	A melt	A no melt
P melt	24.3% 106520	13.9% 60880
P no melt	7.1% 31341	54.8% 2401555

Sens=0.773, Spec=0.798, Inf=0.570,
Agr=0.790, MCC=0.545

XPGR	A melt	A no melt
P melt	17.9% 78698	8.2% 35821
P no melt	13.5% 59163	60.4% 265214

Sens=0.571, Spec=0.881, Inf=0.452,
Agr=0.784, MCC=0.478

2.10 Supplementary materials

2.10.1 Additional melt detection domparisons

Results of the comparison of passive and active melt detection methods are provided for the mixed pixel sites in Table 2.3. These results are given in confusion matrices just like Table 2. The agreement and correlations between passive and active radar melt detection methods are lower than at the uniform sites.

An analysis was also performed for passive and active melt detection comparison at the uniform sites using a –2 dB melt threshold for SAR rather than a –3 dB threshold. The results are shown in Table 2.4. –2 dB has been used for both seasonal snow and firn in mountain terrains from Sentinel-1 (Nagler et al., 2016 and Snapir, 2019) and also by Trusel (2012) for detecting melt on ice sheets with Ku-band SAR. Zhou and Zheng (2017) found

40

Table 2.4: Confusion matrices comparing passive (P) microwave melt detection and SAR melt detection (A) where SAR melt detection uses a –2 dB threshold. Data refer to November through March of the austral summers of 2016/17–2018/19 and include all six uniform sites (Figure 2). Each cell shows the percentage and total occurrences of these cases. Each table gives the sensitivity (Sens), specificity (Spec), agreement (Agr), and Matthews Correlation Coefficient of each melt detection method.

W30K	A melt	A no melt
P melt	30.4% 907067	9.1% 273245
P no melt	5.6% 166170	54.9% 1640819

Sens=0.845, Spec=0.857, Inf=0.702,
Agr=0.853, MCC=0.689

W3S	A melt	A no melt
P melt	29.8% 889382	7.5% 223315
P no melt	6.2% 183885	56.6% 1690749

Sens=0.829, Spec=0.883, Inf=0.712,
Agr=0.864, MCC=0.707

KMean	A melt	A no melt
P melt	29.0% 865218	5.2% 155395
P no melt	7.0% 208019	58.9% 1758669

Sens=0.806, Spec=0.919, Inf=0.725,
Agr=0.878, MCC=0.733

XPGR	A melt	A no melt
P melt	24.1% 720452	0.6% 17554
P no melt	11.8% 352785	63.5% 1896510

Sens=0.671, Spec=0.991, Inf=0.662,
Agr=0.876, MCC=0.737

that -4 dB was sufficient to detect melt when using Sentinel-1 on the Antarctic Peninsula.

2.10.2 Description of Extra-Wide Sentinel-1 residual antenna pattern

In this study Sentinel-1 images were processed and scaled in Google Earth Engine. Figure 2.8 shows all backscatter observations with off-nadir angle. There is a great deal of variability at any given angle because the observations come from all times of year and can come from multiple geographic locations. However, there is a suspiciously linear pattern of maximum backscatter with respect to angle, which is unlikely to be a physical characteristic of the surface. This is interpreted to be a residual angle pattern with off-nadir angle dependence.

The correction described in Equation 2 is a first order correction for this antenna pattern. The result of this correction is shown in Figure 2.8C and D. The c value was determined by taking the approximate slope of the backscatter values with angle in Figure 2.8A. This

pattern is not obvious in the Interferometric-Wide images. If such a residual pattern exists, the angle ranges of these acquisitions are not large enough to capture it.

It should also be noted that the angular correction only impacted the qualitative analysis in this study for visualizing SAR images. The angular correction was applied for all Extra-Wide acquisition mode Sentinel-1 images, but it did not impact melt quantifications. Melt was detected by comparing backscatter differences of images of the exact same geometry and viewing angle, and this correction did not change the relative difference in backscatter between those images.
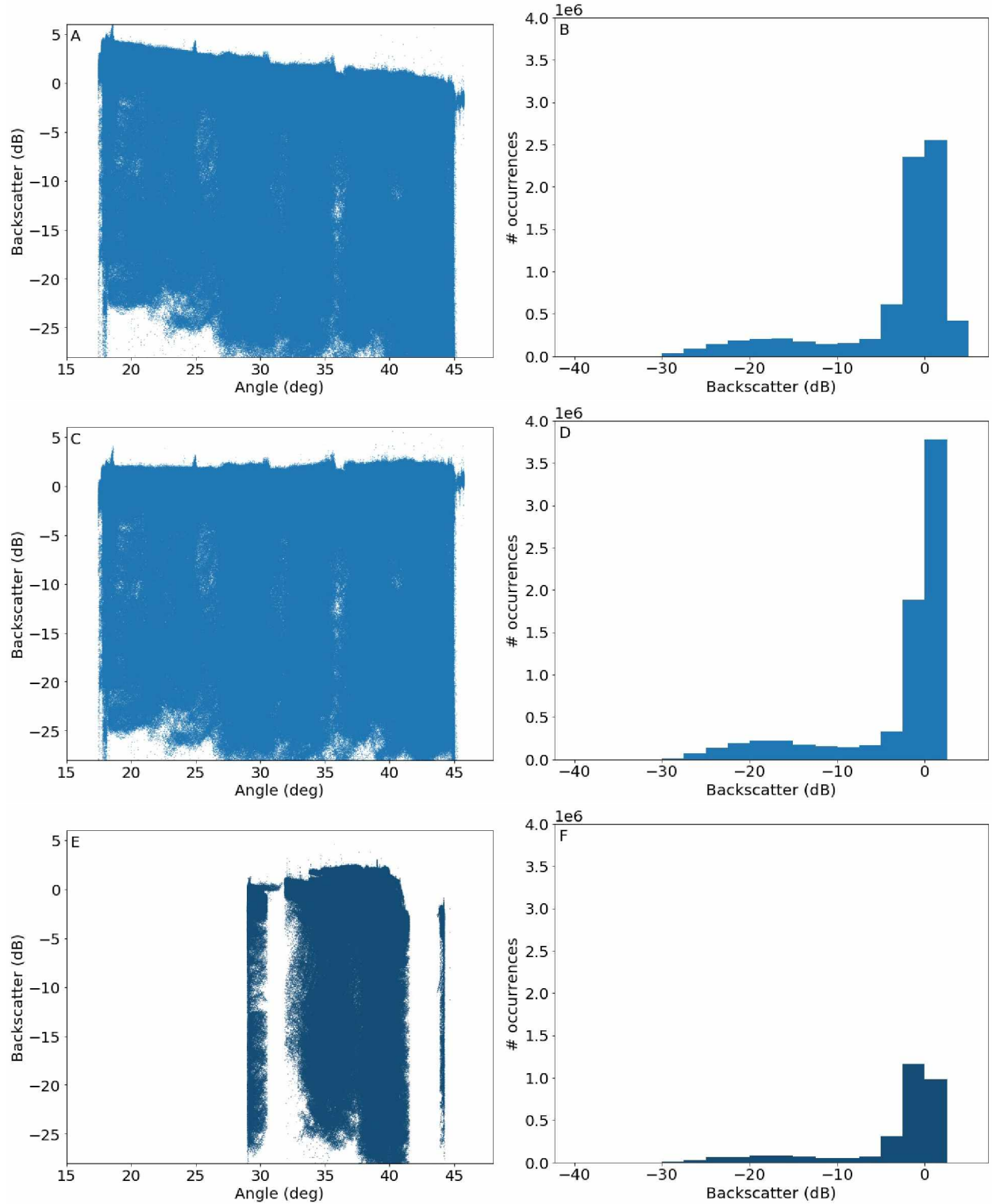
Figure 2.8: Backscatter of all pixels in all Sentinel-1 acquisitions at the uniform sites, processed in Google Earth Engine and scaled to 1km, from July 1, 2016 to June 30, 2019. (A and B) All Extra-Wide acquisitions with no correction for residual antenna pattern. (C and D) Extra-Wide acquisitions after residual antenna pattern correction. (E and F) All interferometric-wide acquisitions, with no additional correction.

2.10.3 References

Nagler, T., Rott, H., Ripper, E., Bippus, G., Hetzenecker, M., 2016. Advancements for snowmelt monitoring by means of sentinel-1 sar. Remote Sensing 8, 348.

Snapir, B., Momblanch, A., Jain, S., Waine, T.W., Holman, I.P., 2019. A method for monthly mapping of wet and dry snow using sentinel-1 and modis: Application to a himalayan river basin. International Journal of Applied Earth Observation and Geoinformation 74, 222–230.

Trusel, L.D., Frey, K.E., Das, S.B., 2012. Antarctic surface melting dynamics: Enhanced perspectives from radar scatterometer data. Journal of Geophysical Research: Earth Surface 117.

Zhou, C., Zheng, L., 2017. Mapping radar glacier zones and dry snow line in the antarctic peninsula using sentinel-1 images. Remote Sensing 9, 1171.

3 Spatial variability and regional trends of Antarctic ice shelf surface melt duration over 1979 - 2020 derived from passive microwave data[4]

Abstract

Passive microwave satellite observations are used to identify the presence of surface meltwater across Antarctica at daily intervals from July 1979 to June 2020, with a focus on ice shelves. Antarctic Peninsula ice shelves have the highest number of annual days of melt, with a maximum of 89 days. Over the entire time period, there are few significant linear trends in days of melt per year. High melt years can be split into two distinct categories, those with high melt days in Dronning Maud Land and Wilkes Land, and those with high melt days in the Antarctic Peninsula and the Bellingshausen Sea sector of West Antarctica. The first pattern coincides with significant negative correlations between melt days and spring and summer Southern Annular Mode. Both patterns also form the primary modes of spatial and annual variability in the dataset observed by Principal Component Analysis. Areas experiencing extended melt for the first time in years tend to show large decreases in subsequent winter microwave emissions due to structural changes in the firn. We use this to identify the impact of novel melt events, particularly over the austral summers of 1991/92 and 2015/16 on the Ross Ice Shelf.

3.1 Introduction

Mass loss of the Antarctic ice sheet has the potential to surpass Greenland in contribution to sea-level rise by 2100 (Pörtner and others, 2019). The majority of potential Antarctic mass loss this century arises from ocean-driven and ice dynamic mechanisms (Golledge and others, 2019), yet surface melt is an increasing component of the mass budget as the atmosphere warms (DeConto and Pollard, 2016). While surface melt is largely restricted to the periphery

---

[4]Reprinted here from: Johnson, A., Hock, R., Fahnestock, M. (2021). Spatial variability and regional trends of Antarctic ice shelf surface melt duration over 1979 - 2020 derived from passive microwave data. *Journal of Glaciology*, 1-14.

of the ice sheet, with a mean annual extent over 2000—2009 of a mere 11% of the total surface area (melt over 1.47 million km^2 , from Trusel and others (2012)), this area is comparable to the entire surface area of the Greenland Ice Sheet (1.7 million km^2). By the year 2100 some regions of Antarctica, especially the Antarctic Peninsula, could have surface melt rates similar to those found across the ablation area of Greenland during 2000–2009 (Bell and others, 2018) and surface melt across the entire continent in 2100 has the potential to equal that of Greenland during 2001–2006 (Trusel and others, 2015). Increasing melt is expected to result in mass loss due to increased runoff (Kittel and others, 2021), and surface melt is also related to dynamic ice loss mechanisms. Thinning ice shelves can collapse entirely due to melt pond driven hydrofracture (Scambos and others, 2009; Banwell and others, 2013) and the thinning and loss of ice shelves can reduce the backstress they provide on grounded ice which leads to glacier acceleration and thinning (e.g. Dupont and Alley, 2005). Surface meltwater reaching the bed has led to increased sliding resulting in acceleration of Antarctic Peninsula outlet glaciers (Tuckett and others, 2019).

Surface melt provides one key point of interaction between the Antarctic ice sheet and Antarctic climate. Over the past 50 years, atmospheric warming has not been uniform across Antarctica (Smith and Polvani, 2017). The Antarctic Peninsula has warmed very rapidly, with near-surface air temperatures at weather stations rising by up to 2.8°C from 1951 to 2000, and then slightly trending downward between 1999 and 2014 (Turner and others, 2016). Near-surface temperature reanalysis has revealed increasing West Antarctica temperatures from 1960 to 2010, while East Antarctica had few statistically significant temperature trends during that period (Nicolas and Bromwich, 2014). The drivers of climate variability can vary from one region to another. One important driver of coastal climate in East Antarctica is the poleward constriction of the Southern Westerly Winds, as measured by the Southern Annular Mode (SAM) (Marshall, 2007). The southward migration of the Southern Westerly Winds, which occurs during the positive SAM phase, has a cooling effect on East Antarctica and the Ross Sea sector of West Antarctica (Mayewski and others, 2009) and a warming effect

on the Antarctic Peninsula. SAM has been trending positive since 1950, and is expected to continue to do so in a warming atmosphere (Bracegirdle and others, 2019). The El Niño Southern Oscillation (ENSO), which is defined by longitudinal pressure and temperature gradients across the Pacific, is known to bring warming and increased accumulation to the Antarctic Peninsula and parts of West Antarctica when in positive phase (El Niño), and the negative phase (La Niña) is associated with decreased accumulation to West Antarctica (Paolo and others, 2018). The Antarctic climate patterns which are known to be related to times of strong ENSO have also been shown to be more intense when SAM was weak or in opposite phase with ENSO (Fogt and others, 2011).

Microwave-band satellite observations have provided data sources with application to the study of Antarctic surface melt. Passive microwave observations from radiometers have been used to quantify melt extent and duration across the entire Antarctic ice sheet and evaluate trends and climate teleconnections (e.g. Zwally and Fiegles, 1994; Torinesi and others, 2003; Picard and others, 2007; Tedesco and Monaghan, 2009), or investigate melt in individual regions of Antarctica (e.g. Fahnestock and others, 2002, and Banwell and others, 2021). From 2001 onwards the rapid-repeat scatterometers QuikSCAT and the Advanced SCATterometer (ASCAT) have been used to quantify melt extent and duration in Antarctica across the entire continent (Trusel and others, 2012; Bothale and others, 2015), or for specific regions (Barrand and others, 2013; Kuipers Munneke and others, 2018), or to quantify melt (Trusel and others, 2013). Similar near-daily melt detection has been shown to be possible for periods after 2014 with time series of high resolution, rapid-repeat Sentinel-1 SAR imagery (Johnson and others, 2020). However, many of the most pronounced melt events occurred during the 1990s, and thus were not covered by these recent active microwave records.

This work uses passive microwave satellite data to derive a 40-year time series of surface melt extent and duration across the Antarctic ice sheet over the period 1979–2020. We focus our analysis on melt on ice shelves because ice shelves provide the most ideal targets for passive microwave detection of melt with their low surface elevation and large extents,

and also because ice shelves are especially susceptible to thinning, retreat and collapse in a warming climate (Gilbert and Kittel, 2021). This study adds an additional decade to previously published passive microwave melt records which allows us to reexamine previously reported trends and teleconnections. In particular, we analyze the characteristics of high melt years and compare these to the primary modes of variability in the spatial extent and duration of melt across all ice shelves. We demonstrate the relationship of the primary mode of variability to SAM. In addition, this work presents a new application of passive microwave time series to detect changes in firn stratigraphy due to abnormally high melt.

3.2   Methods

Snow and firn containing liquid water has a much greater emissivity than dry snow and firn, and therefore passive microwave observations are suitable for identifying the presence of meltwater at or close to a firn/snow surface (Mote and others, 1993). Passive microwave sensors measure upwelling thermal radiation. These observations are reported in brightness temperature (K), which is the temperature of a perfect black body required to produce the measured intensity of emissions.

Passive microwave melt detection methods make a binary assessment about the presence or absence of liquid water and days in which liquid water is detected are referred to as melt days. For each pixel of gridded daily (or every 2 day) passive microwave data in Antarctica, we compute the number of days per year in which melt can be detected (for simplicity henceforth referred to as annual melt days). A melt year here refers to July 1 through June 30 of the following calendar year in order to capture the austral summer. Melt days are quantified for every non-ocean pixel in Antarctica over the melt years 1979/1980 to 2019/20.

Most of the analysis here is focused on melt days on ice shelves. We specifically target pixels defined as having their entire $25{\times}25$ km^2 areal extent being categorized as ice shelf according to a SCAR coastline basemap (Fig. 3.1). Thus mixed pixels including surrounding non-ice shelf terrain are excluded to avoid pixels with high topographic variation at the sub-

pixel scale and thus possible non-uniform melt within a single pixel (Johnson and others, 2020). Pixels which transitioned from ice shelf to ocean at some point during the time period due to ice shelf retreat or collapse were excluded, and we used year 2020 ice shelf outlines to determine ice shelf locations. One additional metric microwave studies in Antarctica have utilized to describe melt is a melt index defined by the product of area and number of melt days (e.g. Torinesi and others, 2003; Picard and others, 2007; Tedesco and others, 2007). In contrast, we report the number of melt days per year, henceforth referred to as annual melt days, to allow for direct comparison of melt duration between ice shelves regardless of their size.

3.2.1   Data

We use passive microwave data collected by satellite-based passive microwave instruments from 1979 onwards. With wide swath widths of 783–1700 km, these microwave sensors in sun-synchronous orbit allow for daily (from 1987 on) and near-daily (1978–1987) observations. This study uses 18 and 19 GHz measurements in the horizontal polarization, as there is a high contrast between wet and dry firn in this frequency and polarization (Mote and others, 1993). These measurements are coarse in space, at a resolution approaching, but coarser than, the $25{\times}25$ km^2 pixel size which the data is posted at. An example of this processing method, and how it can sometimes lead to cross-contamination for nearby surfaces, is given in Gloersen (1992).

All passive microwave data were downloaded from the National Snow and Ice Datacenter (NSIDC). The Scanning Multi-channel Microwave Radiometer (SMMR) instrument on the Nimbus-7 satellite provided the data for 1979–1987 at 18.0 GHz (Gloersen and Francis, 2003). Since the SMMR observations imaged Antarctic ice shelves approximately only once every 2 days, a linear interpolation was used to fill in all missing days, regardless of gap length. The most important gaps in the record were during the 1986/87 austral summer, which had three separate gaps of 4 days in length during December and January. The Special

49

Sensor Microwave Imager (SSM/I) and Special Sensor Microwave Imager/Sounder (SSMIS) instruments on board the Defense Meteorological Satellite Program satellites provided daily 19.35 GHz measurements from 1987 to 2020 (Meier and others, 2019). Due to a data gap of 40 days in December 1987 and January 1988 in the SSM/I record, the 1987/88 melt season was not considered in this study.

3.2.2   Melt detection

The emergence of meltwater in firn causes a drastic increase in the measured brightness temperature at 19 GHz, and this change is exploited to detect melt. The melt detection method used in this study follows Johnson and others (2020), which evaluated four different passive microwave melt detection algorithms across the Antarctic Peninsula by validating them against Sentinel-1 Synthetic Aperture Radar (SAR) melt observations. Sentinel-1 SAR has a resolution several orders of magnitude finer than the 25 km resolution of passive microwave observations. While the quantity of meltwater can vary greatly across ice shelves (e.g. Banwell and others, 2021), binary determinations of the presence of meltwater on ice shelves were found to be relatively uniform across the flat 25 km pixels. Overall, 98.9% of aggregated 1 km pixels in the SAR images shared the same melt or no melt determinations across individual 25 km passive microwave pixels on ice shelves (Johnson and others, 2020). This result was much lower on the pixels surrounding ice shelves. The presence of meltwater was found to be much less uniform directly adjacent to ice shelves where there is often high topographic variation.

Of the four passive microwave methods compared by Johnson and others (2020), two of them used brightness temperature thresholds based on deviations from the previous winter's temperatures, including a 30 K increase threshold (Mote and others, 1993; Zwally and Fiegles, 1994) and a 3 standard deviation threshold (Torinesi and others, 2003). A third method used a cross-polarization gradient ratio (Abdalati and Steffen, 1997). A final method used a statistical analysis of brightness temperature time series using a K-means clustering

algorithm. Here we use the latter method as it was found to be among the best correlated to SAR melt observations and was notably the least biased to overcount or undercount melt. During summer months, the SAR results agreed with this passive microwave method 88% of the time.

Comparison to 2 m air temperatures from Automated Weather Stations (AWS) was not carried out because there were few stations with continuous records on ice shelf surfaces which both experience notable melt and also experience the presence of meltwater uniformly at the 25 km resolution, aside from one station on the Larsen C Ice Shelf. In addition, liquid water can exist due to solar radiation in the surface when air temperatures are at or below 0°C (Tedesco, 2009) thereby complicating the validation technique.

This statistical method to detect melt used here applies a one dimensional K-means clustering algorithm to the annual brightness temperature time series to identify two clusters. If that annual set of passive microwave observations fits well into two clusters on the brightness temperature axis, or the two cluster centers are far enough apart (set here at 40 K) then the upper cluster is identified as melt. A good two-cluster fit is defined as the root-mean-square distance of brightness temperatures to the nearest cluster center in the two cluster case being 42% that of the one cluster case. Otherwise, or if the two cluster centers are too close together (within 20 K), then a threshold brightness temperature of 40 K above the lower cluster is used to detect melt instead (see Johnson and others, 2020 for further details).

An additional filter was applied in order to remove any erroneous melt detections in either obviously dry firn or in pixels which bear time series partially resembling sea ice. On rare occasions dry firn pixels in parts of the interior of the ice sheet could fool the detection algorithm if their seasonal brightness temperature swings were large enough. Some coastal passive microwave pixels also had occasional years in the record in which their time series would partially resemble that of sea ice, as characterized by a sudden transition to extremely low brightness temperature values in mid-late summer indicating the presence of open ocean water, even in cases where the pixel itself covered only land or ice shelf. These could be

51

the result of the formation of late melt season supraglacial lakes, which have been observed across Antarctica (Kingslake and others, 2017; Stokes and others, 2019; Arthur and others, 2020). However, not all instances of ice shelf pixels showing rapid transition to low summer brightness temperatures align with observed instances of standing water on ice shelves, and in particular some of the strongest instances of this phenomena occur on the ocean-side of the Brunt Ice Shelf in the mid 1990s. To resolve this, we removed data from any individual pixel during a year if that pixel reported 90 more melt days than its mean annual melt days, or if the melt threshold brightness temperature was found to be <160 K. On the primary ice shelves used in this study, these criteria only applied to 0.22% of the individual pixel annual melt day totals.

This approach is designed to detect the large jumps in brightness temperatures due to the emergence of liquid water, which are much larger than the differences between satellites or instruments. As such we do not apply a calibration to the measured brightness temperatures of different satellites. To validate this approach however, we tested the passive microwave calibration detailed in Nicolas and others (2017), and we found that in the 6 years in which there was overlap between the satellites detailed in their calibration, only 0.06% of the annual melt day totals for ice shelf pixels were altered.

3.3   Results

3.3.1   Spatial variability of melt

The spatial distribution of annual melt days averaged over the period 1979–2020 is shown in Figure 3.1. As expected, there is a general pattern of decreasing melt days with distance from the ocean, often corresponding to increasing elevation. The region names given in the map will be referred to from here on. Results are shown for the entire Antarctic ice sheet but further analyses are focused on the ice shelves. While there are large areas outside the ice shelves with considerable melt days, many of these have significant topographic variation, and therefore are not likely to have a uniform presence of meltwater at the resolution of

passive microwave. Annual melt days for individual ice shelf pixels vary between zero and 91 with an average of 24 days across all ice shelf pixels, excluding the Ross and the Ronne-Filchner ice shelves. On average, the Antarctic Peninsula ice shelves experience the most melt days, and only Antarctic Peninsula ice shelves and the Shackleton Ice Shelf have pixels which experience more than 60 mean annual melt days.

In Dronning Maud Land there is an overall west-to-east gradient of increasing annual melt days, consistent with Torinesi and others (2003), as well as regional climate models of surface melt (Van Wessem and others, 2018). Within the region, the westernmost Brunt and Riiser-Larsen ice shelves have the least melt days, with some pixels having less than one mean annual melt day, and the easternmost King Baudouin Ice Shelf has the most melt with up to 34 mean annual melt days. This gradient in melt days across the region likely indicates differing climate regimes across the region. For example, sea ice concentrations in western but not eastern Dronning Maud Land are strongly controlled by the Weddell Sea (Isaacs and others, 2021). In Amery and Wilkes Land the largest ice shelves, namely the Amery, West and Shackleton shelves, all have relatively high mean annual melt days with individual pixels exceeding 78 annual melt days. The ice shelves between the Moscow University and Cook ice shelves are smaller and have low melt day totals. Around the Cook Ice Shelf, there are many ice shelves which are too small for the coarse resolution of these passive microwave instruments to resolve.

On the western side of the continent, the Ross and Amundsen sea sectors of West Antarctica have few melt days. The most prominent ice shelf of the region, other than the Ross Ice Shelf, is the Getz Ice Shelf which has an area of 10000 km^2 observable by these passive microwave satellites and a mean of 5 annual melt days per pixel. Higher numbers of melt days are found in the Bellingshausen Sea sector. The Abbot is the largest ice shelf of the region with an investigated area of 15000 km^2 and an average of 21 annual melt days. In the Antarctic Peninsula, all of the ice shelves have especially high annual melt days, with the George VI, Larsen C, and Wilkins Ice Shelf all averaging more than 50. In particular, the

Wilkins Ice Shelf has the most melt days with individual pixels experiencing as many as 91 mean annual melt days. Pixels nearby to the Wilkins Ice Shelf reach up to 93 mean annual melt days. The annual melt day results we show on the Antarctic Peninsula are similar but slightly lower than those quantified over the same time period by Banwell and others (2021). Johnson and others (2020) demonstrate that on the Wilkins Ice shelf, the K-means statistical melt detection methods find a mean of 89 annual melt days over 1979/80-2018/19 whereas the method employed in Banwell and others (2021) finds 92 mean annual melt days.

3.3.2   Timing of melt

There are spatial patterns in the timing of melt across Antarctica, indicating earlier or later melt seasons in some regions. In order to quantify the timing of melt, we calculated the dates for the onset and midpoint of melt for each pixel. To quantify the onset of melt, we found the start date for the longest consecutive period of days of melt throughout the year with no gaps of 10 or more days. The midpoint of melt was the day of year on which half of all cumulative melt days had been reached, here referred to as melt day midpoint.

These results are shown in Figure 3.2. The earliest dates for the onset of melt on ice shelves occur in Amery and Wilkes Land and in the Antarctic Peninsula (Fig. 3.2a). The mean annual melt days of each pixel (Fig. 3.1) describe some of the variability in the timing of melt. Intuitively, pixels with more melt would usually be expected to have an earlier onset of melt. And indeed there is a significant negative correlation between pixel mean annual melt days and melt onset ($r = -0.94$, $p < 0.01$), equating more melt days with earlier onsets of the melt season. Throughout this paper, p-values are noted with either $p < 0.01$ or $p < 0.05$. To help track the spatial variability of timing of melt, Figure 3.2b shows the midpoint of melt for each pixel. There is also a low positive correlation between mean annual melt days and melt day midpoint day ($r = 0.29$, $p < 0.01$, Figs 3.1 and 3.2b), indicating that melt seasons often stretch further into the end of summer than the beginning for many regions with high melt, whereas low melt regions often experience melt seasons earlier in
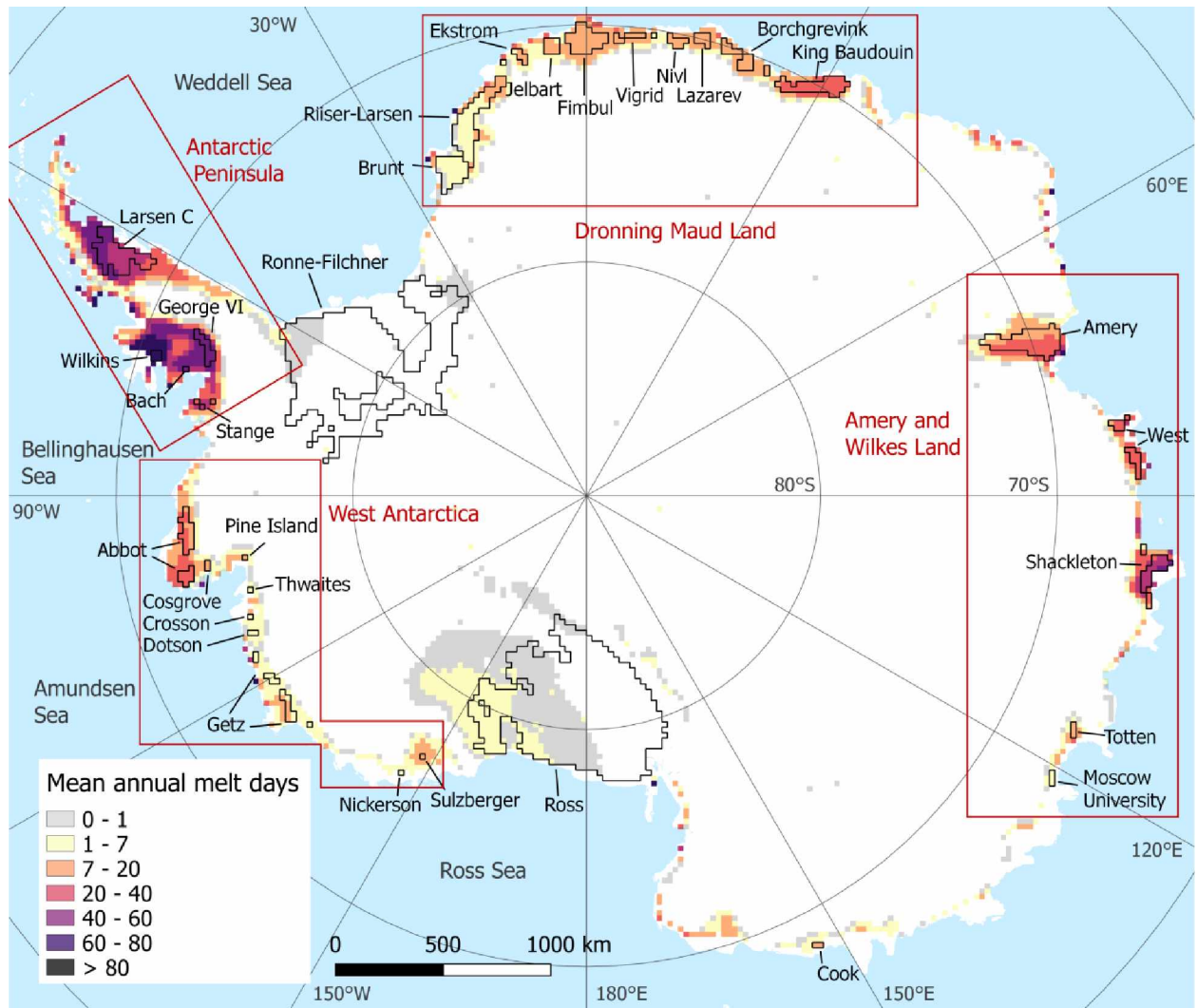
Figure 3.1: Mean annual melt days for each passive microwave pixel across Antarctica, 1979-2020, using the K-means melt identification algorithm. Black outlines show the extent of each ice shelf used in further analyses (based on 25×25 km pixels that are entirely classified as ice shelf).
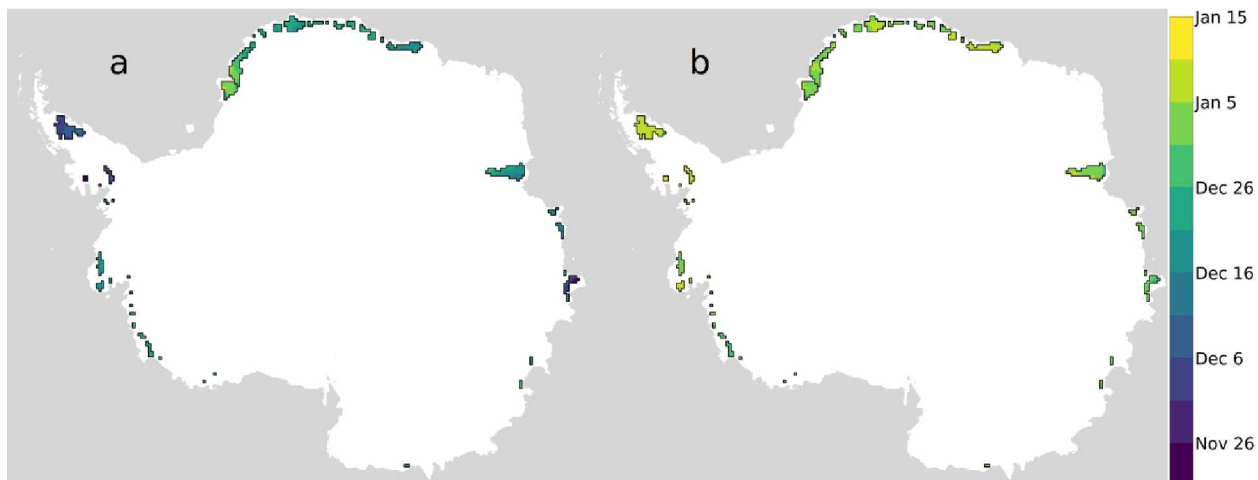
Figure 3.2: (a) Mean day of onset of seasonal melt. (b) Day of year when half of the total number of annual melt days has been reached (here referred to as melt day midpoint). Results are averaged over 1979 - 2020

the summer, closer to the times of maximum possible solar radiation. These patterns are perhaps best exemplified in the Antarctic Peninsula, where there are long melt seasons and late midpoints of melt. There are two ice shelves however which are notable in that they defy this trend. The Shackleton and West ice shelves in Wilkes Land have high melt days and some of the earliest dates for the onset of melt, but they also have some of the earliest melt day midpoints. Therefore, these two ice shelves in Wilkes Land have an unusually early melt season compared to elsewhere across Antarctica.

The majority of melt days occurs during the summer, but several winter melt events have been documented, mostly on the Antarctic Peninsula. Figure 3.3 shows the mean annual melt days for each pixel during a winter period of April 15 to October 15 on the Antarctic Peninsula. There is large interannual variability in winter melt because a pixel might only experience winter melt events during a few years in the melt record. There is a correlation $(r = 0.60, p < 0.01)$ between mean winter melt days and total mean melt days for each pixel as only pixels with relatively high amounts of melt ever see melt during the winter. However, further variability in winter melt days is likely related to specific local climatic processes. For example, Larsen C winter melt events have been shown to be driven by foehn winds (Kuipers Munneke and others, 2018; Datta and others, 2019) and the winter melt observed
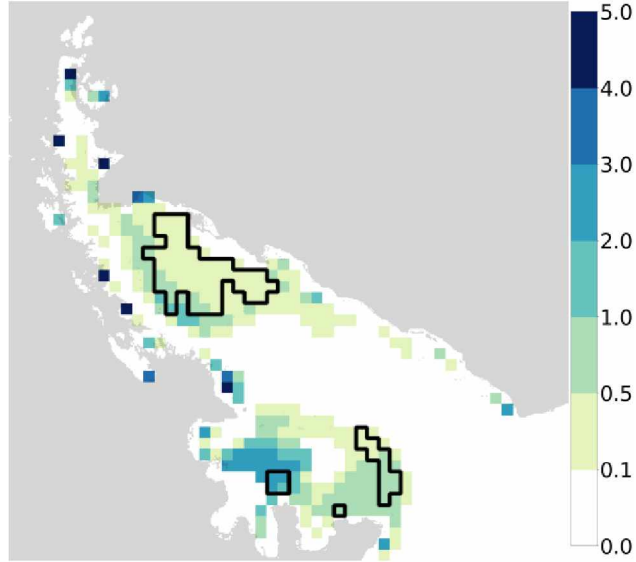
Figure 3.3: Mean number of annual winter melt days for each pixel of the Antarctic Peninsula, over 1979-2019. The winter period here refers to 15 April - 15 October.

here occurs more frequently in the inland pixels where these foehn winds reach the shelf. These events range from a couple days up to 10 days on the Larsen C Ice Shelf (Kuipers Munneke and others, 2018). We find winter melt events on the Larsen C Ice Shelf with durations of up to 11 days. On the western side of the peninsula, winter melt days are most common to the west of the Wilkins ice shelf in regions closest to the Bellingshausen Sea. Temporally, there are almost no statistically significant linear trends in the number of days of winter melt over the four decade record ($p < 0.05$). This agrees with the lack of linear trends in winter melt days noted by Kuipers Munneke and others (2018) over 2000–2016 based on scatterometer observations.

3.3.3 Trends in annual melt days

Mean annual melt days over the 41-year study period are plotted for each investigated ice shelf in Figure 3.4, excluding the Ross and Ronne-Filchner ice shelves. Melt days averaged over all pixels on each ice shelf are shown. Interannual variability tends to be high, especially for many ice shelves with low annual melt day averages. For example, in most years, Thwaites has only a few days of melt per year, but there are 3 years in the record with more than 15 days of melt, reaching 30 days in 2012/13. The distribution of annual melt days detected by passive microwave instruments has been noted to appear gaussian for pixels with high melt days, and exponential for pixels with fewer melt days (Picard and others, 2007). High melt years are usually regionally coherent, and are further explored in Section 3.4.1.

None of the ice shelves in Figure 3.4 show a significant ($p < 0.05$) linear trend in annual melt days over the time period. Subsets of the time period have been demonstrated to show trends however, for example, Bothale and others, 2015 find significant negative trends over 2001–2014 using scatterometer data on some ice shelves, mostly clustered around the Antarctic Peninsula, with the Larsen C Ice Shelf seeing –3.3 days of melt per year. We do not find these trends to be significant in our data. Picard and others (2007) document negative trends in melt across the Antarctic Peninsula over 1995/96–2005/06. Over this time period, we find many individual pixels on the Larsen C Ice Shelf with significant negative melt day trends, with an average of –3.5 annual melt days per year ($p < 0.05$). As previously noted, the Antarctic Peninsula is observed having a negative annual temperature trend over 2000–2014 in the weather station temperature record (Turner and others, 2016).

Over the entire time period, if we consider the annual melt day time series of individual pixels instead of entire ice shelves, there are still few statistically significant linear trends over the time period. Across these ice shelves, only 4.1% of the individual passive microwave pixels have significant ($p < 0.05$) trends, and the linear trends that meet this threshold on ice shelves have a mean and standard deviation of -0.43 ± 0.12 annual melt days per year. These pixels are mostly spread across the Larsen C, Fimbul, Amery and Shackleton
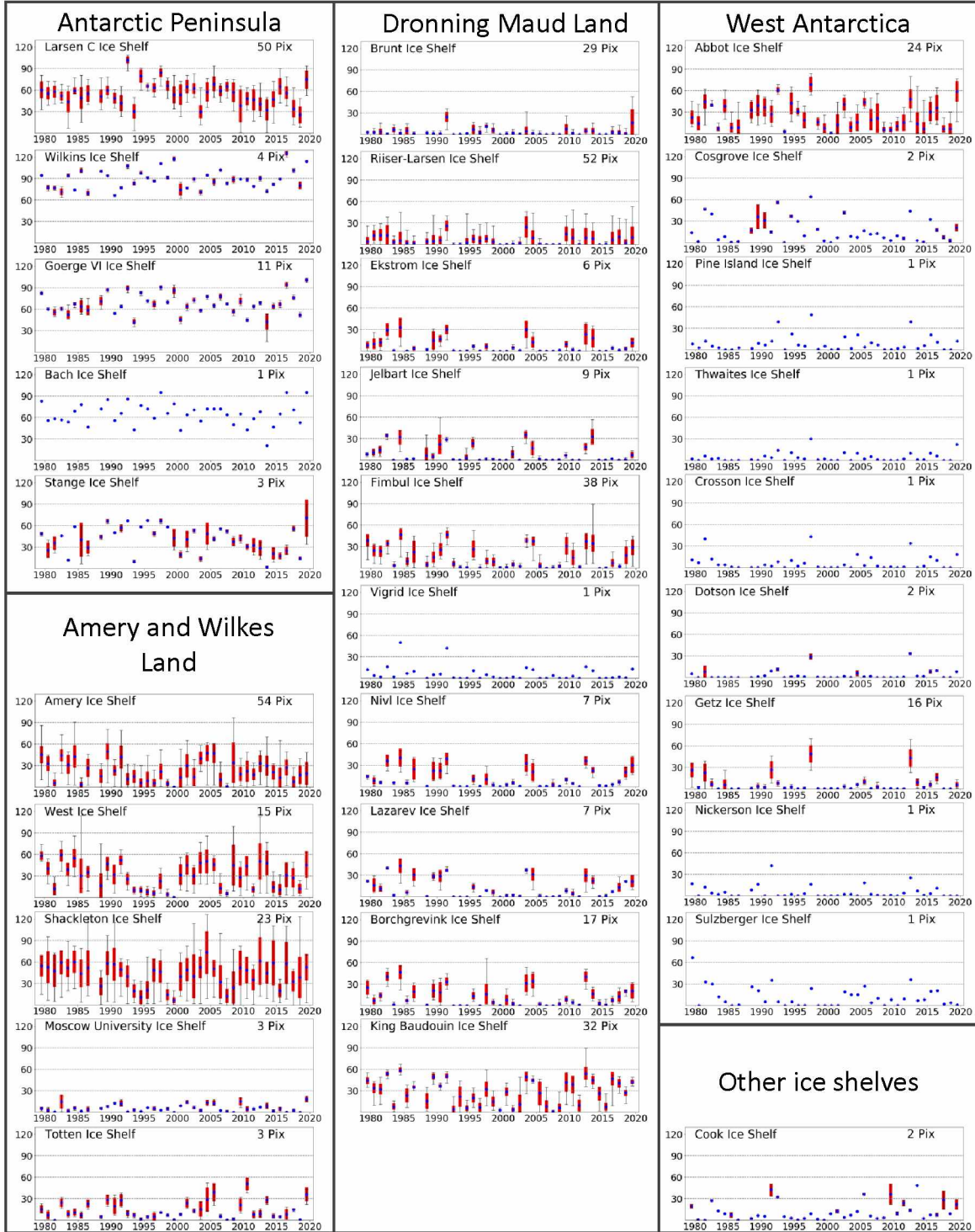
Figure 3.4: Annual melt days for all 30 investigated Antarctic ice shelves from 1979/80 to 2019/20. Figure shows annual melt days averaged across all pixels of each ice shelf (as defined in Figure 3.1), standard deviation (red bars) of pixels within that ice shelf, and range. Standard deviation and range markers are absent if the ice shelf only has one pixel or if all pixels have the same amount of melt. The Ross and Ronne-Filchner ice shelves are shown separately due to their much smaller number of melt days (Figure 3.5).

59
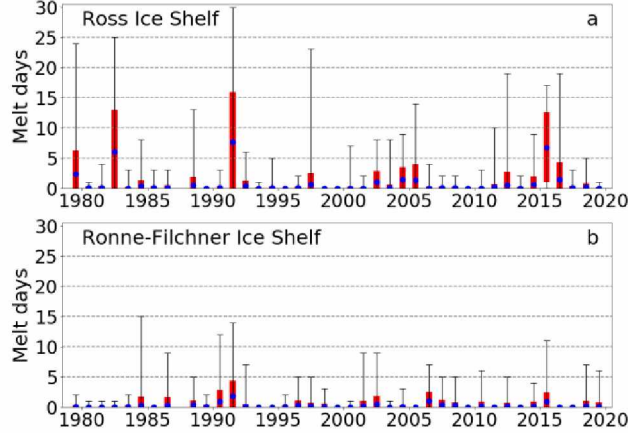
Figure 3.5: Annual melt days averaged across all pixels on Ronne-Filchner and Ross ice shelves. Standard deviations given by red bars. The Ross Ice Shelf covers 647 pixels and the Ronne-Filchner covers 549 pixels.

ice shelves. The significant trends range from –0.71 to –0.11 annual melt days per year.

The largest ice shelves, the Ronne-Filchner and the Ross, experienced very little melt. Their melt day time series is therefore shown separately in Figure 3.5. Melt is not spatially homogeneous across ice shelves this large, and even during the highest melt years, large swaths of the surface experienced no melt. Much of the surface of the Ronne-Filchner Ice Shelf experiences no melt in this record. On these ice shelves, melt primarily occurs on the northwestern section of the Ronne-Filchner Ice Shelf and the northeastern quadrant of the Ross Ice Shelf (Fig. 3.1). The vast majority of melt days on the Ross Ice Shelf are contained in just a few melt events, especially those during 1991/92 and 2015/16 (Fig. 3.5a). The median number of spatially averaged annual melt days across the Ross Ice Shelf is 0.08, yet the 1991/92 melt season averaged 7.6 melt days, and pixels in the northeast showed melt for as many as 30 days. Further analysis of this melt event and its impacts are given in Section 3.4.3.

3.3.4   Spatial correlations

To investigate the spatial coherence of melt days across Antarctica, we correlate the mean annual melt day time series for each possible ice shelf pair. This comparison only correlates

total annual melt days, with no regard to the timing of that melt throughout the year (further explored in Section 3.3.3). All of the significant correlations ($p < 0.05$) are shown in Figure 3.6, which account for 48% of all ice shelf pairs. The highest annual melt day correlations are found between ice shelves in the same region, which is to be expected. The greatest intra-region coherence was in Dronning Maud Land with correlation coefficients reaching up to 0.96. On the Antarctic Peninsula, the correlations between ice shelves on the western side of the mountainous spine is high (with r values as up to 0.93), but the correlations from the Larsen C on the eastern side to the other Antarctic Peninsula ice shelves are lower (r values of 0.40–0.65). Overall, correlation coefficients for ice shelves within each of the major regions in Figure 3.1 range from 0.31 to 0.96.

Perhaps more important to the study of climatic drivers are the correlations between regions. These correlations indicate that many ice shelves across the continent had similar very high or low melt day totals during the same years. Dronning Maud Land has relatively high correlations with Amery and Wilkes Land (with r values up to 0.71, averaging 2800 km apart) and West Antarctic ice shelves on the Ross Sea side of West Antarctica (with r values up to 0.55, 3000 km apart). The Ross Sea sector of West Antarctica also shows some correlations to Amery and Wilkes Land melt (r values up to 0.47), despite the fact that these regions are separated by an average distance of 4000 km. The Antarctic Peninsula has fewer melt day correlations with other regions. It has significant correlations with West Antarctica (r values up to 0.65) and also strikingly negative correlations with several Dronning Maud Land ice shelves across the Weddell Sea (with r values between –0.33 and –0.47) on the opposite side of the Weddell Gyre.

The spatial correlations of melt between ice shelves shown above demonstrate coherent temporal variations in melt days between many regions across the continent. In order to provide more detail so these results can be better compared to underlying climatic drivers, we compared the melt day time series of each individual pixel pair. We performed a Principal Component Analysis (PCA) to determine the primary modes of variability and visualize
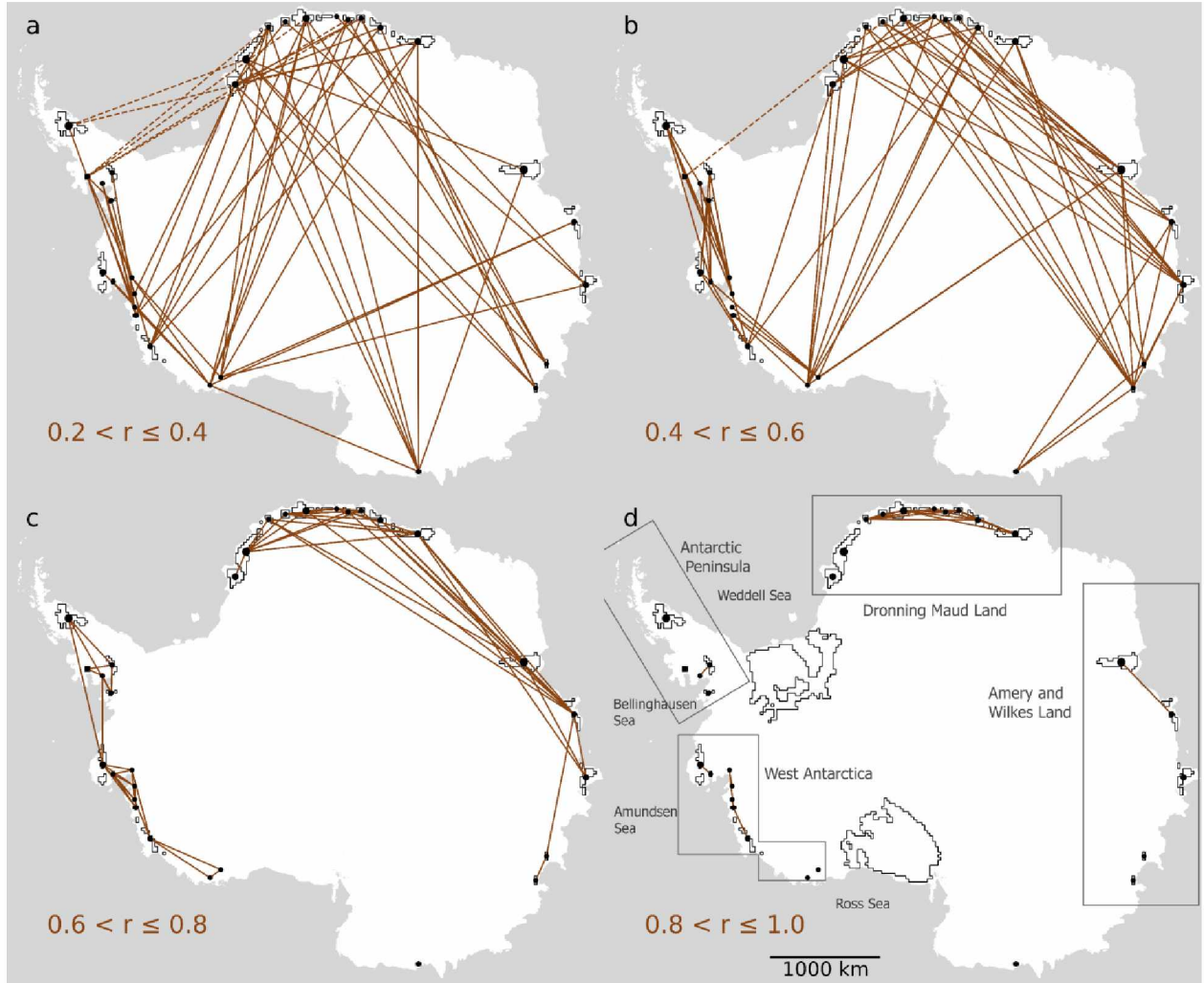
Figure 3.6: Correlations (r) in annual melt days between ice shelves from 1979-2020 ($p <$ 0.05). Ice shelves with statistically significant correlations are connected by lines, and results shown for four ranges of correlation coefficients. Positive correlations are given with solid lines, and negative correlations with dotted lines.

their spatial characteristics (Fig. 3.7) by using an eigen decomposition on the covariances between the annual melt day time series of each ice shelf pixel. The Ronne-Filchner and Ross ice shelves were excluded from this calculation because otherwise, due to their size, their faint modes of variability would dominate the PCA. These modes of variability imply a relationship of the climate drivers across the continent for that mode.

The first principal eigenvector (Fig. 3.7a) describes 41% of the variability in the annual melt day dataset, and has the strongest associations to Dronning Maud Land and Amery and Wilkes Land ice shelves, with a smaller negative connection to the Antarctic Peninsula. The second Principal Component (Fig. 3.7b) describes 20% of the variability and has strong associations to Antarctic Peninsula and Bellingshausen Sea sector ice shelves, but only a weak relationship to melt elsewhere on the continent. While the coefficients are negative in these regions instead of positive, it is the direction and not necessarily sign which shows the pattern of variability. The second mode implies that the strongest drivers of melt on the Antarctic Peninsula and West Antarctica have less impact on melt across the rest of Antarctica. These first two modes bear some visual resemblance to the East-West asymmetry of near-surface annual mean air temperature variability modes observed across Antarctica over 1958–2012 (Jun and others, 2020), although the temperature modes are strongly related to winter air temperature variability while surface melt here is primarily a summer phenomena. The third Principal Component is primarily dominated by the difference between melt in Amery and Wilkes Land to melt in Dronning Maud Land and accounts for 8% of the variability in the data. No other modes account for more than 5% of the variability.

3.4   Discussion

3.4.1   Analysis of high melt years

Many of the ice shelves around Antarctica have few spatially averaged melt days per year over 1979/80–2019/20, yet even in regions with very low melt there are notably abnormal years with remarkably high deviations from the mean. For example, the Getz Ice Shelf in the
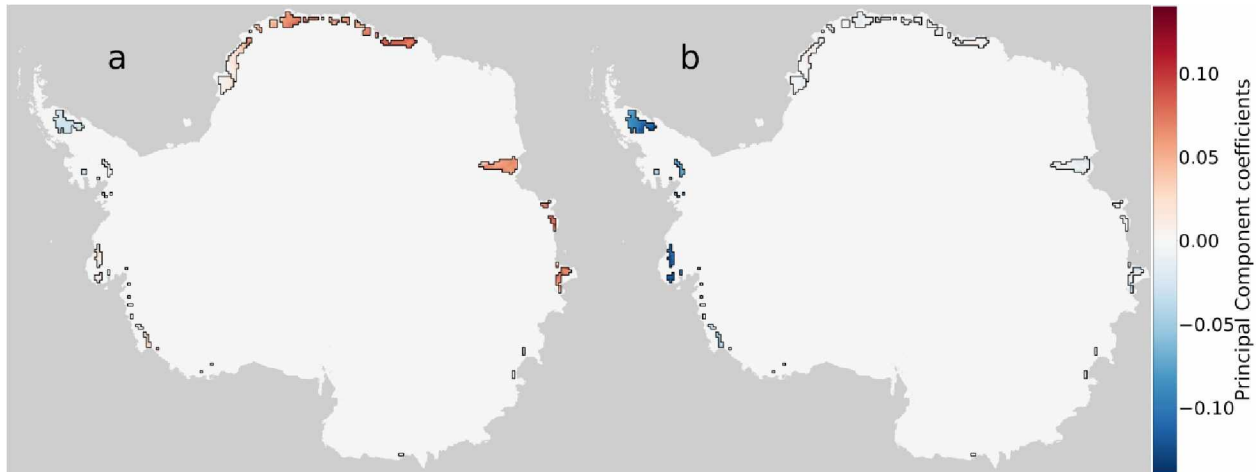
Figure 3.7: First two Principal Components, with coefficients projected back onto their corresponding passive microwave pixels. (a) First Principal Component, which describes 41% of the variance. (b) Second Principal Component, which describes 20% of the variance.

Amundsen Sea sector of West Antarctica (see Fig. 3.4 for the full melt record) experienced an average of 5 annual melt days. However, in each of the years of 1991/92, 1997/98 and 2012/13, there were more than 20 melt days. Similar ice shelves nearby, as well as many in Dronning Maud Land in 1991/92 and 2012/13, had very high melt days in those years as well. The climate characteristics of these remarkable years provide insight into the drivers of variability of melt days across Antarctica.

In this section, we identify years of high melt and categorize them. We classify a high melt year as a year in which three or more ice shelves have annual melt days of at least two standard deviations above their mean. There are eight melt years in the dataset which meet this criteria: 1982/83, 1984/85, 1991/92, 1992/93, 1997/98, 2003/04, 2012/13 and 2019/20. The years we identify here loosely fit into two categories: those which have a very high number of melt days in Dronning Maud Land (1982/83, 1984/85, 1991/92, 2003/04 and 2012/13), and those which have very high melt days on the Antarctic Peninsula and Bellingshausen Sea sector of West Antarctica (1992/93, 1997/98, 2019/20). The melt day anomalies relative to the 1979/80–2019/20 melt day average for each of these years are shown in Figure 8.

In the years with high numbers of melt days on Dronning Maud Land ice shelves, the

ice shelves of Amery and Wilkes Land generally experienced similar anomalies but West Antarctica had variable melt days. The westernmost ice shelves of Dronning Maud Land, the Brunt and Riiser-Larsen, also did not have noticeably high or low melt during these years. The year 1991/92 stands out as it saw a remarkably high number of melt days on the Amundsen and Ross Sea side of West Antarctica and also on the Ross Ice Shelf itself. One particularly notable pattern during these years is the contrast to the Antarctic Peninsula. During the five high melt years in Dronning Maud Land, the Antarctic Peninsula generally had negative melt day anomalies.

The pronounced spatial differences of melt days between Dronning Maud Land and the Antarctic Peninsula during these years are consistent with the negative correlations in annual melt days between these two regions (Figs 3.6a, b). Seven significant ($p < 0.05$) negative correlations were identified between ice shelf pairs in the Antarctic Peninsula and Dronning Maud Land, with r values ranging from -0.33 to -0.47. However, if these five particular years are removed from the record then all of the negative melt day correlations lose their statistical significance.

The years of 1992/93, 1997/98 and 2019/20 are marked by a notably high number of melt days on the Antarctic Peninsula and the Bellingshausen Sea sector of West Antarctica. Banwell and others (2021) note 1992/93 as having the highest cumulative melt on the Antarctic Peninsula. There are moderate to negative melt anomalies in Dronning Maud Land and Amery and Wilkes Land during these years. As shown in Figure 3.6, the annual melt days on the Antarctic Peninsula and Bellingshausen Sea side of the West Antarctica are not particularly correlated to melt days in other regions of Antarctica. Likewise in each of the years of 1992/93, 1997/98 and 2019/20, there are few distinct spatial patterns of melt days across the rest of the continent in each of those years.

The spatial patterns of melt days during these eight high melt years match closely with the direction of the first two Principal Components of melt day variability (Fig. 3.7). The spatial patterns of melt during years with high melt days in Dronning Maud Land are
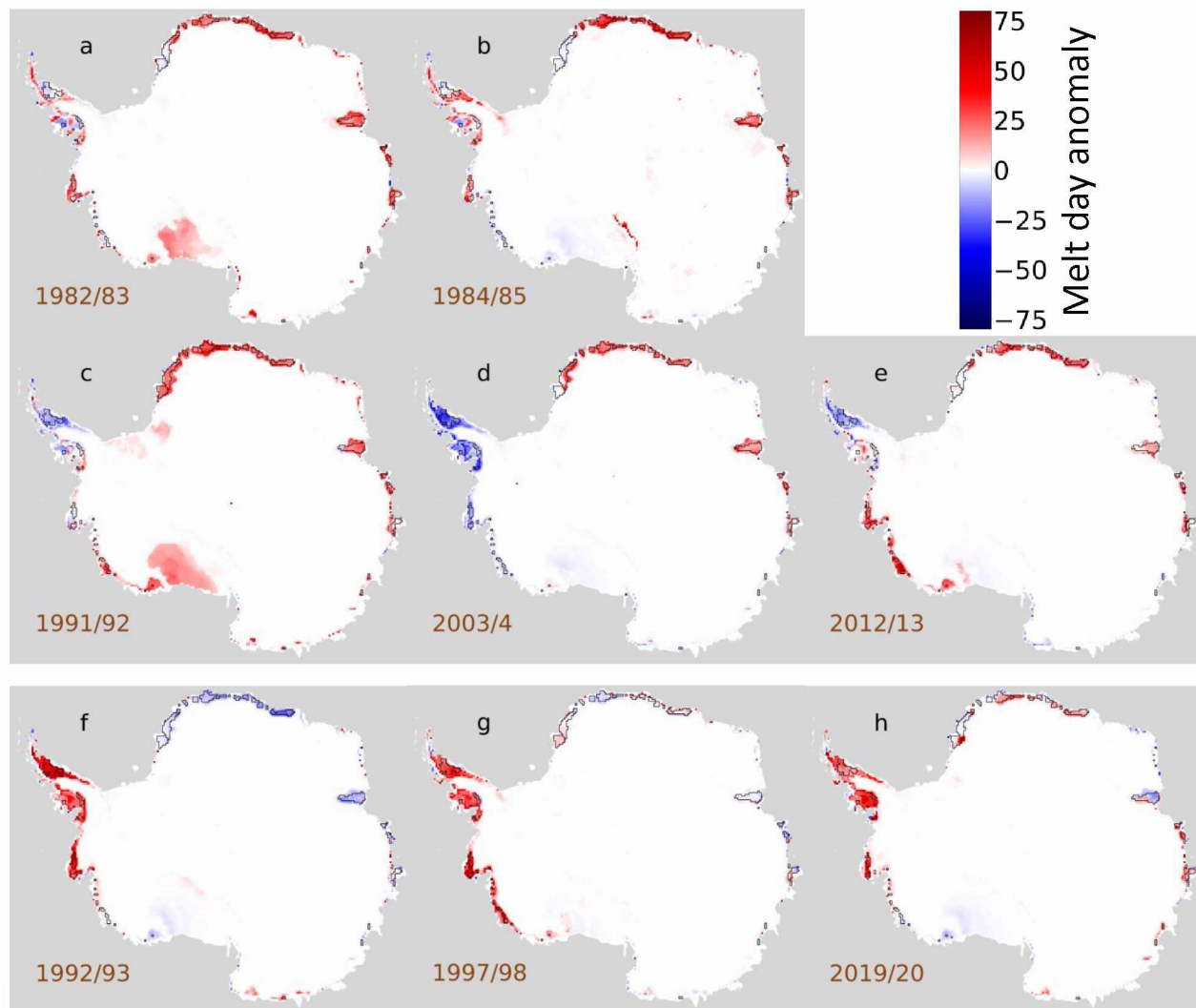
Figure 3.8: Melt day anomaly relative to the 1979-2020 mean for each pixel for selected high melt years. Panels a-e show years with high melt day anomalies in Drowning Maud Land while panels f-h show years with high numbers of melt days on the Antarctic peninsula.

similar to the first Principal Component of melt variability and the spatial patterns of melt in years with high melt on the Antarctic Peninsula show similarity to the second Principal Component, which is also dominated by the variability of the Antarctic Peninsula.

The years presented here mark the years with especially high melt along the ice shelves surrounding Antarctica. As such, a few years with notably high regional melt events or melt extents stretching further into the interior of the continent were not identified by this metric. In particular, we note 2005/06 which is documented as having especially high melt in the Amery, Wilkes Land and Ross regions of Antarctica (Tedesco, 2009), but not elsewhere. The 2015/16 melt season brought melt to a large extent of the Ross Ice Shelf and West Antarctica over a 1–2 week period in mid January, related to strong El Niño (Nicolas and others, 2017). During that year, there was some increased melt on the Abbot and Larsen C ice shelves, and decreased melt across Dronning Maud Land and Amery and Wilkes Land.

3.4.2 Climate correlations

To investigate the climatic context of the spatial variations in melt days across Antarctic ice shelves, we correlate the spatially averaged ice shelf annual melt day time series with ENSO as measured by the Multivariate ENSO Index (MEI) and SAM ($p < 0.05$). MEI and SAM values were obtained from the NOAA Physical Sciences Laboratory and NOAA Climate Prediction Center, respectively. Following previous literature (Torinesi and others, 2003; Tedesco, 2009), we compare melt days to the mean October through January climate index values as they were found to have some of the strongest correlations with melt detection results. All significant correlations are shown in Figure 3.9. Results show that many West Antarctica ice shelves, especially along the Amundsen Sea, have a moderate positive correlation (r values 0.32–0.49) with the mean October through January MEI. More substantial however in terms of r values and number of significant correlations are the correlations with SAM. In Dronning Maud Land, Amery and Wilkes Land, and West Antarctica, there are negative correlations (r values from –0.33 to –0.60) with the mean October through January
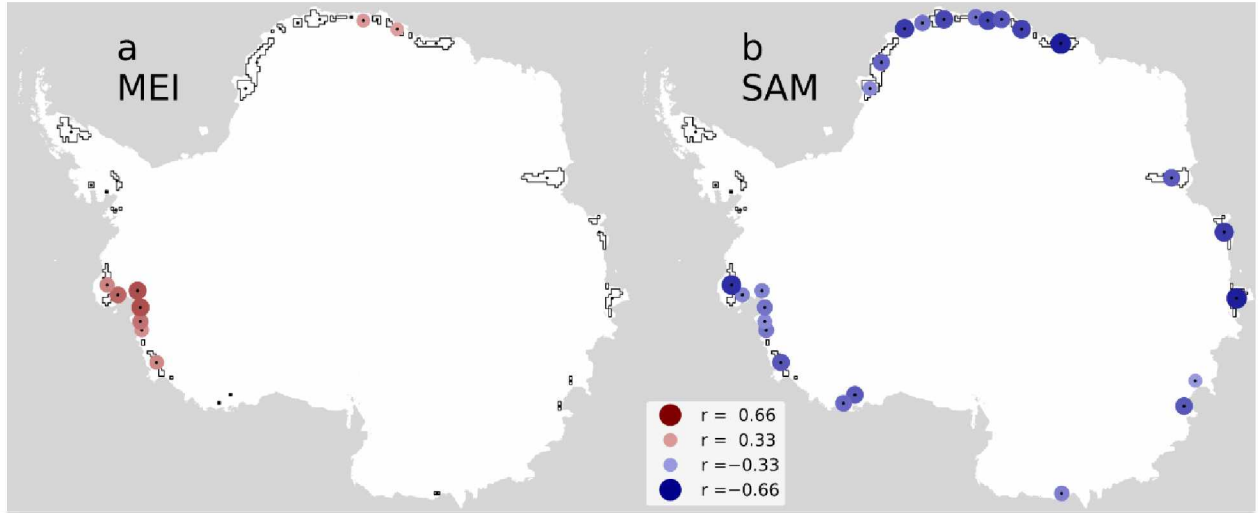
Figure 3.9: Statistically significant correlation coefficients (r) between ice shelf annual melt days and mean October through January values of (a) the Multivariate ENSO Index and (b) the Southern Annular Mode. The radius and color of the circle scale with the absolute value of r. The maximum absolute r value is 0.60.

SAM. The negative correlations with SAM are consistent with previous work (Torinesi and others, 2003; Tedesco, 2009), although their work found higher absolute correlations using melt area×day index values rather than melt days used here and without the benefit of the most recent decade of data. Picard and others (2007) also noted trends of decreasing melt days on the Antarctic Peninsula and increasing melt elsewhere coinciding with decreasing SAM.

Several lines of evidence suggest the importance of the role SAM plays in the variability of melt on Antarctic ice shelves. Many of the ice shelves in Figure 3.9 with the strongest negative correlation of annual melt days to summertime SAM values are also the ice shelves with especially high melt during the large melt years of 1982/83, 1984/85, 1991/92, 2003/04 and 2012/13 (Fig. 3.8). These ice shelves, especially the ones in Dronning Maud Land and Amery and Wilkes Land, align with the first Principal Component of melt day variability in the PCA analysis (Fig. 3.7a). Furthermore, there is a direct relationship between SAM and the first PCA eigenvector. We tested the correlation of each individual passive microwave pixel on ice shelves to the mean October through January SAM values, and found that these

correlations are also significantly correlated to the first Principal Component coefficients with an r value of -0.78 ($p < 0.01$). This demonstrates an inverse relationship in the southward migration of Southern Westerly Winds with melt days in Dronning Maud Land, such that there is more melt when these winds are further away from the continent. A similar but weaker connection is also found between the second Principal Component and MEI ($r = 0.12$, $p < 0.01$). Thus spring and summertime SAM values provide a major contribution to the primary mode of variability in the melt day record.

Firn core oxygen isotope analysis has shown that SAM was the dominant mode of climate variability in coastal Dronning Maud Land at the decadal scale over the past century (Naik and others, 2010). SAM provides an avenue to explain the physical mechanisms which could cause variability of Antarctic melt. The northward-migration of the Southern Westerly Winds associated with a negative summertime SAM phase is known to be related to increased warming in Dronning Maud Land and Amery and Wilkes Land as well as cooling in the Antarctic Peninsula (Marshall, 2007). We observe the melt dataset presented here to have a stronger relationship to SAM than to ENSO, although both are known to interact with Antarctic climate, and teleconnections to ENSO are strongest when SAM is weak or opposite (Fogt and others, 2011).

3.4.3   Detecting interannual changes to firn structure

For surfaces that normally have low numbers of melt days, we have frequently noticed changes to the microwave emission intensity of dry firn following summers with abnormally high melt. Figure 3.10 shows one such example on the Getz Ice Shelf. Over the entire 40-year time period, this pixel has a mean of 10 melt days per year, yet in the 2012/13 summer there was an unusually large melt event with a total of 45 melt days. Interestingly, after the melt had ended, the brightness temperature of the dry firn was significantly lower than it was before the melt season. This can be used to detect firn changes in some cases.

To quantify this effect, we define a value here called the Firn Seasonal Brightness Temper-
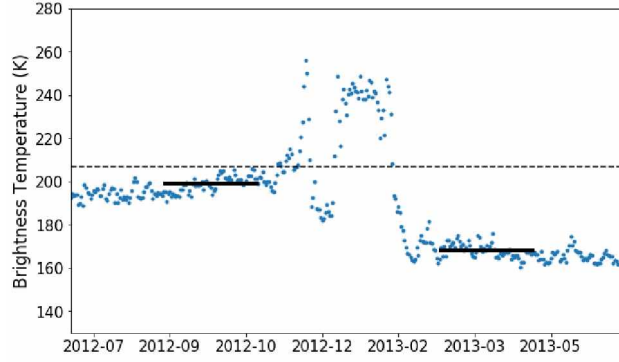
Figure 3.10: Brightness temperature observations of single pixel on Getz Ice Shelf over the course of the austral summer 2012/13. Black lines indicate the mean value over the September-October and March-April periods used to detect changes in firn structure. Dashed line shows the melt detection threshold for this time series.

ature Difference, Δ_{BT} , which is the mean September and October brightness temperature subtracted from the mean of the following March and April. This value is a measure of the change in brightness temperature caused by surface processes during the summer season. We observe that regions without melt, which is nearly the entire ice sheet except the periphery, on average have positive Δ_{BT} values indicating higher fall than spring brightness temperatures. We interpret this to be the result of the diffusion of seasonal heating into the snowpack. For example, the top several meters of a snowpack in dry firn in Antarctica have been observed to have higher temperatures in March–April than in September–October (e.g. Macelloni and others, 2007). Ice shelves and areas near the edge of the ice sheet which do experience melt however have negative Δ_{BT} . The decrease in Δ_{BT} in regions with melt is not necessarily linear with respect to the number of melt days. Regions which have more than 30 days of melt, such as the Antarctic Peninsula, do not have as large of a Δ_{BT} anomaly during very high melt years compared to areas which generally have much fewer melt days.

Several important anomalies of Δ_{BT} are given in Figure 3.11. The maps from 1991/92 and 1997/98 give examples of the Δ_{BT} anomaly during the two types of high melt years detailed in Section 3.4.1. The Ross Ice Shelf had large negative anomalies in 1991/92 and 2015/16, which are the years it experienced by far the most spatially cumulative melt days (Fig. 3.5a). On other parts of the continent, Dronning Maud Land had significant negative

70
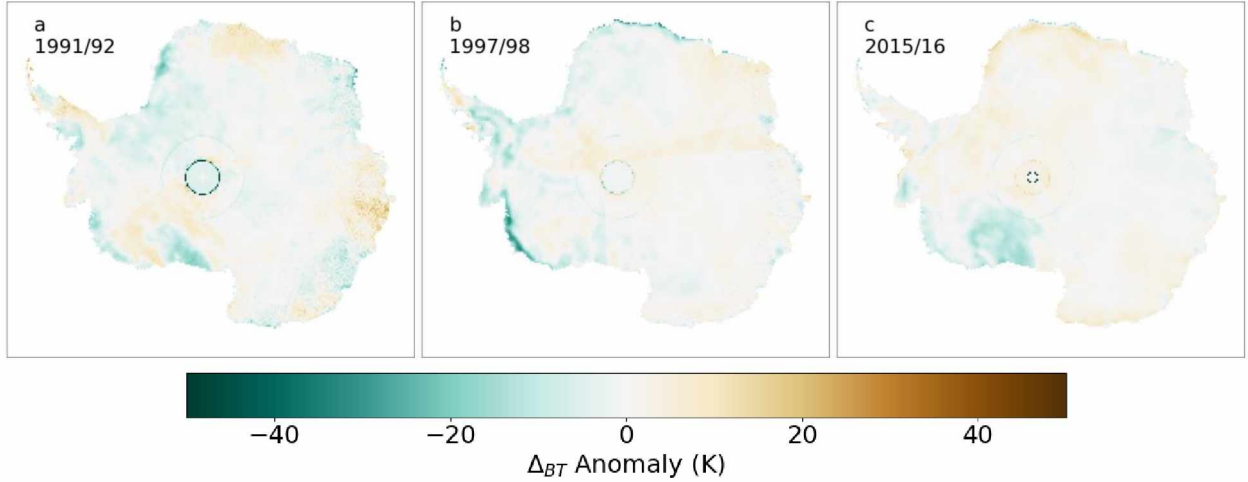
Figure 3.11: Firn Seasonal Brightness Temperature Difference (Δ_{BT}) anomalies for select years.

Δ_{BT} anomalies during 2003/04 and 2012/13 and West Antarctica had significant negative Δ_{BT} anomalies during 1997/98 and 2012/13. Each of these are years of especially high melt in those regions.

These decreases in firn brightness temperatures could be explained by increased grain growth and ice lens development due to melt. The effects of liquid water in a snowpack provide a physical basis for such a decrease in brightness temperature. Liquid water in firn promotes grain growth and can refreeze into ice lenses in the firn column (Benson, 1962). At 19 GHz, the upwelling radiation originates from the top several meters of a dry firn column, decreasing exponentially with depth (Chang and others, 1976). Ice lenses and larger snow grains increase microwave scattering in snow, thereby reducing the intensity of microwave emissions which can escape the firn after the melt concludes (Abdalati and Steffen, 1998). Microwave radar analysis of the 1991/92 Ross Ice Shelf event has indicated the formation an ice layer (Fahnestock and Bamber, 2001), and firn cores on the Ross Ice Shelf taken in 1999–2001 mostly only had ice lenses associated with the 1991/92 melt season present in the core (Das and Alley, 2005), as well as a few lenses from the 1992/93 melt season. While we do not detect much melt overall melt on the Ross Ice Shelf during 1992/93 (Fig. 3.5a), there were some small melt events on the interior of the ice shelf (Fig. 3.8f) and there

are coinciding negative Δ_{BT} anomalies in that region. The depressed dry firn brightness temperatures continued for more than a year in some cases. Burial rates at locations on the Ross Ice Shelf have been observed as being between 30 and 65 cm per year (Knuth and others, 2010), so ice lenses could take a couple years to be buried below the passive microwave observation depth.

To further aid this interpretation of abnormal brightness temperature decreases being related to melt-driven increases in grain growth and ice lens development in a firn surface, we have considered the scatterometer records of ASCAT over the 2015/16 melt event covering the Ross Ice Shelf. ASCAT Enhanced Resolution Images were obtained from the Scatterometer Climate Record Pathfinder at BYU. The January 2016 melt event has been well documented (Nicolas and others, 2017) and it appears clearly in the passive microwave melt record here (Fig. 3.12b). We compared two ASCAT images from directly before and after this melt event on the Ross Ice Shelf, and we observe a distinct increase in the ASCAT backscatter following this event, in the same spatial pattern as melt (Fig. 3.12a). Melt has been noted to create extremely strong microwave reflectors in a snowpack in the percolation zone of Greenland due to large snow grains and ice lenses (Rignot and others, 1993). The increase in backscatter on the Ross Ice Shelf over the 2015/16 austral summer is a clear indication of new scatters present in the firn column, and the spatial similarity to the melt event implicates the melt as the source of the scatterers. The melt features of ice lenses and increased grain sizes have already been noted to cause a decrease in the measured passive microwave brightness temperatures, and we observe the passive microwave Δ_{BT} decrease from this event on the Ross Ice Shelf (Fig. 3.12c) follows the same pattern as the melt and backscatter increases.

The annual Δ_{BT} anomalies could help to identify regions in which melt-driven changes occurred in these firn surfaces. Ice lens formation can increase runoff in a snowpack (Machguth and others, 2016), and the grain growth and ice lens development identified in this section can affect other microwave-band observations (Fig. 3.12a). These changes might pose prob-
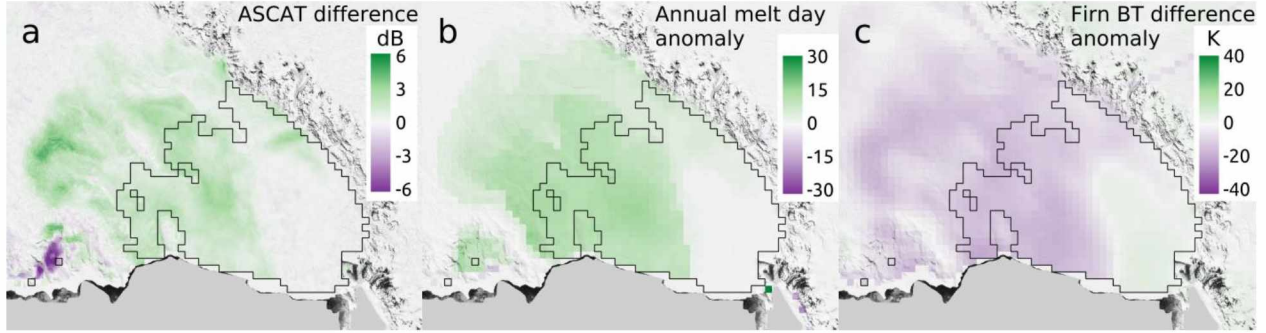
Figure 3.12: Observations of the Ross ice shelf from the 2015/16 melt season. (a) ASCAT backscatter (σ^0) difference between 31 January 2016 and 1 January 2016. (b) Anomaly of annual melt day for 2015/16. (c) Anomaly of Firn Seasonal Brightness Temperature Difference (Δ_{BT}) anomaly for 2015/16. Background map is Modis Mosaic (Haran and others, 2014), with the passive microwave ice shelf mask outline shown.

lems for radar altimetry. For example, the radar altimetry-derived thinning rates on the Ross Ice Shelf observed by Paolo and others (2015) over 1994 –1998 (their Fig. 3.2) have a spatial variability of up to 5 m a^{-1} across the Ross Ice Shelf with a pattern which closely aligns with the surface Δ_{BT} anomaly pattern from the 1991/92 melt season, despite thinning being attributed to basal melt. Ice lens development, detectable by changes in firn brightness temperature shown here, can contribute to changes in radar penetration depth over time, possibly leading to errors in analysis of active microwave radar time series.

3.5   Conclusions

Passive microwave datasets allow for quantification of melt days for the past four decades, providing a valuable dataset to augment other cryospheric observations. These results can be used to study climate across the continent or understand the recent history of a single ice shelf. Spatially the highest mean annual melt days occurred on the Wilkins Ice Shelf in the Antarctic Peninsula and the Shackleton Ice Shelf in Amery and Wilkes Land, with the Wilkins having the most at 89 mean annual melt days. In Dronning Maud Land, melt days show a positive eastward gradient, and West Antarctica also has similar spatial trend with generally increasing melt days eastward toward the Antarctic Peninsula.

Results show a striking lack of linear trends in the number of annual melt days over

73

1979–2020, despite the known positive trends in near-surface air temperatures across parts of the continent based on weather station records (Turner and others, 2020) and climate models (Smith and Polvani, 2017), or known negative trends in specific regions over specific time periods (Turner and others, 2016). Given the negative correlation of spring and summer SAM with melt days in Dronning Maud Land, Amery and Wilkes Land, and the Ross Sea sector of West Antarctica, the positive trend in SAM over this time period provides one mechanism which has been increasingly reducing annual melt days in these regions. Some of the divergences between the documented temperature trends and the results presented here may be explained by the fact that melt predominantly occurs during the summer. Regional and continent-wide trends in near-surface Antarctic temperatures have been shown to be weaker and less significant during the austral summer compared to other seasons, with spring having the highest trends (Nicolas and Bromwich, 2014).

Years with the highest melt can be classified into two groups, and these groups also match the primary modes of spatial and annual variability in the melt day dataset. Years with high numbers of melt days in Dronning Maud Land tend to have high melt days in Amery and Wilkes Land and in the Ross Sea sector of West Antarctica, as well as lower melt days on the Antarctic Peninsula. There are numerous correlations between the annual melt day time series for ice shelves in these regions, and they are similar to the pattern in the first Principal Component of melt day variability. This pattern has been further shown to be strongly (and inversely) related to October through January SAM, underscoring the importance of SAM, and therefore the constriction of the Southern Westerly Winds around Antarctica, during the austral spring and summer to ice shelf melt in these regions.

The years with the highest numbers of melt days in the Antarctic Peninsula and Bellingshausen Sea sector of West Antarctica lack spatial coherence of melt days elsewhere across the continent. There are few spatial correlations in the melt day time series between Antarctic Peninsula and Abbot ice shelves to ice shelves in other regions. The second Principal Component of melt day variability is the primary mode of variability for the Antarctic Penin-

sula, and it too shows little strength elsewhere. These results imply that the climate forces which cause high melt days on the Antarctic Peninsula are somewhat decoupled from the primary drivers of high melt days across the rest of Antarctica. We have also found mean October through January ENSO values to be positively correlated with melt days on many West Antarctic ice shelves, especially those in the Amundsen Sea sector.

The seasonal changes in firn brightness temperature, described here as Δ_{BT} , provide a useful tool for exploring changes to firn structure over time in regions which experience low amounts of melt. While this method does not quantify exact changes in grain size or ice lens thickness or frequency, it is the product of physical changes in the near-surface firn stratigraphy caused by melt. The grain growth and ice lens development captured by this metric is very likely observable in firn cores, as was noted on the Ross Ice Shelf. The record of Δ_{BT} anomalies can be used to aid in the study of firn development on many Antarctic ice shelves over this time period.

3.6 Acknowledgements

3.7 Data Sources & Availability

Coastline data were downloaded from SCAR Antarctica Digital Coastline Database (https://www.add.scar.org/), last accessed: 2020-01-09. SMMR data were downloaded from NSIDC (https://doi.org/10.5067/C8ZJDDHZAS59) (Gloersen and Francis, 2003). SSM/I and SSMIS data were downloaded from NSIDC (Meier and others, 2019). MEI values were downloaded from NOAA Physical Sciences Laboratory (https://psl.noaa.gov/enso/mei/), last accessed: 2020-11-2. SAM (AAO) data were provided by NOAA/National Weather Service Climate Prediction Center (https://www.cpc.ncep.noaa.gov/products/precip/CWlink

/daily_ao_index/aao/aao.shtml), last accessed: 2020-10-26. ASCAT Enhanced Resolution Image Products were downloaded from Brigham Young University Scatterometer Climate Record Pathfinder (https://www.scp.byu.edu/data/Ascat/SIR/msfa/Ant.html), last accessed: 2021-4-17. MODIS Mosaic was downloaded from NSIDC (Haran and others, 2014).

The melt day dataset produced for this study is available at https://doi.org/10.15784/601457.

3.8 References

Abdalati W and Steffen K (1997) Snowmelt on the greenland ice sheet as derived from passive microwave satellite data. *J. Clim.*, **10**(2), 165–175

Abdalati W and Steffen K (1998) Accumulation and hoar effects on microwave emission in the greenland ice-sheet dry-snow zones. *J. Glaciol.*, **44**(148), 523–531

Arthur JF, Stokes CR, Jamieson SS, Carr JR and Leeson AA (2020) Distribution and seasonal evolution of supraglacial lakes on shackleton ice shelf, east antarctica. *Cryosphere*, **14**(11), 4103–4120

Banwell AF, MacAyeal DR and Sergienko OV (2013) Breakup of the larsen b ice shelf triggered by chain reaction drainage of supraglacial lakes. *Geophys. Res. Lett.*, **40**(22), 5872–5876

Banwell AF, Datta RT, Dell RL, Moussavi M, Brucker L, Picard G, Shuman CA and Stevens LA (2021) The 32-year record-high surface melt in 2019/2020 on the northern george vi ice shelf, antarctic peninsula. *Cryosphere*, **15**(2), 909–925

Barrand N, Vaughan D, Steiner N, Tedesco M, Kuipers Munneke P, Van den Broeke M and Hosking J (2013) Trends in antarctic peninsula surface melting conditions from observations and regional climate modeling. *J. Geophys. Res. Earth. Surf.*, **118**(1), 315–330

Bell RE, Banwell AF, Trusel LD and Kingslake J (2018) Antarctic surface hydrology and impacts on ice-sheet mass balance. *Nat. Clim. Change*, **8**(12), 1044–1052

Benson C (1962) Stratigraphic studies in the snow and firn of Greenland ice sheet, CRREL (SIPRE) research report 70

Bothale RV, Rao P, Dutt C, Dadhwal V and Maurya D (2015) Spatio-temporal dynamics of surface melting over antarctica using OSCAT and QuikSCAT scatterometer data (2001–2014). *Curr. Sci.*, 733–744

Bracegirdle TJ, Colleoni F, Abram NJ, Bertler NA, Dixon DA, England M, Favier V, Fogwill CJ, Fyfe JC, Goodwin I and others (2019) Back to the future: Using long-term observational and paleo-proxy reconstructions to improve model projections of antarctic climate. *Geosci. J.*, **9**(6), 255

Chang T, Gloersen P, Schmugge T, Wilheit T and Zwally H (1976) Microwave emission from snow and glacier ice. *J. Glaciol.*, **16**(74), 23–39

Das SB and Alley RB (2005) Characterization and formation of melt layers in polar snow: observations and experiments from west antarctica. *J. Glaciol.*, **51**(173), 307–312

Datta RT, Tedesco M, Fettweis X, Agosta C, Lhermitte S, Lenaerts JT and Wever N (2019) The effect of foehn-induced surface melt on firn evolution over the northeast antarctic peninsula. *Geophysical Research Letters*, **46**(7), 3822–3831

DeConto RM and Pollard D (2016) Contribution of antarctica to past and future sea-level rise. *Nature*, **531**(7596), 591–597

Dupont T and Alley RB (2005) Assessment of the importance of ice-shelf buttressing to ice-sheet flow. *Geophys. Res. Lett.*, **32**(4)

Fahnestock M and Bamber J (2001) Morphology and surface characteristics of the west antarctic ice sheet. *The West Antarctic ice sheet: behavior and environment. Washington, DC, American Geophysical Union*, 13–27

Fahnestock MA, Abdalati W and Shuman CA (2002) Long melt seasons on ice shelves of the antarctic peninsula: an analysis using satellite-based microwave emission measurements. *Ann. Glaciol.*, **34**, 127–133

Fogt RL, Bromwich DH and Hines KM (2011) Understanding the sam influence on the south pacific enso teleconnection. *Clim. Dyn.*, **36**(7-8), 1555–1576

Gilbert E and Kittel C (2021) Surface melt and runoff on antarctic ice shelves at 1.5°c, 2°c and 4°c of future warming. *Geophys. Res. Lett.*, e2020GL091733

Gloersen P (1992) *Arctic and Antarctic sea ice, 1978-1987: Satellite passive-microwave observations and analysis.* 511, Scientific and Technical Information Program, National Aeronautics and Space Administration

Gloersen P and Francis EA (2003) Nimbus-7 SMMR antenna temperatures. NASA National Snow and Ice Data Center Distributed Active Archive Center, Version 1, South 18H and 37V. Doi: https://doi.org/10.5067/C8ZJDDHZAS59. Last accessed: 2017-7-19.

Golledge NR, Keller ED, Gomez N, Naughten KA, Bernales J, Trusel LD and Edwards TL (2019) Global environmental consequences of twenty-first-century ice-sheet melt. *Nature*, **566**(7742), 65–72

Haran T, Bohlander J, Scambos T, Painter T and Fahnestock M (2014, updated 2019) Modis mosaic of antarctica 2008-2009 (moa2009) image map, version 1. NSIDC: National Snow and Ice Data Center Distributed Active Archive Center, Version 1 South 19H and 37V. Doi: https://doi.org/10.7265/N5KP8037. Last accessed: 2020-2-7

Johnson A, Fahnestock M and Hock R (2020) Evaluation of passive microwave melt detection methods on antarctic peninsula ice shelves using time series of sentinel-1 SAR. *Remote Sens. Environ.*, **250**, 112044

Jun SY, Kim JH, Choi J, Kim SJ, Kim BM and An SI (2020) The internal origin of the west-east asymmetry of antarctic climate change. *Sci. Adv.*, **6**(24), eaaz1490

Kingslake J, Ely JC, Das I and Bell RE (2017) Widespread movement of meltwater onto and across antarctic ice shelves. *Nature*, **544**(7650), 349–352

Kittel C, Amory C, Agosta C, Jourdain NC, Hofer S, Delhasse A, Doutreloup S, Huot PV, Lang C, Fichefet T and others (2021) Diverging future surface mass balance between the antarctic ice shelves and grounded ice sheet. *Cryosphere*, **15**(3), 1215–1236

Knuth SL, Tripoli GJ, Thom JE and Weidner GA (2010) The influence of blowing snow and precipitation on snow depth change across the ross ice shelf and ross sea regions of antarctica. *J. Appl. Meteorol. Climatol.*, **49**(6), 1306–1321

Macelloni G, Brogioni M, Pampaloni P and Cagnati A (2007) Multifrequency microwave emission fromthe dome-c area on the east antarctic plateau: temporal and spatial variability. *IEEE Trans. Geosci. Remote Sens.*, **45**(7), 2029–2039

Machguth H, MacFerrin M, van As D, Box JE, Charalampidis C, Colgan W, Fausto RS, Meijer HA, Mosley-Thompson E and van de Wal RS (2016) Greenland meltwater storage in firn limited by near-surface ice formation. *Nat. Clim. Change*, **6**(4), 390–393

Marshall GJ (2007) Half-century seasonal relationships between the southern annular mode and antarctic temperatures. *Int. J. Climatol.*, **27**(3), 373–383

Mayewski PA, Meredith M, Summerhayes C, Turner J, Worby A, Barrett P, Casassa G, Bertler NA, Bracegirdle T, Naveira Garabato A and others (2009) State of the antarctic and southern ocean climate system. *Rev. Geophys.*, **47**(1)

Meier WN, Wilcox H, Hardman MA and Stewart JS (2019) DMSP SSM/I-SSMIS daily polar gridded brightness temperatures. National Snow and Ice Data Center Distributed Active Archive Center, Version 5, South 19H and 37V. Doi: https://doi.org/10.5067/QU2UYQ6T0B3P. Last accessed:2020-12-24

Mote TL, Anderson MR, Kuivinen KC and Rowe CM (1993) Passive microwave-derived spatial and temporal variations of summer melt on the greenland ice sheet. *Ann. Glaciol.*, **17**, 233–238

Munneke PK, Luckman A, Bevan S, Smeets C, Gilbert E, Van den Broeke M, Wang W, Zender C, Hubbard B, Ashmore D and others (2018) Intense winter surface melt on an antarctic ice shelf. *Geophys. Res. Lett.*, **45**(15), 7615–7623

Naik SS, Thamban M, Laluraj C, Redkar B and Chaturvedi A (2010) A century of climate variability in central dronning maud land, east antarctica, and its relation to southern annular mode and el niño-southern oscillation. *J. Geophys. Res. Atmos.*, **115**(D16)

Nicolas JP and Bromwich DH (2014) New reconstruction of antarctic near-surface temperatures: Multidecadal trends and reliability of global reanalyses. *J. Clim.*, **27**(21), 8070–8093

Paolo FS, Fricker HA and Padman L (2015) Volume loss from antarctic ice shelves is accelerating. *Science*, **348**(6232), 327–331

Picard G, Fily M and Gallée H (2007) Surface melting derived from microwave radiometers: a climatic indicator in antarctica. *Ann. Glaciol.*, **46**, 29–34

Pörtner H, Roberts D, Masson-Delmotte V, Zhai P, Tignor M, Poloczanska E, Mintenbeck K, Alegría A, Nicolai M, Okem A, Petzold J, Rama B and Weyer N (2019) *IPCC Special Report on the Ocean and Cryosphere in a Changing Climate*. IPCC

Scambos T, Fricker HA, Liu CC, Bohlander J, Fastook J, Sargent A, Massom R and Wu AM (2009) Ice shelf disintegration by plate bending and hydro-fracture: Satellite observations and model results of the 2008 wilkins ice shelf break-ups. *Earth Planet. Sci. Lett.*, **280**(1-4), 51–60

Smith KL and Polvani LM (2017) Spatial patterns of recent antarctic surface temperature trends and the importance of natural variability: lessons from multiple reconstructions and the cmip5 models. *Clim. Dyn.*, **48**(7-8), 2653–2670

Stokes CR, Sanderson JE, Miles BW, Jamieson SS and Leeson AA (2019) Widespread distribution of supraglacial lakes around the margin of the east antarctic ice sheet. *Sci. Rep.*, **9**(1), 1–14

Tedesco M (2009) Assessment and development of snowmelt retrieval algorithms over antarctica from k-band spaceborne brightness temperature (1979–2008). *Remote Sens. Environ.*, **113**(5), 979–997

Tedesco M and Monaghan AJ (2009) An updated antarctic melt record through 2009 and its linkages to high-latitude and tropical climate variability. *Geophys. Res. Lett.*, **36**(18)

Tedesco M, Abdalati W and Zwally H (2007) Persistent surface snowmelt over antarctica (1987–2006) from 19.35 ghz brightness temperatures. *Geophys. Res. Lett.*, **34**(18)

Torinesi O, Fily M and Genthon C (2003) Variability and trends of the summer melt period of antarctic ice margins since 1980 from microwave sensors. *J. Clim.*, **16**(7), 1047–1060

Trusel L, Frey KE and Das SB (2012) Antarctic surface melting dynamics: Enhanced perspectives from radar scatterometer data. *J. Geophys. Res. Earth Surf.*, **117**(F2)

Trusel LD, Frey KE, Das SB, Munneke PK and Van Den Broeke MR (2013) Satellite-based estimates of antarctic surface meltwater fluxes. *Geophys. Res. Lett.*, **40**(23), 6148–6153

Trusel LD, Frey KE, Das SB, Karnauskas KB, Munneke PK, Van Meijgaard E and Van Den Broeke MR (2015) Divergent trajectories of antarctic surface melt under two twenty-first-century climate scenarios. *Nat. Geosci.*, **8**(12), 927–932

Tuckett PA, Ely JC, Sole AJ, Livingstone SJ, Davison BJ, van Wessem JM and Howard J (2019) Rapid accelerations of antarctic peninsula outlet glaciers driven by surface melt. *Nat. Commun.*, **10**(1), 1–8

Turner J, Lu H, White I, King JC, Phillips T, Hosking JS, Bracegirdle TJ, Marshall GJ, Mulvaney R and Deb P (2016) Absence of 21st century warming on antarctic peninsula consistent with natural variability. *Nature*, **535**(7612), 411–415

Turner J, Marshall GJ, Clem K, Colwell S, Phillips T and Lu H (2020) Antarctic temperature variability and change from station data. *Int. J. Climatol.*, **40**(6), 2986–3007

Van Wessem JM, Van De Berg WJ, Noël BP, Van Meijgaard E, Amory C, Birnbaum G, Jakobs CL, Krüger K, Lenaerts J, Lhermitte S and others (2018) Modelling the climate and surface mass balance of polar ice sheets using racmo2–part 2: Antarctica (1979–2016). *The Cryosphere*, **12**(4), 1479–1498

Zwally HJ and Fiegles S (1994) Extent and duration of antarctic surface melting. *J. Glaciol.*, **40**(136), 463–475

4 The response of ice in the Filchner-Ronne region to ocean-driven subshelf melt[5]

Abstract

The Filchner-Ronne region contains the second largest ice shelf in Antarctica. Changes in ocean temperatures or circulation could bring increased ice shelf basal melting, which in turn has direct consequences on the evolution of the Antarctic Ice Sheet in this region and can impact global sea levels. In this chapter we use ice sheet modeling to study the response of the ice sheet and ice shelf in the Filchner-Ronne region during the period of 2015 to 2100 to a set of ocean warming scenarios that involve raising ocean potential temperatures up to 6 °C. To tune the ice sheet model parameters which control ice flow, we built a surrogate model based on a ensemble of calibration runs, and then compared the surrogate model results to observed ice velocities in order to develop a posterior distribution for the parameters. We used parameter sets generated from the posterior distribution to perform an ensemble of model runs for each ocean warming scenario. With no change in ocean temperature, by the year 2100 the mass of ice above flotation in the region increased by 8020±560 Gigatons (Gt) relative to 2015, while it decreased by 660±660 Gt for the +2 °C scenario and by 28370±1590 Gt for the +6°C scenario. This corresponds to a global sea level change ranging from –24 mm to +85 mm at year 2100. The additional mass losses with increasing ocean temperature are associated with increased mass fluxes through the grounding lines, increased ice stream velocities, and increased grounding line retreat rates. In the +6°C scenario significant portions of the ice shelf disappear by 2100.

4.1 Introduction

The Filchner-Ronne drainage basin of Antarctica (3.7 million km^2 including the ice shelves) contains 25% of all the ice in the Antarctic ice sheet, and it supports the second largest ice shelf on the continent (430,000 km^2). The Filchner-Ronne Ice Shelf experiences the fewest days of melt per year of any ice shelf (Figure 3.1 and 3.5), and some of the lowest

---

[5]In preparation for publication by Johnson, A., Aschwanden, A., Torsten, A., & Hock, R.

surface melt rates of any ice shelf (Jakobs et al., 2020). Ice shelf collapse as a function of surface melt driven hydrofracture is thought to require certain thresholds of sustained surface melt (Trusel et al., 2015), yet due to low temperatures and low melt rates, this region of Antarctica is one of the least likely to experience such an ice shelf collapse. Ocean-driven subshelf melt however can provides much greater melt rates across the region, both now and into the future under projected emission scenarios (Hill et al., 2021).

Ocean forcing provides an important control on ice shelf stability in this region. Ocean surface temperatures and circulations interact with the ice shelf through multiple processes. Increasing surface temperatures reduce sea ice production, which could initially decrease melting on the Filchner-Ronne Ice Shelf as there will be less high-salinity, dense seawater to push into the freshwater cavities under the Ronne Ice Shelf (Nicholls and Østerhus, 2004). The converse of this has been directly observed, as increased sea ice production in the Weddell Sea since 2015 has strengthened this circulation (Hattermann et al., 2021). Greater temperature increases however could potentially lead to Warm Deep Water from the Weddell Sea entering the subshelf environment, which could greatly increase melting (Hellmer et al., 2012). Coupled ocean and ice sheet models have been able to reproduce both these phenomena (Naughten et al., 2021). Their work demonstrated that a global mean surface temperature increase of 7 °C was required to destabilize the ice shelves in this region, although moderate warming has an impact on mass fluxes and sea level contributions. Changes to meridional winds could have impacts which increase ice shelf basal melting by an order of magnitude (Hazel and Stewart, 2020). The thinning and destablization of ice shelves is connected to ice mass losses through physical mechanisms such as the loss of backstress (Dupont and Alley, 2005), with the potential for Marine Ice Sheet Instability (Weertman, 1964).

The aim of this work is to provide projections of the evolution of the ice sheet in the Filchner-Ronne region in response to several ocean warming scenarios. We leverage the computational efficiency of the Parallel Ice Sheet Model (PISM) and modern bed topographies

(Morlighem, 2020) to provide numerical simulations at high resolution, and we use surrogate model analysis to decrease the uncertainties of our projections.

4.2 Methods

4.2.1 Overview

We run PISM for the period 2015–2100 using seven hypothetical ocean temperature scenarios to test the response of the grounded ice to increasing amounts of basal melt and ice shelf thinning. These scenarios use the Potsdam Ice-shelf Cavity mOdel (PICO) to force ice shelf basal melt with a step change in ocean potential temperatures at depth in front of the ice shelf of +0°C, +1°C, up to +6°C. The surface forcing is held constant during this time period.

For each scenario, we perform an ensemble of PISM model runs at 2 km resolution, with specific mechanical properties set by the results of a calibration. This calibration uses a Bayesian analysis of surrogate model results and observed surface velocities to produce a posterior distribution of expected parameter values (Section 4.2.5). The approach aims to reduce the model result uncertainty by using parameter values likely to reproduce modern velocity fields, based on initial tests of a much wider parameter space (Brinkerhoff et al., 2021). The workflow is illustrated in Figure 4.1.

4.2.2 Model description

PISM is a shallow ice and shallow shelf approximation model for the evolution of glacier ice (Winkelmann et al., 2011), with temperature-dependent ice flow thermomechanically coupled to the evolution of enthalpy (Aschwanden et al., 2012). PISM is chosen for its robust performance and ability to model large areas at relatively high resolutions. It has been used to provide projections of ice sheet evolution at the continent scale (e.g. Aschwanden et al., 2019, Golledge et al., 2019, Albrecht et al., 2020) as well as at the regional scale (Habermann et al., 2013). PISM models are used in the Ice Sheet Model Intercomparison Project (Seroussi
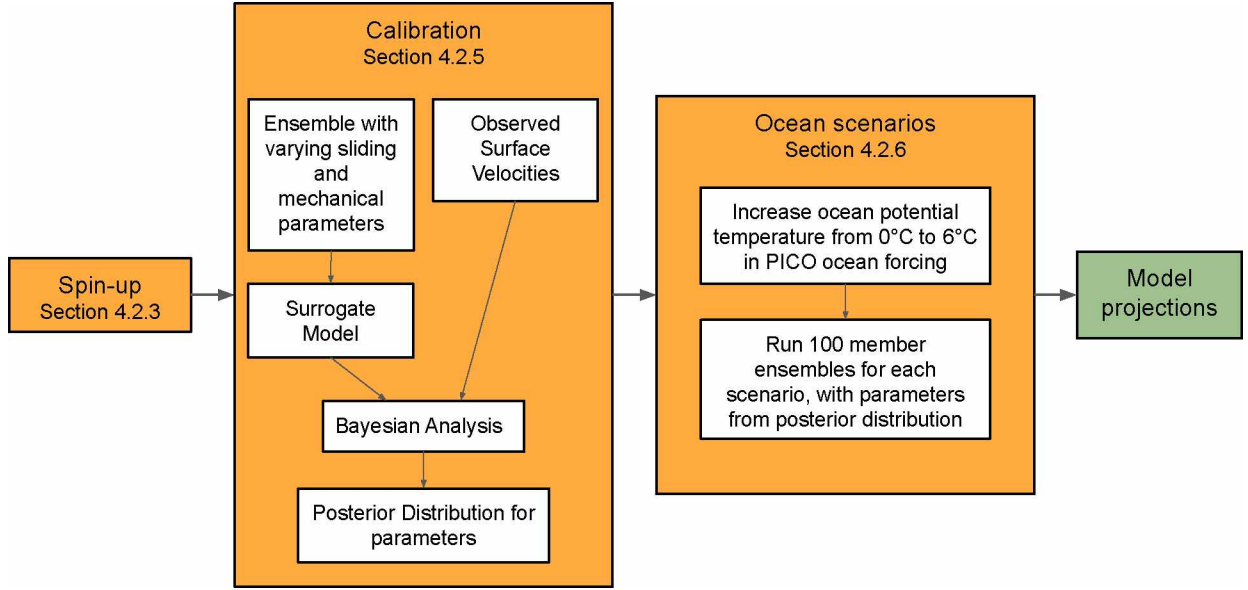
Figure 4.1: Description of modeling workflow. Yellow boxes show major steps (outlined in methods section), and inner white boxes show sub-steps.

et al., 2020), Initialization Model Intercomparison Project (Seroussi et al., 2019), and the Antarctic Buttressing Model Intercomparison Project (Sun et al., 2020).

Within PISM the application of the shallow shelf approximation for membrane stresses of ice allows for the sliding of grounded ice and the development of ice streams (Bueler and Brown, 2009). Subglacial processes and the stresses at the basal interface model sliding stresses and provide important controls for ice dynamics. A power law is applied for the basal shear stress τ_b:

$$\tau_b = -\tau_c \frac{\mathbf{u}}{u_{th}^q |\mathbf{u}|^{1-q}} \tag{4.1}$$

The basal shear stress τ_b is a function of the yield stress τ_c, the basal velocity $\mathbf{u}$, and a sliding velocity threshold u_{th}. The exponent q allows for plastic, pseudo-plastic, or linear sliding. Sliding occurs when the driving stress is greater than a yield stress τ_c at the bed, as given by the Mohr-Coulomb criterion:

$$\tau_c = N_{\text{till}} \tan \phi \tag{4.2}$$

Here ϕ is the till friction angle (Equation 4.3), and N_{till} is the effective pressure (Equation 4.4). The till friction angle is a stepwise function calculated at every grid point,

$$\phi(b) = \begin{cases} \phi_{\text{min}}, & b \leq b_{\text{base}} \\[2mm] \phi_{\text{min}} + \frac{\phi_{\text{max}} - \phi_{\text{min}}}{b_{\text{range}}}(b - b_{\text{base}}), & b_{\text{base}} < b < b_{\text{base}} + b_{\text{range}} \\[2mm] \phi_{\text{max}}, & b \geq b_{\text{base}} + b_{\text{range}} \end{cases} \tag{4.3}$$

The till friction angle increases linearly from ϕ_{min} at minimum bed elevation b_{base} up to ϕ_{max} over a height of b_{range} above b_{base}. The other term in Equation 4.2), effective pressure, is given by:

$$N_{\text{till}} = \min \left\{ P_0, N_0 \left(\frac{\delta P_0}{N_0}\right)^s 10^{(e_0/C_c)(1-s)} \right\} \tag{4.4}$$

The effective pressure is a function of the ice overburden pressure P_0, till effective reference pressure N_0, till effective fraction overburden δ, till reference void ratio e_0, and till compressibility coefficient C_c. PISM models the evolution of water in the till. The till wetness s is the ratio of effective to potential thickness of water in the till. This formulation of yield stress τ_c, till friction angle ϕ, and effective pressure N_{till} has been shown to reproduce the emergence of ice streams in Antarctica (Martin et al., 2011). The full list of terms and their default values are given in Table 4.1).

4.2.3   Model setup and spinup

We represent the Filchner-Ronne drainage basin in PISM using a 1799×2159 km^2 grid at 1 km resolution. Ice shelf maximum extent is masked to the extent in 2016 preventing further advance, although ice shelves are allowed to retreat. At the domain boundaries, we force the gradients of surface elevation and thickness to be zero. Therefore modeled ice

Table 4.1: Default model parameters. These parameters values were used in the calibration and application of the model, except where otherwise stated.

Parameter	Symbol	Unit	Default value
SIA enhancement factor	SIAe		1.4
SSA enhancement factor	SSAe		1.0
Pseudo-plastic q	q		0.9
Pseudoplastic sliding velocity threshold	u_{th}	m a^{-1}	100
Till effective fraction overburden	δ		0.07
Till friction angle (min)	ϕ_{min}	degree	1
Till friction angle (max)	ϕ_{min}	degree	45
Till friction angle bed (min)	b_{base}	m	-900
Till friction angle bed (range)	b_{range}	m	2400
Till reference void ratio	e_0		0.69
Till compressibility coefficient	C_c		0.12
Till reference effective pressure	N_0	Pa	1000

velocities directly adjacent to the boundaries are unlikely to be realistic.

The regional model was spun up over a long time period. A 10 km model was run with fixed geometry and no mass forcing was run for approximately 100 kyr, followed by a 10 kyr model run to reach dynamic equilibrium, and then a 1 kyr run forced to the thickness of Bedmap2 (Fretwell et al., 2013) to ensure present-day ice geometry. We then switched the ice sheet bed topography and thicknesses to that of Bedmachine (Morlighem, 2019), and continued the model spinup for an additional 500 years with ice thicknesses forced to remain constant. The additional 500 years were necessary to allow for parts of the bed to reach the pressure-melting temperature after switching bed topographies, and thus allow sliding for ice streams.

4.2.4   Model forcing

PISM was forced by near-surface air temperature and precipitation fields from RACMO2.3 (van Wassem et al., 2018), applied to the Community Earth System Model Version 2 (CESM2; Danabasoglu et al., 2020). CESM2 was downscaled to 1 km, and the mean of surface temperature and climatic mass balance over 1950–2014 were used as constant forcing. During the spinup ocean temperature and ice shelf basal mass fluxes were generated

with the Finite Element/columE Sea ice-Ocean Model (FESOM: Sidorenko et al., 2015). In the Filchner-Ronne region FESOM is capable of reproducing the subshelf circulation to produce realistic shelf basal melt fields (Timmermmann and Goeller, 2017).

Throughout the spinup and the application of the model in this work, all forcing remained constant except the ocean forcing. After this spinup, the ocean forcing was changed to apply PICO (Reese et al., 2018) for the rest of this study. PICO is an ocean model in which warm water reaches the base of the ice shelf at the grounding line and the the ocean overturning is calculated for the cold fresh meltwater rising under the ice shelf. The inputs for PICO include the mean ocean salinity and potential temperature at the depth of the bottom of the front of the ice shelf across an entire drainage basin, as well as a few ocean overturning parameters. While PICO does not capture the complexities of ocean circulations underneath the ice shelf, it provides a realistic way to model melt using different ocean temperatures (Hill et al., 2021).

4.2.5   Calibration and model evaluation

Some mechanical parameters of the model, especially those related to sliding, must be tuned in order to accurately reproduce observed surface ice velocities. These parameters include the pseudo-plastic q (Equation 4.1), till effective fraction overburden δ (Equation 4.4) and till friction angle depth minimum b_{base} and range b_{range} (Equation 4.2 and 4.3), as well as the Shallow Ice and Shallow Shelf enhancement factors (SIAe and SSAe, respectively). These enhancement factors provide coefficients applied to the Shallow Ice and Shallow Shelf approximation stress to strain relationships. We determined a range of physically plausible values for these parameters (Table 4.2) to be used in the calibration. The higher ends of the Shallow Shelf Approximation enhancement factor value produce much higher velocities than observed for floating ice, and high values of either of the enhancement factors must be used with great caution. They have been included to ensure that fully stimulating the development of ice streams with realistic surface velocities was possible within the tuning

Table 4.2: Model parameters which were varied in the calibration procedure. Parameters of each ensemble member were drawn uniformly from within the stated ranges for the calibration. The spinup values were used for the 500 years of spinup with Bedmachine.

parameter	symbol	spinup value	range for sensitivity
SIA enhancement factor	SIAe	1.0	0.25 to 2.5
SSA enhancement factor	SSAe	1.0	0.5 to 1.5
Pseudo-plastic q	q	0.75	0.25 to 1
Till effective fraction overburden	δ	0.04	0.03 to 0.11
Till friction bottom elevation	b_{base}	-900	-1500 to 500
Till friction elevation range	b_{range}	2400	500 to 2500

parameter set.

We created an 300 member ensemble with parameter values within these ranges. A Sobel Sequence generated samples from a uniform distribution of all the six parameters (Table 4.2). We applied the parameter set of each ensemble member to PISM on a 2 km grid, and then ran the model forward for 50 years. The atmosphere and ocean inputs were held constant during this period. Ocean forcing was provided by PICO using modern temperatures and salinities (Schmidtko et al., 2014), and with PISM default overturning parameters.

We used the output of the calibration runs to train a surrogate model, and then compared that to observed ice velocities. Following the methodology of Brinkerhoff et al. (2021), we trained a neural network based on the modes of variability of the resultant velocity fields of the ensemble of calibration runs with respect to the input parameters. This produced a surrogate model which could predict the velocity fields produced by any parameter combination. We compared the surrogate model results to an observed velocity field of the region, taken from the ITSLIVE map of 2018 velocities (Gardner et al., 2019). We regridded the observed velocities to the same 2 km grid as the model. We used Markov Chain Monte Carlo sampling of the surrogate model parameter space to produce a set of emulators which predicted the probabilities of parameter values. These were merged into a single posterior distribution for the probability of values of each of these physical parameters. The posterior distribution results are shown in Figure 4.2. The observed surface velocities are shown in Figure 4.3.
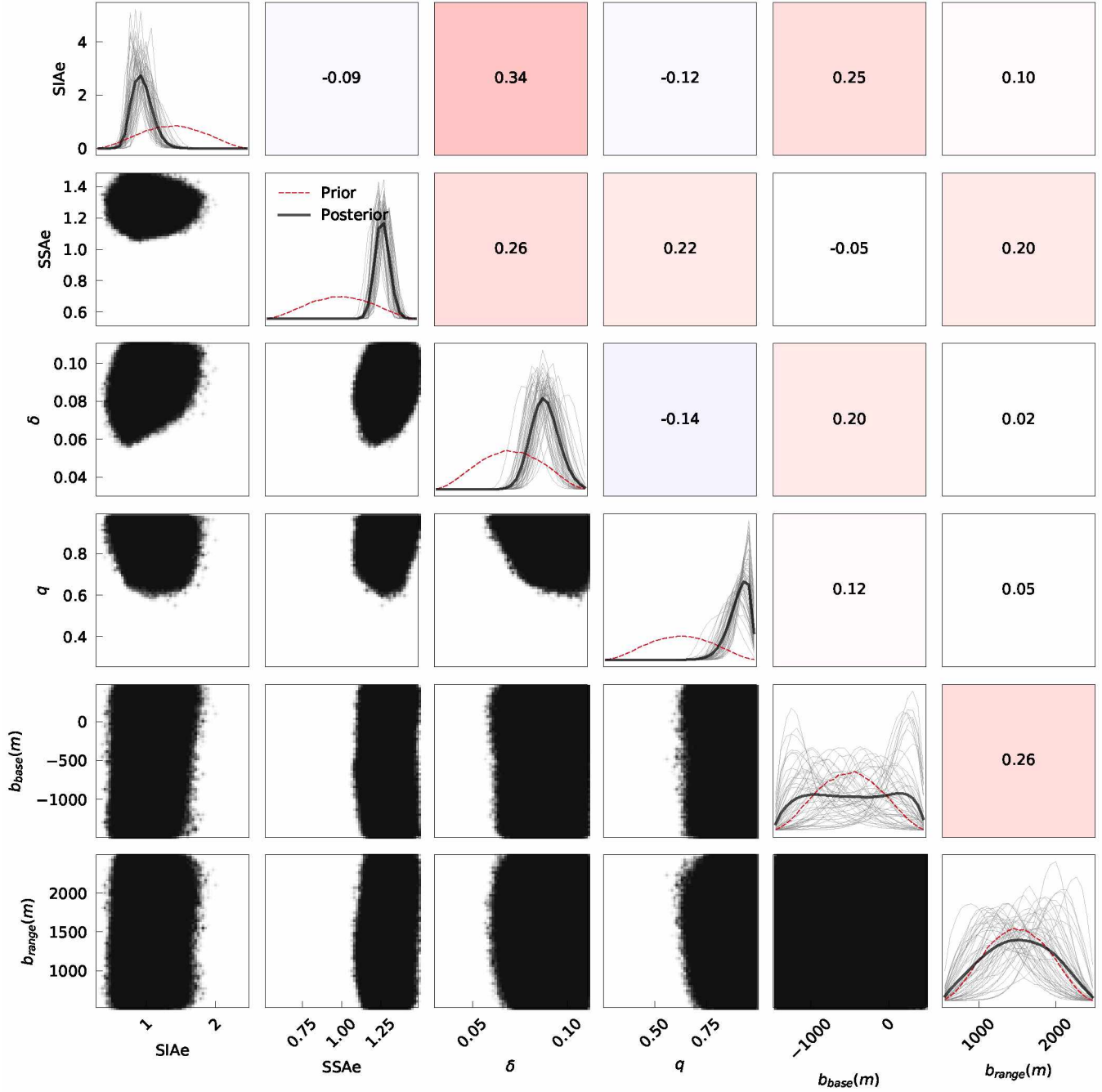
Figure 4.2: Surrogate model analysis results. Color-coded boxes above the diagonal show the correlation coefficients between parameters, the diagonal shows prior (red) and posterior distributions (black) along with each emulator (grey), and plots below the diagonal show all the parameter configurations.

We use the posterior distribution to generate values for each of these six parameters to use in our ocean warming scenario driven projections. One example of the model agreement with observed surface velocities is shown in Figure 4.4. For this run we chose parameter values near the peak of each distribution, and ran the model for 50 years at 1 km resolution. Overall, ice velocities are reproduced to within 100 m a^{-1} near the grounding line of the Institute and Rutford ice streams (Figure 4.3), which both have observed velocities of approx 360-400 m a^{-1} at the grounding lines. The most prominent velocity difference is found on the Moller ice stream, where observed grounding line surface velocities are approximately 100 to 150 m a^{-1} and the ice stream does not extend more than 100 km inland. The model instead produces an ice stream which stretches almost towards the inland domain boundary and has velocities of approximately 300 m a^{-1} at the grounding line.

4.2.6   Ocean warming scenarios

We created a set of experiments raising ocean potential temperatures at depth along the front of the ice shelf from their present day values by (Schmedtko et al., 2014) by +0°C to +6°C at 1°C intervals. These changes were imposed in PICO as a step change, and an ensemble of 100 PISM runs at 2 km resolution from 2015–2100 was performed for each scenario. After the step change in ocean temperature, we held ocean and surface forcing constant for the rest of the time period.

Only the lowest warming scenarios presented here are realistic to projected emission scenarios within the century, with ocean warming at depth in this region beyond +1 °C being well outside the range of 21st century warming under RCP8.5 (Little and Urban, 2016). However, changes in ocean circulation, potentially possible in the 21st century, can cause an order of magnitude increase in ice shelf melting in the region (Hazel and Stewart, 2020, Naughten et al., 2021). PICO does not capture lateral ocean circulation, but it does allow for a great deal of iteration and testing of many scenarios in PISM. The +6°C warming scenario is especially unrealistic without some catastrophic event, yet it provides a forcing
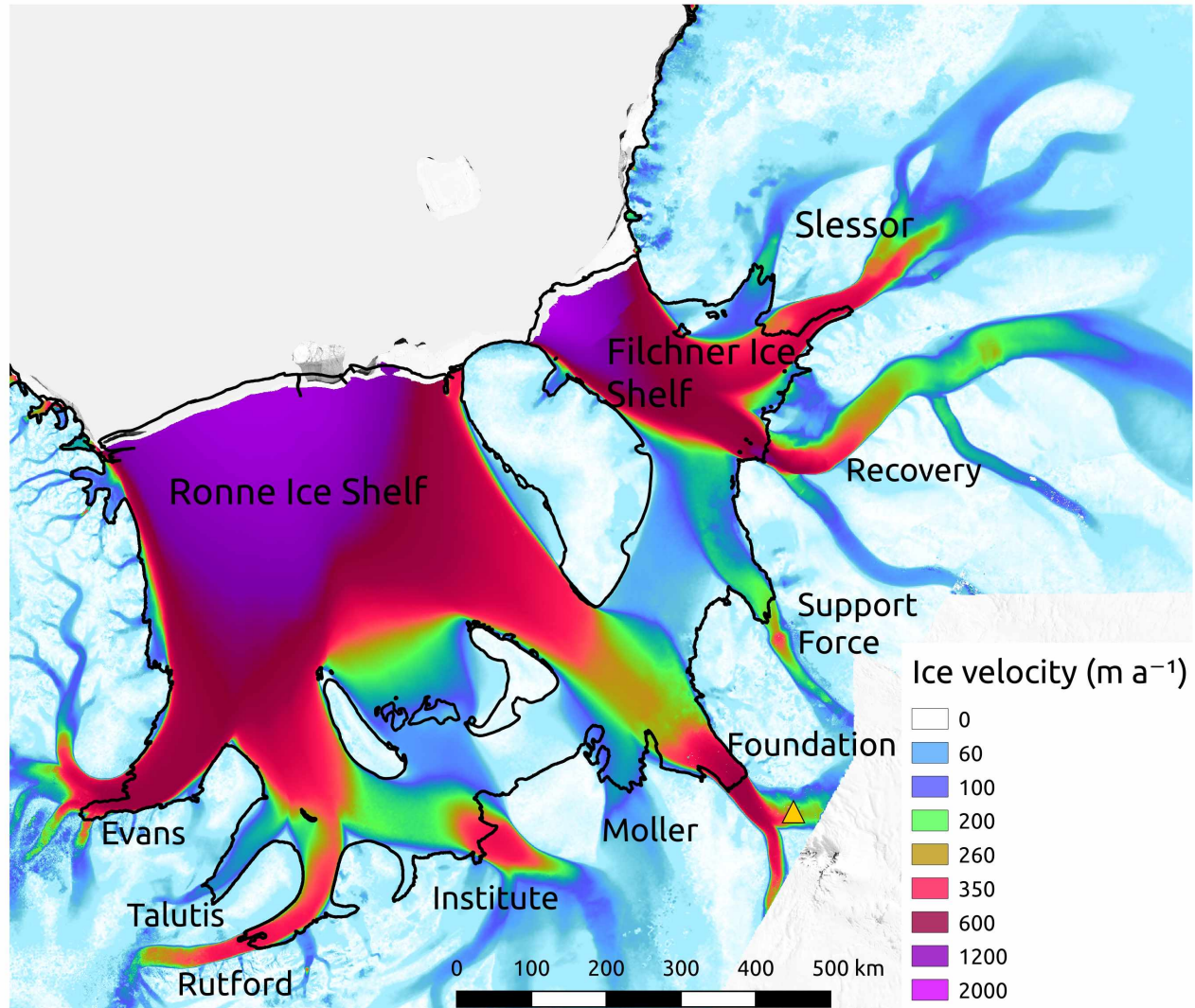
Figure 4.3: Map of the model domain showing ice velocities, with ice streams labeled. Grounding lines shown in black. Velocities are 2018 velocities from ITSLIVE, ice shelf outlines are 2020 outlines from SCAR, and the background is a 2009 Moderate Resolution Imaging Spectroradiometer mosaic from the National Snow and Ice Datacenter (Haran et al., 2014). Ice streams are labeled by name. Note that Support Force refers to Support Force Glacier.
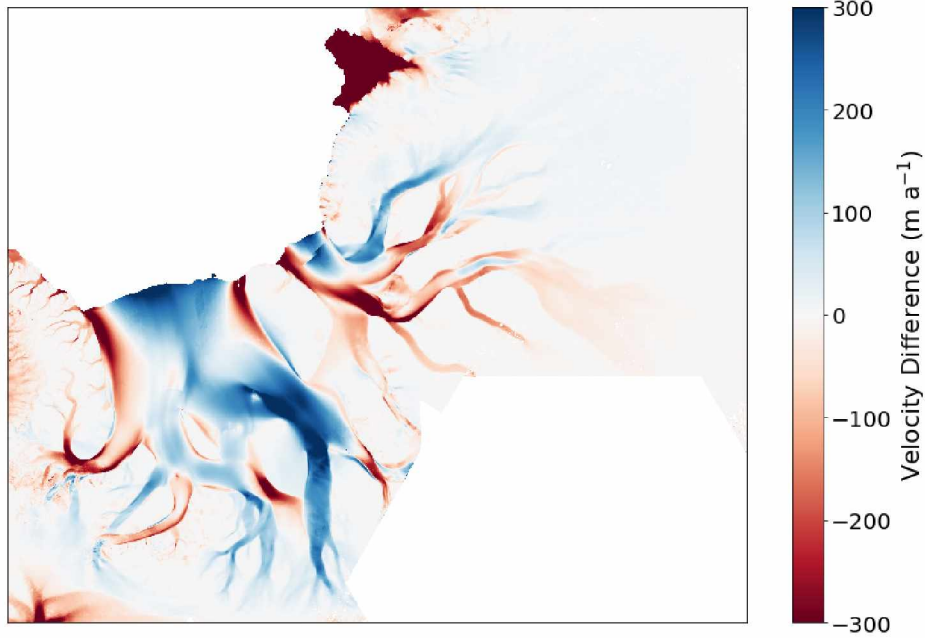
Figure 4.4: Difference between modeled and observed surface velocities (m a^{-1}).

comparable to and perhaps more realistic than the ice sheet "float-kill" criterion used in the Antarctic Buttressing Model Intercomparison Project (Sun et al., 2020).

For each ocean temperature increase scenario we run a 100 member ensemble in PISM. The values of tuned physical parameters are drawn from the resulting posterior distribution of the Bayesian analysis of the results of the surrogate calibration models and observed present day surface velocities (Section 4.2.3). The frequency of the drawn parameter values for these 100 member ensembles are given in Figure 4.5.

4.3 Results

Differences in mean ice mass above flotation for the four ocean warming scenarios of +0 °C, +2 °C, +4 °C, and +6 °C are shown in Figure 4.6. Increased ocean warming is directly related to decreasing ice mass. By the end of the time period, the mean ice mass above flotation varies by up to 36,000 Gt between scenarios, with sea-level contributions at 2100 varying from −24 to +85 mm across the four scenarios, assuming an ocean area of 362.5 million km^2. The trajectories of melt diverge significantly, and after just 20 years there is
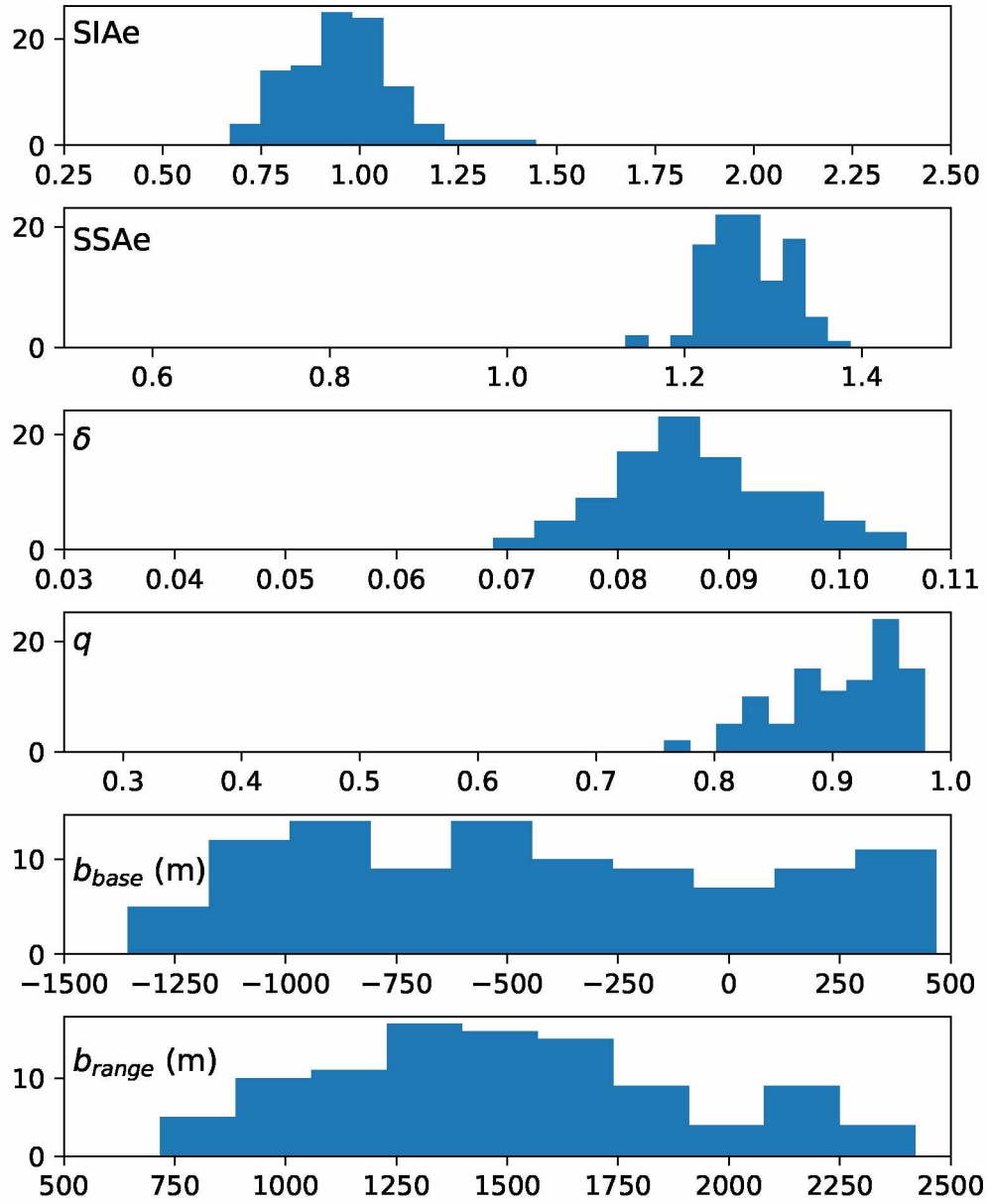
Figure 4.5: Frequency of parameter values in climate simulation ensemble, shown here as the total occurrences for each range. Parameters sampled from posterior (Figure 4.2).
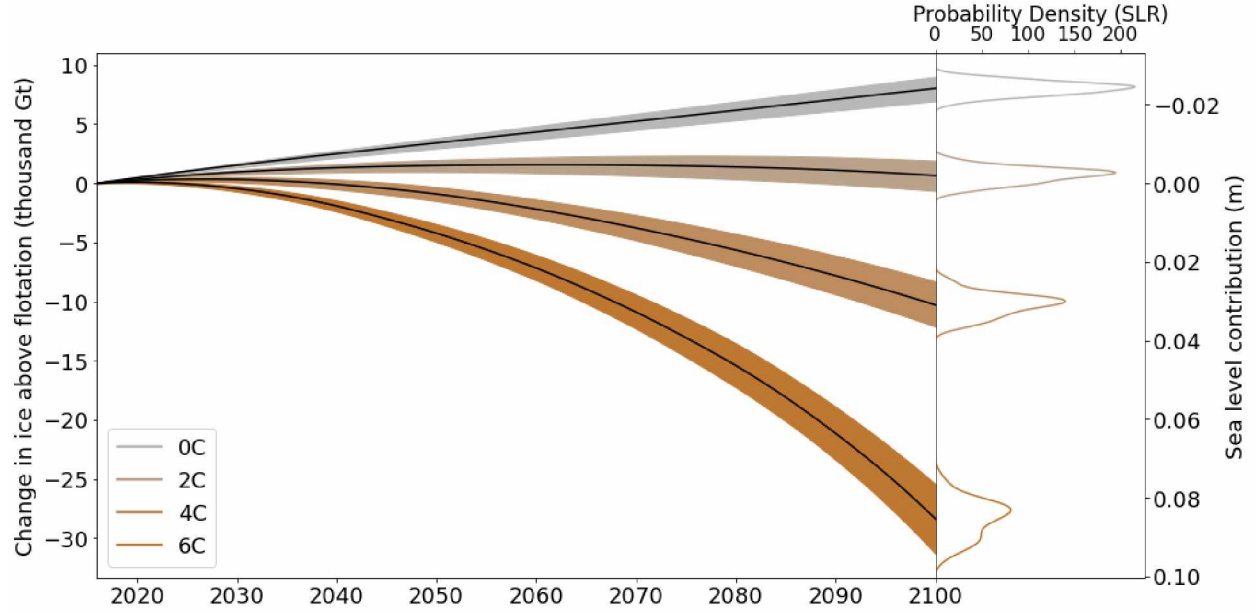
Figure 4.6: Ice mass above flotation and corresponding sea-level contribution for 2015–2100 for four ocean warming scenario. The 95% confidence interval of each scenario is shaded. Probability of ensemble results is given with sea level rise (SLR).

little overlap in the 95% confidence interval in ice mass between each of these four scenarios.

Additional climate scenarios help illustrate the rate of mass decrease with ocean temperature. The ice mass above flotation at the the end of the time period (year 2100) is shown in Figure 4.7 for all scenarios. The rate of total mass change with respect to ocean temperature shows linearity between +0 °C and +4 °C, with a rate of –4600 Gt ice above flotation per °C (14 mm sea level rise per °C) at year 2100. This rate becomes more negative with ocean temperature after the +4 °C scenario.

Thinning at the grounding line and throughout the ice shelf has a direct impact on the flux through the grounding line. The total grounding line flux shows significant variation among these scenarios, especially as time increases (Figure 4.8). While the grounding line fluxes range from –218 to –277 Gt a^{-1} between scenarios at the beginning, by the end of the time period they range from –252 to –1301 Gt a^{-1}. The rate of the grounding line flux becomes more negative with increasing ocean temperature. Over 2015–2100, linear approximations for the rate of change of the grounding line flux over time in each scenario range from –0.59
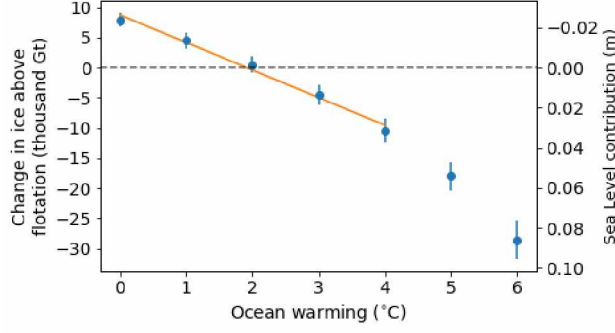
Figure 4.7: Ice mass above flotation at year 2100 for seven ocean temperature increase scenarios, with 95% confidence interval of mass shown. Orange line shows the linear fit of the mean ice mass with ocean temperature over the interval of the +0 °C to +4 °C scenarios.

Gt a^{-2} at +0 °C to –9.86 Gt a^{-2} at +6 °C.

4.4   Discussion

While Antarctica is projected to lose mass in the 21st century (Seroussi et al., 2020), and some regions such as the Amundsen Sea Sector of West Antarctica are losing considerable mass today (Zwally et al., 2021), the results presented here indicate that under near-present day climate forcing the Filchner-Ronne region is gaining mass. Figure 4.9 highlights the terms of this regional mass balance. The surface climate forcing uses 1950–2014 mean values from RACMO, and forces surface mass gains on the order of 392 Gt a^{-1} across the entire region. With PICO for ocean forcing, the +0 °C scenario shows mass gain due to freeze-on at the front of the Filchner-Ronne Ice Shelf, although with increased ocean warming basal melt dominates the mass balance.

Direct observations of the Filchner-Ronne region from time series of surface altimetry (Zwally et al., 2021) and gravimetry (Groh and Horwath, 2021) indicate that the region is indeed likely remaining constant or gaining mass. Under either the RCP 2.6 or 8.5 emission scenarios, this region is unlikely to contribute to sea level rise by the end of the 21st century as increased accumulation is expected to offset the limited increases in basal melting (Hill et al., 2021), although unlikely possibilities exist for ice shelf collapse and ice stream retreat with significant positive sea level contributions. The experiments provided here demonstrate
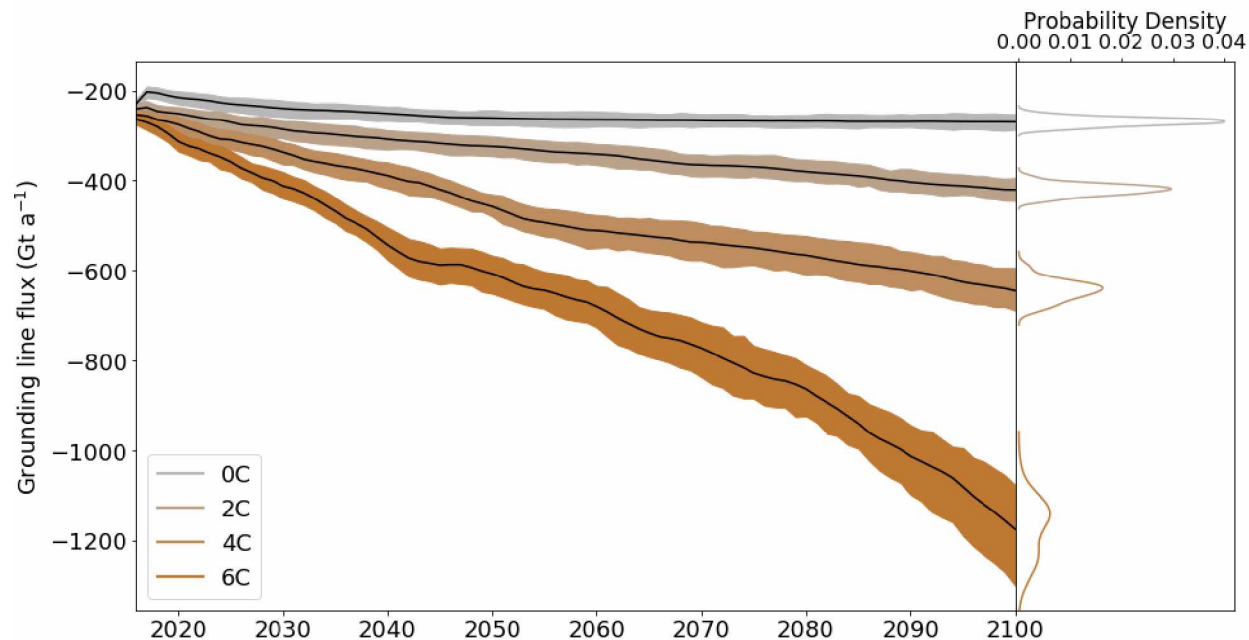
Figure 4.8: Annual ice flux through the grounding line. The 95% confidence interval of each scenario is shaded. Negative flux values indicate ice being removed from the ice sheet at the grounding line.

the possible role of ocean heating in the evolution of the region, as well as highlight how and when ice shelf collapse and ice stream acceleration occur.

The ice sheet response by the year 2100 becomes more negative with increasing ocean temperature (Figure 4.7). The temperature of $+4$ °C appears to be an inflection point, with the rate of ice mass decrease with temperature becoming more negative at higher temperatures. One reason for this non-linearity is that at $+4$ °C and above, the PICO melt model produces basal shelf melt rates sufficient to melt through the ice shelf entirely along some parts of the grounding line, leading those regions of the ice shelf to become disconnected. In the $+4$ °C scenario this only occurs in parts of the western Ronne Ice Shelf, while the $+6$ °C scenario sees the most extensive disappearance of ice near the grounding line. In addition to opening a much thicker calving front, this also causes PICO to redraw the ocean overturning boxes to span whatever floating ice still exists connected to the grounding line. While 6 °C of immediate ocean warming at depth is an unrealistic scenario by known climate change mechanisms barring some catastrophic event (Little and Urban, 2016), this
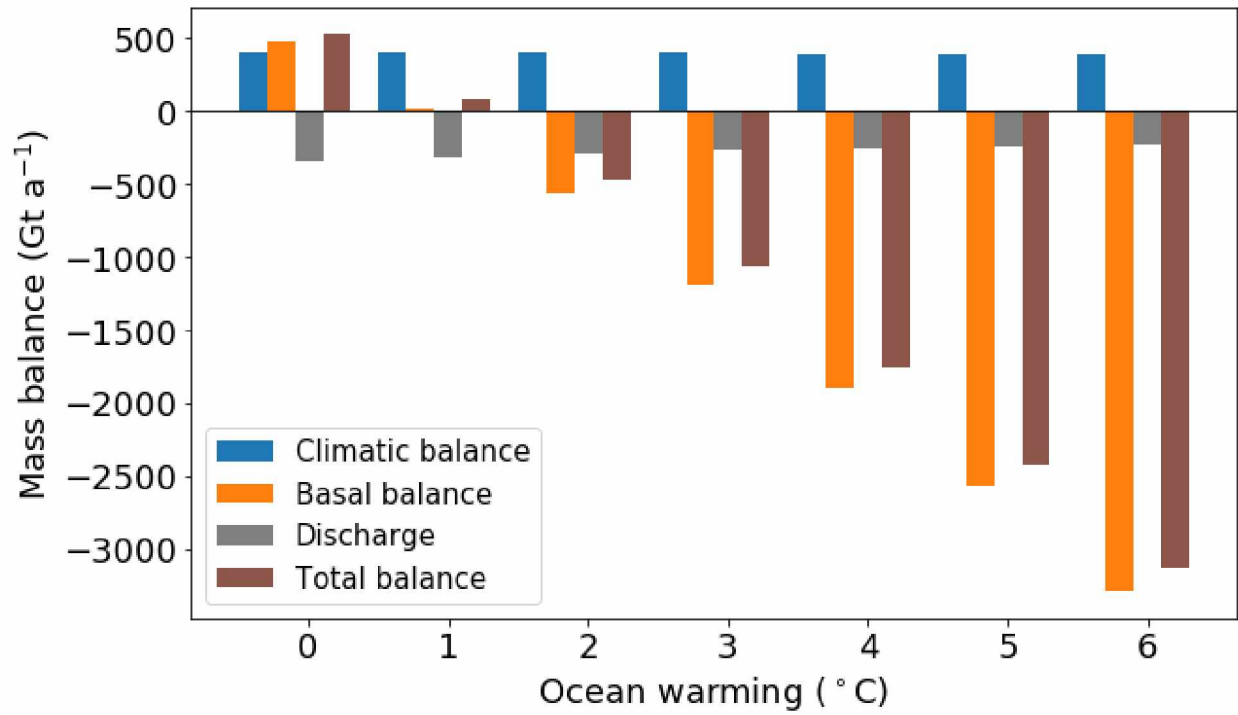
Figure 4.9: Magnitude of mass balance terms at 10 years into the simulation for each scenario. The median value from each ensemble is shown. Basal balance refers to the mass flux across the basal boundary of both grounded and floating ice. Discharge refers to the ice passing beyond the imposed maximum ice shelf extent, set here to present day ice shelf geometry.
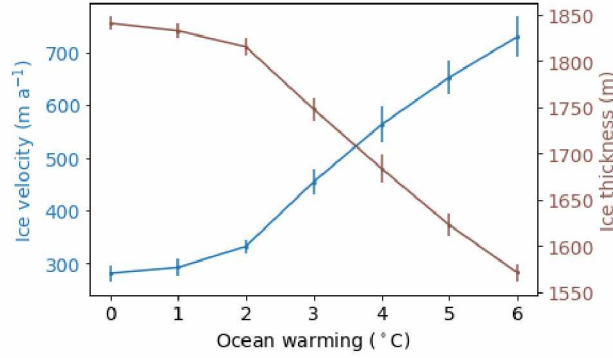
Figure 4.10: Ice surface velocity and thickness at one point on the Foundation Ice stream, approximately 90 km upstream of the initial grounding line. The exact position of this point is shown as an orange triangle in Figure 4.3. One standard deviation is shown for each ocean warming scenario. This point does not become ungrounded in any scenario.

scenario highlights the potential changes the Filchner-Ronne region would undergo in such a scenario, or at a future time, and these scenarios also show the importance of the Filchner-Ronne Ice Shelf in abutting the flow of grounded ice, as highlighted by grounding line fluxes in Figure 4.8.

Our results demonstrate that increased melting results in significantly increased velocities, potentially far from the locations where the ice has thinned or disappeared. Figure 4.10 shows velocities at one point on the Foundation Ice Stream. In the 4 °C scenario the distance between this location and the regions where the ice shelf which disappeared entirely was 670 km, although there was thinning near the grounding line much closer. While this point on the Foundation Ice Stream saw ice acceleration and thinning, it remains grounded in all of the ocean temperatures scenarios. The velocity increased with increased ocean temperature, and that rate became higher after +2 °C. At +2 °C warming the ice also began thinning more rapidly (Figure 4.10). The +2 °C inflection point is the same ocean temperature where the system changed from gaining mass by 2100 to losing mass (Figure 4.7).

With temperature increases also came accelerated grounding line retreat. The areas which changed to either grounded or ungrounded ice by 2100 are shown in Figure 4.11 and demonstrate significant retreat in the warmer scenarios and little retreat in the +0°C and +1 °C ocean warming scenario. In the +0°C scenario, freeze-on at the front of the Ronne

100

Ice Shelf results in a new pinning point forming as ice becomes grounded on an ice rise in the bed topography at the front. At +2 °C the grounding areas retreat by over 39000 km^2, increasing to 120000 km^2 at +6 °C.

The +2°C ocean temperature scenario marks the point where the retreat begins to surpass advance. During this scenario the ice sheet experiences mass gain over the first half of the time span (Figure 4.6). While this temperature scenario has a mean melt rate of 5.1 m a^{-1} at the grounding line, as measured by the mean across the innermost PICO box, the front of the ice shelf has freeze-on rates of approximately 1 m a^{-1}. The mass change of the region only turns negative in the later half of the time span, and because it is not due to the surface mass balance forcing (which is constant), then it is a product of dynamical effects of the increased grounding line thinning and retreat.

Throughout these tests the ocean salinity was held constant. The PICO parameterization of subshelf melt is built on the three-equation model from Holland and Jenkins (1999), which uses salinity for the turbulent mixing of low salinity meltwater and the higher salinity subshelf water. To test the impact of our salinity assumption, we created PICO melt fields for the +2°C and +6°C ocean temperature scenarios with basin salinity values varying from from 33.0 to 35.0 psu. In the 2°C scenario, the mean melt at the grounding line increased by 0.29 m a^{-1} psu^{-1} (5.8% of the mean melt rate), and in the 6°C scenario melt increased by 0.61 m a^{-1} psu^{-1} (2.9% of the mean melt rate).

4.5   Conclusions

The results of this study show the ice loss potential of the Filchner-Ronne region of Antarctica for scenarios of increasing ocean temperatures. Warming of just 2°C could result in a change of 660±660 Gt of ice above flotation (contributing -2.0±2.0 mm to sea level) by 2100. The 6°C warming scenario provides a situation in which the Filchner-Ronne ice shelf rapidly collapses this century due to highly increased basal melt. In that scenario ice decreased by 28370±1590 Gt, with an overall contribution of 85.3±4.8 mm to sea level.
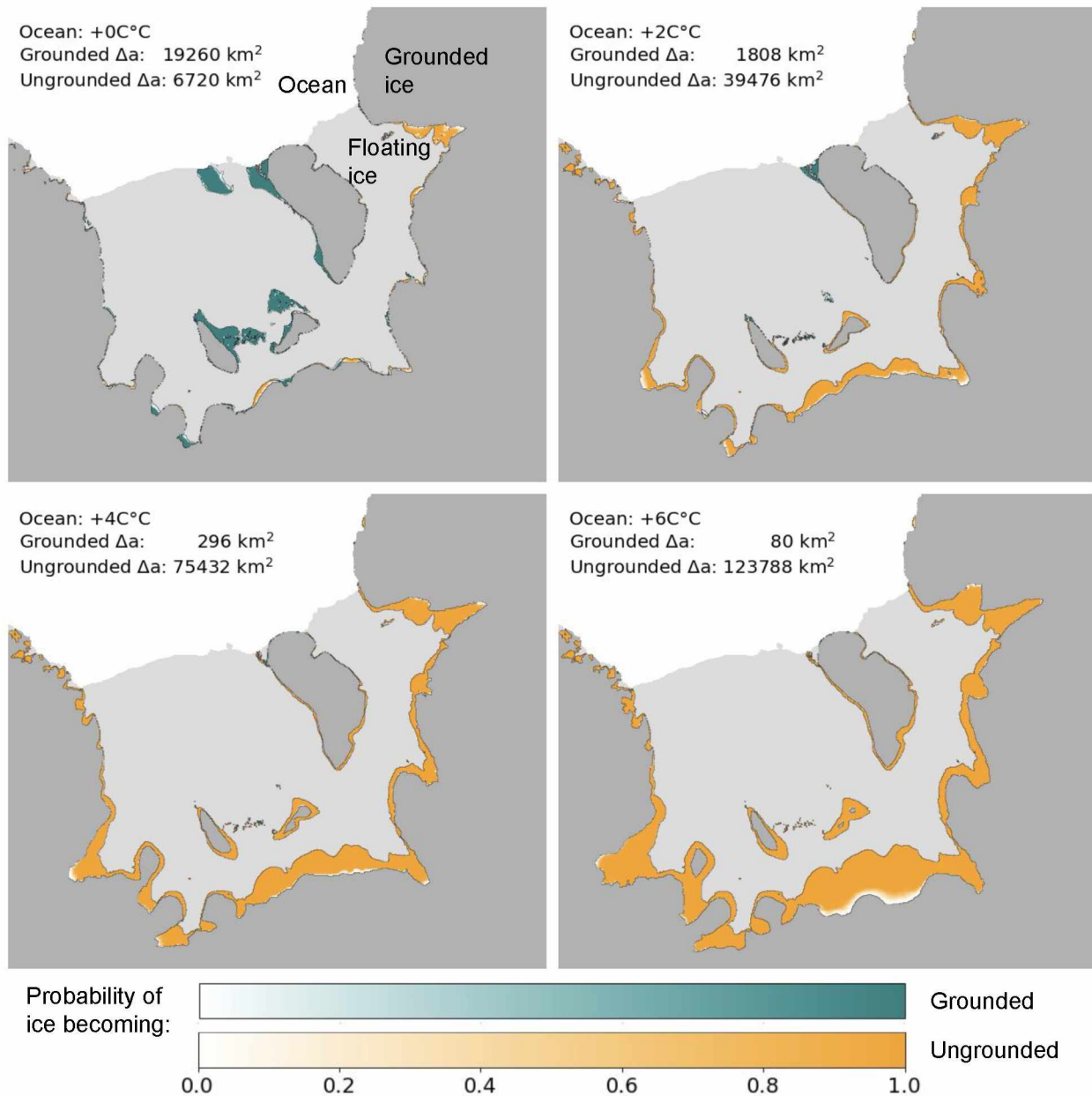
Figure 4.11: Areas that become grounded or ungrounded by 2100 relative to 2015. Each map shows probability across all ensemble members for that scenario. The grey shaded areas show the initial spatial distribution of grounded and floating ice in the model. Areas (Δa) becoming grounded or ungrounded are given for each scenario

Mass fluxes across the grounding line similarly grow increasingly negative, from –270±9 Gt a^{-1} in the no warming scenario up to –1174±64 Gt a^{-1} in the 6°C scenario at year 2100. Correspondingly, grounding lines retreat further with progressively more aggressive climate scenarios, resulting in a decrease in area of grounded ice up to 123000 km^2.

This work demonstrates the use of a surrogate model analysis with observed ice velocities to provide parameter sets of ice sheet model ensembles. In the 300 model calibration runs, the initial grounding line flux at year 2015 had a standard deviation of 118 Gt a^{-1} (with an overall mean of -316 Gt a^{-1}). However, the +0 °C ocean temperature scenario, which had the same atmosphere and ocean forcing as the calibration setup, the standard deviation in grounding line flux at year 2015 was just 9.1 Gt a^{-1}. The ensemble of calibration runs drew their parameter values from uniform distributions, and despite that there was minimal tuning of the parameter space for the calibration runs, the Markov Chain Monte Carlo sampling with a surrogate model was able to greatly reduce uncertainty and ignore unrealistic parameter values for the ensemble model runs used to project the future of the ice sheet in this region. This approach of surrogate model analysis (Brinkerhoff et al., 2020) with observation data shows promise for decreasing the uncertainty in projections of future ice evolution and sea level rise.

4.6   References

Albrecht, T., R. Winkelmann, and A. Levermann (2020), Glacial-cycle simulations of the antarctic ice sheet with the parallel ice sheet model (pism)–part 2: Parameter ensemble analysis, *The Cryosphere, 14*(2), 633–656.

Aschwanden, A., E. Bueler, C. Khroulev, and H. Blatter (2012), An enthalpy formulation for glaciers and ice sheets, *Journal of Glaciology, 58*(209), 441–457.

Aschwanden, A., M. A. Fahnestock, M. Truffer, D. J. Brinkerhoff, R. Hock, C. Khroulev, R. Mottram, and S. A. Khan (2019), Contribution of the greenland ice sheet to sea level over the next millennium, *Science advances*, *5*(6), eaav9396.

Barthel, A., C. Agosta, C. M. Little, T. Hattermann, N. C. Jourdain, H. Goelzer, S. Nowicki, H. Seroussi, F. Straneo, and T. J. Bracegirdle (2020), Cmip5 model selection for ismip6 ice sheet model forcing: Greenland and antarctica, *The Cryosphere*, *14*(3), 855–879.

Brinkerhoff, D., A. Aschwanden, and M. Fahnestock (2021), Constraining subglacial processes from surface velocity observations using surrogate-based bayesian inference, *Journal of Glaciology*, *67*(263), 385–403.

Bueler, E., and J. Brown (2009), Shallow shelf approximation as a "sliding law" in a thermomechanically coupled ice sheet model, *Journal of Geophysical Research: Earth Surface*, *114*(F3).

Danabasoglu, G., J.-F. Lamarque, J. Bacmeister, D. Bailey, A. DuVivier, J. Edwards, L. Emmons, J. Fasullo, R. Garcia, A. Gettelman, et al. (2020), The community earth system model version 2 (cesm2), *Journal of Advances in Modeling Earth Systems*, *12*(2).

Dupont, T., and R. Alley (2005), Assessment of the importance of ice-shelf buttressing to ice-sheet flow, *Geophysical Research Letters*, *32*(4).

Fretwell, P., H. D. Pritchard, D. G. Vaughan, J. L. Bamber, N. E. Barrand, R. Bell, C. Bianchi, R. Bingham, D. D. Blankenship, G. Casassa, et al. (2013), Bedmap2: improved ice bed, surface and thickness datasets for antarctica, *The Cryosphere*, *7*(1), 375–393.

Gardner, A. S., M. Fahnestock, and T. A. Scambos (2019), Its_live regional glacier and ice sheet surface velocities, *Data archived at National Snow and Ice Data Center*.

Golledge, N. R., E. D. Keller, N. Gomez, K. A. Naughten, J. Bernales, L. D. Trusel, and T. L. Edwards (2019), Global environmental consequences of twenty-first-century ice-sheet melt, *Nature*, *566*(7742), 65–72.

Groh, A., and M. Horwath (2021), Antarctic ice mass change products from grace/grace-fo using tailored sensitivity kernels, *Remote Sensing*, *13*(9), 1736.

Habermann, M., M. Truffer, and D. Maxwell (2013), Changing basal conditions during the speed-up of jakobshavn isbræ, greenland, *The Cryosphere*, *7*(6), 1679–1692.

Haran, T., J. Bohlander, T. Scambos, T. Painter, and M. Fahnestock (2014, updated 2019), Modis mosaic of antarctica 2008-2009 (moa2009) image map, version 1, nSIDC: National Snow and Ice Data Center Distributed Active Archive Center, Version 1 South 19H and 37V. Doi: https://doi.org/10.7265/N5KP8037. Last accessed: 2020-2-7.

Hattermann, T., K. W. Nicholls, H. H. Hellmer, P. E. Davis, M. A. Janout, S. Østerhus, E. Schlosser, G. Rohardt, and T. Kanzow (2021), Observed interannual changes beneath filchner-ronne ice shelf linked to large-scale atmospheric circulation, *Nature communications*, *12*(1), 1–11.

Hazel, J. E., and A. L. Stewart (2020), Bistability of the filchner-ronne ice shelf cavity circulation and basal melt, *Journal of Geophysical Research: Oceans*, *125*(4), e2019JC015,848.

Hellmer, H. H., F. Kauker, R. Timmermann, J. Determann, and J. Rae (2012), Twenty-first-century warming of a large antarctic ice-shelf cavity by a redirected coastal current, *Nature*, *485*(7397), 225–228.

Hill, E. A., S. H. Rosier, G. H. Gudmundsson, and M. Collins (2021), Quantifying the potential future contribution to global mean sea level from the filchner-ronne basin, antarctica, *The Cryosphere Discussions*, pp. 1–43.

Holland, D. M., and A. Jenkins (1999), Modeling thermodynamic ice–ocean interactions at the base of an ice shelf, *Journal of Physical Oceanography*, *29*(8), 1787–1800.

Jakobs, C. L., C. H. Reijmer, C. P. Smeets, L. D. Trusel, W. J. Van De Berg, M. R. Van Den Broeke, and J. M. Van Wessem (2020), A benchmark dataset of in situ antarctic surface melt rates and energy balance, *Journal of Glaciology*, *66*(256), 291–302.

Little, C. M., and N. M. Urban (2016), Cmip5 temperature biases and 21st century warming around the antarctic coast, *Annals of Glaciology*, *57*(73), 69–78.

Martin, M., R. Winkelmann, M. Haseloff, T. Albrecht, E. Bueler, C. Khroulev, and A. Levermann (2011), The potsdam parallel ice sheet model (pism-pik)–part 2: dynamic equilibrium simulation of the antarctic ice sheet, *The Cryosphere*, *5*(3), 727–740.

Morlighem, M., E. Rignot, T. Binder, D. Blankenship, R. Drews, G. Eagles, O. Eisen, F. Ferraccioli, R. Forsberg, P. Fretwell, et al. (2020), Deep glacial troughs and stabilizing ridges unveiled beneath the margins of the antarctic ice sheet, *Nature Geoscience*, *13*(2), 132–137.

Naughten, K. A., J. De Rydt, S. H. Rosier, A. Jenkins, P. R. Holland, and J. K. Ridley (2021), Two-timescale response of a large antarctic ice shelf to climate change, *Nature communications*, *12*(1), 1–10.

Nicholls, K. W., and S. Østerhus (2004), Interannual variability and ventilation timescales in the ocean cavity beneath filchner-ronne ice shelf, antarctica, *Journal of Geophysical Research: Oceans*, *109*(C4).

Reese, R., T. Albrecht, M. Mengel, X. Asay-Davis, and R. Winkelmann (2018), Antarctic sub-shelf melt rates via pico, *The Cryosphere*, *12*(6), 1969–1985.

Schmidtko, S., K. J. Heywood, A. F. Thompson, and S. Aoki (2014), Multidecadal warming of antarctic waters, *Science*, *346*(6214), 1227–1231.

Seroussi, H., S. Nowicki, E. Simon, A. Abe-Ouchi, T. Albrecht, J. Brondex, S. Cornford, C. Dumas, F. Gillet-Chaulet, H. Goelzer, et al. (2019), initmip-antarctica: an ice sheet model initialization experiment of ismip6, *The Cryosphere*, *13*(5), 1441–1471.

Seroussi, H., S. Nowicki, A. J. Payne, H. Goelzer, W. H. Lipscomb, A. Abe-Ouchi, C. Agosta, T. Albrecht, X. Asay-Davis, A. Barthel, et al. (2020), Ismip6 antarctica: a multi-model ensemble of the antarctic ice sheet evolution over the 21st century, *The Cryosphere*, *14*(9), 3033–3070.

Sidorenko, D., T. Rackow, T. Jung, T. Semmler, D. Barbi, S. Danilov, K. Dethloff, W. Dorn, K. Fieg, H. F. Gößling, et al. (2015), Towards multi-resolution global climate modeling with echam6–fesom. part i: model formulation and mean climate, *Climate Dynamics*, *44*(3-4), 757–780.

Sun, S., F. Pattyn, E. G. Simon, T. Albrecht, S. Cornford, R. Calov, C. Dumas, F. Gillet-Chaulet, H. Goelzer, N. R. Golledge, et al. (2020), Antarctic ice sheet response to sudden and sustained ice-shelf collapse (abumip), *Journal of Glaciology*, *66*(260), 891–904.

Timmermann, R., and S. Goeller (2017), Response to filchner–ronne ice shelf cavity warming in a coupled ocean–ice sheet model–part 1: The ocean perspective, *Ocean Science*, *13*(5), 765–776.

Trusel, L. D., K. E. Frey, S. B. Das, K. B. Karnauskas, P. K. Munneke, E. Van Meijgaard, and M. R. Van Den Broeke (2015), Divergent trajectories of antarctic surface melt under two twenty-first-century climate scenarios, *Nat. Geosci.*, *8*(12), 927–932.

Van Wessem, J. M., W. J. Van De Berg, B. P. Noël, E. Van Meijgaard, C. Amory, G. Birnbaum, C. L. Jakobs, K. Krüger, J. Lenaerts, S. Lhermitte, et al. (2018), Modelling the climate and surface mass balance of polar ice sheets using racmo2–part 2: Antarctica (1979–2016), *The Cryosphere*, *12*(4), 1479–1498.

Weertman, J. (1974), Stability of the junction of an ice sheet and an ice shelf, *Journal of Glaciology, 13*(67), 3–11.

Winkelmann, R., M. A. Martin, M. Haseloff, T. Albrecht, E. Bueler, C. Khroulev, and A. Levermann (2011), The potsdam parallel ice sheet model (pism-pik)–part 1: Model description, *The Cryosphere, 5*(3), 715–726.

Zwally, H. J., M. B. Giovinetto, M. A. Beckley, and J. L. Saba (2012), Antarctic and greenland drainage systems, gsfc cryospheric sciences laboratory.

Zwally, H. J., J. W. Robbins, S. B. Luthcke, B. D. Loomis, and F. Rémy (2021), Mass balance of the antarctic ice sheet 1992–2016: reconciling results from grace gravimetry with icesat, ers1/2 and envisat altimetry, *Journal of Glaciology, 67*(263), 533–559.

5 Conclusion

Chapter 2 showed an evaluation of passive microwave melt detection methods using time series of Sentinel 1 SAR observations. This work has demonstrated that melt was spatially uniform on ice shelves for the coarse 25 km passive microwave pixels. The SAR results showed that on ice shelves 98.9% of the melt determinations within individual 25 km pixels agreed with each another. Off the ice shelves however this agreement was much lower at 93%, and in those regions when more than 50% of SAR observations for a passive pixel showed melt, then the overall agreement within that pixel dropped to 73%. Topographic features especially caused heterogeneity in spatial distribution of melt, and in regions like the Antarctic Peninsula, there is often high topographic variability adjacent to ice shelves. The comparison to passive microwave results showed that the SAR melt results agreed with the passive microwave melt results up to 95.0% of the time, and 89.2% of the time during November through March. The results of this chapter showed that the Winter+30K melt threshold method overcounted melt while the Cross Polarization Gradient Ratio method had the highest correlation but greatly underestimated melt. The statistical method based on KMeans clustering and the method based on finding 3 standard deviation above winter had good accuracy and correlation. Of these, the KMeans method had the highest informedness, implying that it was the least biased to overcounting or undercounting melt. For these reasons, the KMeans method is the best method suggested for melt detection on Antarctic ice shelves. If false negatives and undercounting melt are not a concern in a melt detection study, then the Cross Polarization Gradient Ratio method would be recommended. Conversely, if the false positive rate or overcounting of melt are of no concern, then the Winter+30K method would be superior.

Chapter 2 demonstrated the use of Sentinel-1 SAR images as a tool to produce time series measurements of the Antarctic Peninsula with near-daily frequency. This application demonstrates a conceptualization of SAR as a platform for producing a dense time series,

109

and is enabled by modern tools for processing big data sets such as Google Earth Engine. Other studies have begun using Sentinel-1 to detect melt with Google Earth Engine (e.g. Snapir et al., 2019 and Liang et al., 2021). However, SAR-based melt detection likely still has room to grow in terms of improving the melt detection methodology as well developing new melt detection data products. One particular issue with using Sentinel-1 SAR data in Google Earth Engine is the variability of backscatter between images with different viewing geometries of the same target. This variability between viewing geometry prevented the possibility of melt detection from many of the SAR images in Chapter 2 because individual viewing geometries could only be used if they imaged the firn surface during the winter preceding melt. Platforms such as the Hybrid Pluggable Processing Pipeline (HyP3) at the Alaska Satellite Facility can provide SAR time series built on a different method of radiometric terrain correction which might alleviate part of this issue. With the amount near-daily frequency of SAR images, and especially if the issue of variability between viewing geometries can be resolved, then it could be possible to not just identify melt in single Sentinel-1 SAR images, but also quantify the number of annual melt days for the entire Antarctic periphery using Sentinel-1 SAR. A dense SAR time series might even open the possibility for quantifying total melt, not just melt days, following the same melting decibel-day approach developed in Trusel et al. (2012) for use with scatterometer observations.

The results of Chapter 3 demonstrate the spatial and temporal patterns of melt days on ice shelves across Antarctica. Melt days are the highest on Antarctic Peninsula Ice Shelves as well as on the West and Shackleton Ice Shelves, and lowest on the Ross and Ronne-Filchner. There are few linear trends in the number of annual melt days on ice shelves. The modes of variability of annual melt days for ice shelf pixels are dominated by two modes of variability, those with high melt on the Antarctic Peninsula and Bellingshausen Sea Sector of West Antarctica, and those with high melt in Dronning Maud Land. These modes broadly align with melt in spatial patterns of melt in years in which some ice shelves have abnormally high melt. Furthermore, the mode of variability dominated by melt in Dronning Maud Land

110

also shares resemblance to locations which have the strongest negative correlation to October through January SAM values, suggesting the importance of SAM in the variability of climate on many Antarctic ice shelves.

In Chapter 3, changes in the backscatter of dry firn after melt were shown to be potentially indicative of changes in firn grain size and ice lens frequency on firn surfaces which traditionally have low melt. Chapter 3 has suggested the value of looking at the history of brightness temperatures before and after melt seasons as a way to better understand the evolution of these surfaces, and help to identify when melt events occurred, or identify the year which produced a particular ice lens. Chapter 3 did not create a complete catalogue of all ice shelf surface changes and there is variability in the seasonal brightness temperature change time series which did not appear to be driven by notable identifiable melt events. However, a more exhaustive study of that topic alone, likely if paired with more regional climate model histories of annual surface melt as well as weather station observations, has the possibility to produce a full and useful dataset of abnormal passive microwave-identified firn densification events.

In addition, as noted in Chapter 3, the decrease in backscatter is the result of changes in the microwave-band scattering of the surface, and so radar measurements should also be impacted, both with increased volume scattering due to larger grains, and scattering off the ice lenses, which have a rough upper surface and are punctuated by perpendicular flow fingers in the snowpack making ideal double bounce reflectors. Chapter 3 demonstrated that this inferred increased backscatter has likely already affected radar altimitry measurements on the Ross Ice Shelf, but this phenomena has not been comprehensively studied in radar or SAR yet to determine if it has a useful application to quantifying the aftermath of abnormally high melt events in Antarctica.

Chapter 4 demonstrated the impacts of increased ocean potential temperature at depth in front of the Filchner Ronne Ice Shelf. An ensemble of runs were conducted for each scenario and run from 2015–2100. With 2°C of ocean warming, the ice shelf mass changed

111

by $+660\pm660$ (contributing 2.0 ± 2.0 mm to sea level), and the annual grounding line flux increased from 241 ± 6 Gt a^{-1} at the start to 420 ± 12 Gt a^{-1} by the end of the period. At 4°C of warming, a few small regions of the ice shelf collapse entirely and the grounding line ice flux reaches 645 ± 24 Gt a^{-1}, while the region lost 10290 ± 960 Gt of ice mass above flotation (31.0 ± 2.9 mm sea level rise). The 6°C scenario saw the disappearance of much of the ice shelf at the grounding line. While this scenario is well outside the range of climate projections for the 21st century (Little and Urban, 2016), this scenario can roughly approximate what it would take for the ice shelf to collapse entirely this century, and the scenario results in a grounding line flux of 117 ± 74 Gt a^{-1}, with an ice mass loss of 28370 ± 1590 Gt, equating to 85.3 ± 4.8 mm of sea level rise. This study has found that between ocean potential temperature increases of 0°C to 4°C, sea level rise by year 2100 increases by 14 mm °C^{-1}. The scenario with zero ocean warming saw a mass increase of 8020 ± 560 Gt above flotation. PICO prescribed additional freeze-on at the front of the ice shelf which resulting in ice at the front of the Ronne Ice Shelf becoming grounded on a new pinning point. These results highlight the wide range of impacts this region can have on sea levels due to ocean forcing.

5.1 References

Liang, D., H. Guo, L. Zhang, Y. Cheng, Q. Zhu, and X. Liu (2021), Time-series snowmelt detection over the antarctic using sentinel-1 sar images on google earth engine, *Remote Sensing of Environment*, *256*, 112,318.

Little, C. M., and N. M. Urban (2016), Cmip5 temperature biases and 21st century warming around the antarctic coast, *Annals of Glaciology*, *57*(73), 69–78.

Snapir, B., A. Momblanch, S. Jain, T. W. Waine, and I. P. Holman (2019), A method for monthly mapping of wet and dry snow using sentinel-1 and modis: Application to a himalayan river basin, *International Journal of Applied Earth Observation and Geoinformation*, *74*, 222–230.

Trusel, L., K. E. Frey, and S. B. Das (2012), Antarctic surface melting dynamics: Enhanced perspectives from radar scatterometer data, *Journal of Geophysical Research: Earth Surface, 117*(F2).